Production and Stark deceleration of lithium hydride molecules

Sean Kaoru Tokunaga

Thesis submitted in partial fulfilment of the requirements for the degree of
Doctor of Philosophy of the University of London and the Diploma of Membership
of
Imperial College.

Imperial College London

University of London

March 2009

Abstract

Production and Stark deceleration of lithium hydride molecules

Sean Kaoru Tokunaga

This thesis describes the first production of cold, slow-moving ^{7}LiH molecules. A fast-moving pulse of cold molecules is produced by laser ablation of Li into a supersonically expanding carrier gas containing H_2. This pulse travels at either 600m/s or 420m/s, depending on the carrier gas used. Translational, vibrational and rotational temperatures are found to be 0.9±0.1K, 5.9±0.5K and 468±17K respectively, with 90% of the molecules in the ground state. Molecules are detected through laser-induced fluorescence using a frequency doubled Ti:Sapphire laser tuned to the $A^1\Sigma^+$-$X^1\Sigma^+$ transitions at around 375nm. The number of ground state molecules is found to be $4.5 \pm 1.8 \times 10^7$ molecules per steradian per shot.

Ground state molecules are transferred to the first rotationally excited state using narrowband radiation at 444GHz. The radiation is produced by quintupling the 88.8GHz output of a Gunn oscillator, resulting in 60μW of power and a 15kHz linewidth. At full power, a driving efficiency of 68% is measured. At lower power, some of the hyperfine structure of the rotationally excited state is resolved. The measured rotational transition is 443952.91±0.09MHz, in agreement with two other measurements of similar precision.

Molecules in the rotationally excited state are decelerated using a Stark decelerator. Here, the force experienced by a polar molecule in an electric field gradient is used to focus and decelerate the molecules. Starting from 420m/s, the molecules are decelerated to 53m/s, corresponding to a 98.5% reduction in kinetic energy. The temperature of the decelerated bunch is approximately 15mK. Experimental data is compared to numerical simulations, and good agreement is obtained. In an attempt to increase the flux, an alternative mode of deceleration is demonstrated. Although the final speed of the decelerated molecules is higher for a given voltage, the number of decelerated molecules increases by an order of magnitude when this alternative mode is applied.

Acknowledgements

I would like to thank my supervisors Mike Tarbutt and Ed Hinds. Thank you both for your support, guidance and boundless patience. And most of all, thank you for this opportunity to work with you. Mike, thanks also for doubling up as my post-doc. I wouldn't have got anything done without your continuous presence in the lab. Ed, thank you for your insights, questions and encouragement. I'm proud to have studied under the two of you.

To Ben and Jony, thank you for your advice both in and out of the lab, as well as your friendship. Your sense of humour always makes you good company. I'd also like to thank all the students in the fridge (B114). In particular, I want to thank Dan and Dhiren for the fascinating (although sometimes circular) discussions, as well as Thom for putting up with me both in the office and in the flat. Thanks also to my lab-mates, Jake and Ianjit, for their hard work. Michael, Thenasis and Benoit, thanks for the enjoyable (and often instructive) morning coffee breaks. Finally, thanks to everyone else in CCM (and ex-CCMers), including Henry, Isabel, Jonathan and Richard. Thank you all for a fascinating and delightful few years.

I would also like to thank Jon and Dave from the workshop. Thank you for building the decelerator, and indeed most of the other components in the experiment. Thank you also for your careful instruction on how to operate some of the machines. I want to thank Tim Steimle for his help and suggestions on how to improve the molecular beam source.

I also gratefully acknowledge EPSRC and EuroQUAM for financial support.

I'd also like to thank Nora and the people at Clayponds for their support and encouragement. I'd like to thank my parents for years of financial support and for your confidence in my decisions. Thanks also to John and Kostya from BPIS, as well as my friends here and back home, including Roy, Patrice, Alexis, Celine, Hansa, Keith, Bri, Olly and Olinka. Your enthusiasm for what I do is a great motivation.

To my mother, father, Chris and Pat.

Contents

List of Figures

List of Tables

Chapter 1

Introduction

Cold molecules are desirable for a diverse range of applications in physics and chemistry [1]. Polar molecules are of particular interest, their interaction with electric fields being typically several orders of magnitude larger than that of atoms. This interaction is the basis for Stark deceleration, a technique for producing samples of slow, cold molecules [2]. So far applied to just a few molecular species, the technique involves using inhomogeneous time-varying electric fields to reduce the velocity of molecules in a pulsed beam.

Lithium hydride is a good candidate for many cold-molecule experiments. It offers a favourable electric dipole moment to mass ratio and a very-well characterized structure, simple enough to make calculations of collision cross-sections seem feasible. Because it has a large rotational constant and no lambda-doubling, it is possible to produce a beam where most of the molecules are in a single quantum state. Furthermore, both bosonic and fermionic species are available. Despite these advantages, cold samples of LiH had never been produced, through Stark deceleration or otherwise. This thesis reports the first production of a cold beam of LiH molecules and its deceleration to low speeds.

This chapter begins by motivating the production of ultra-cold molecules. This is followed by a review of the techniques for producing cold molecules developed to date. I will then conclude with an overview of the experiment covered in this thesis.

Chapter 2 covers the production and detection of a supersonic beam of LiH. Chapter 3 describes the population transfer to a rotationally excited state. This allows the beam to be decelerated to rest using a Stark decelerator, as will be demonstrated in chapter 4. Chapter 5 contains a summary of the work and a future outlook.

The work presented in this thesis has led to the following publications [3, 4].

1.1 Motivation

In this section, I outline some of the many motivations for producing samples of ultra-cold molecules.

1.1.1 High-resolution spectroscopy

High resolution spectroscopy of atoms, ions and molecules has, for many decades, made an enormously valuable contribution to metrology, measurements of fundamental constants and precision tests of fundamental physical theories. In the case of ions, where their overall charge facilitates their manipulation, experiments have reached an unparalleled level of control. Single ions can be trapped almost indefinitely, allowing extremely long measurement times. The latest triumph in single-ion precision measurement experiments is a measurement of the electron magnetic moment [5] and of the fine structure constant α to 0.7 parts per billion [6].

As for their neutral counterparts, the development of atomic beams has led to innumerable successful measurements. Laser spectroscopy along with electric and magnetic resonance techniques applied to atomic and molecular beams constitute the bulk of precision measurements to date. These collimated jets travelling at several hundreds to thousands of m/s has allowed, amongst many others, values for the Rydberg constant [7], Lamb shifts in hydrogen [8], parity violations [9] and electric dipole moments of fundamental particles (e.g. [10]) to be determined to unprecedented levels of accuracy, most of which have yet to be superseded.

One limitation in these experiments is often their interaction time due to the high velocity of the atoms or molecules in the beam. In the special case of atoms with a simple energy-level structure, the introduction of laser cooling overcame this difficulty by cooling and slowing the atoms down. Atomic fountains for instance, which effectively create a 'very slow beam' by launching laser cooled atoms upward, increased the interaction time by many orders of magnitude. In fact, these fountains proved to be so successful that they now provide the world's standard for time [11]. The most recent years have seen the demonstration of optical lattices which trap single atoms at each lattice site. Replacing the traditional beam experiments with lattices is an ongoing topic of research [12].

Nonetheless, experiments involving other atoms or all molecules (where laser cooling is not easily applicable) still predominantly involve beams. Stark deceleration offers an exciting possibility of increasing the interaction time without the need for laser cooling, an appealing prospect for high resolution spectroscopy of molecules.

Time reversal symmetry violation

The electric dipole moment of elementary particles vanishes unless parity (P) and time reversal (T) symmetries are violated [13]. Measuring a non-zero electric dipole moment in a fundamental particle implies T-violation which through the CPT theorem also implies CP-violation. Such a measurement would be complementary to the experiments on K and B particles where the observed CP-violation confirms the standard model CKM mechanism [14, 15]. In the standard model, the upper limit on a dipole moment for an electron d_e is around 10^{-38}e cm. However, several other theories which go beyond the standard model predict d_e to be around $10^{-26} - 10^{-28}$e cm. Measuring d_e can therefore also provide a direct test for physics beyond the standard model.

The most accurate measurement of d_e to date is the one by Regan *et al.* who measured a value of $d_e = (7 \pm 8) \times 10^{-28}$e cm by searching for a differential Stark shift between two hyperfine levels $F = 1$ $m_f = \pm 1$ in ground state atomic thallium [10]. Thallium was chosen because of its mass. Because this differential energy shift is relativistic in origin, heavier atoms offer the greatest sensitivity. A large external field E_{ext} is applied on the atoms, which polarizes them yielding an energy of the form $-\eta d_e \cdot E_{ext}$ where η is an 'enhancement factor' that depends on the structure of the atom.

It has since been shown that an improved measurement can be made in a beam of heavy polar molecules, e.g. YbF [16]. The main advantage of using dipolar molecules is that the orbital wavefunctions are already strongly polarized along the internuclear axis. An external field is then only required for aligning the internuclear axis with a lab-fixed frame, which can be achieved at moderate electric fields. For this reason, the enhancement factor η can be very much larger for molecules than for atoms. This experiment is currently under way in our laboratory. Better control over such beams, offered by methods such as Stark deceleration could constrain the value of d_e even further.

Parity violation in chiral and diatomic molecules

A chiral molecule is one whose mirror image is different from itself. Given their resemblance, the physical properties of the left and right-handed 'enantiomers', such as their density, boiling and melting points are unsurprisingly the same to within experimental accuracy. However, their biochemical properties seem to indicate some differences between the two strains. For instance, all living organisms exclusively contain left-handed amino acids. In physics, the weak interaction is the only interaction known to violate parity (P), the symmetry which would need to be broken to allow such observed differences. Measuring an energy level difference between left and right handed chiral molecules would not only be the signature for P-violation via the weak interaction [17, 18], but could shed light on the mechanisms behind the differences in their biochemical properties.

The most sensitive measurement to date was carried out on the CHFClBr molecule, where saturation spectroscopy was performed on the two enantiomers [19]. The resonance frequencies of hyperfine components of ro-vibrational transitions at around 9μm were compared. Although no parity violation was observed at the 2.5×10^{-13} level, the next generation of the experiment is currently under way and is expected to take the form of a molecular beam. Further control on the molecular velocity could also enhance this measurement.

There is also an experiment under way to measure parity violation associated with nuclear spin [20]. Such violations would give rise to anapole moments within diatomic molecules. This measurement is expected to be sensitive to new physics including quark substructures.

The time dependence of fundamental constants

Most modern physical theories assume the fundamental constants, such as α, do not change in time. Nonetheless, mechanisms have been proposed whereby the constants could vary over time due to processes like the expansion of the universe [21]. One method for verifying this assumption would be to compare two transitions which depend differently on α. Alternatively, it has been reported that the sensitivity to the time variation of the fundamental constants is enhanced when probing transitions between two narrow and close lying energy levels which, again, depend differently on

α [22].

One can also compare spectroscopic data obtained in the laboratory with astronomical data, thereby providing comparisons over longer time scales. Recently, laboratory measurements of the Lyman bands in H_2 were compared to spectral lines from quasars. The results suggest a change to the proton-electron mass ratio at $\Delta\mu/\mu = (2.4 \pm 0.6) \times 10^{-5}$ [23].

Very high precision measurements of the Λ-doublet microwave transitions in the ground state of the OH molecule have been made by probing a cold, slow sample produced by a Stark decelerator [24]. The use of a cold, slow beam improved the sensitivity over previous measurements by factors of 10 and 25 for the two transitions measured. Comparisons of the laboratory frequencies to those from OH megamasers in interstellar space are expected to give a sensitivity of 1 part per million for changes in the fine structure constant over a timespan of 10^{10} years.

Recently, there has also been a proposal to build a molecular fountain using Stark decelerated ammonia molecules [25], with the aim of performing another test for the time-variation of the proton-electron mass ratio.

Lifetime measurements of excited states

The ability to trap molecules using electric fields led to direct measurements of their upper state lifetimes. The Einstein A coefficients in the Meinel system of OH were measured directly by observing the loss rate in the trap [26]. A pulsed beam of vibrationally excited OH radicals was Stark decelerated and loaded into an electrostatic quadrupole trap. The radiative lifetime of the upper Lambda-doublet component of the $X^2\Pi_{3/2}$, $v = 1$, $J = 3/2$ level was determined as 59.0±2.0 ms. This measurement has important implications for infra-red absorption and emission spectroscopy, which is often used as a diagnostic in atmospheric and interstellar physics.

In a similar experiment, the lifetime of metastable CO molecules in the $a^3\Pi_1$ ($v = 0$, $J = 1$) state was measured to be 2.63±0.03ms. [27].

1.1.2 Quantum chemistry

The chemical properties of matter depend strongly on their temperature. Providing more control over the temperature brings new possibilities for collisional studies.

Collision cross-sections

Being able to control the velocity of molecules allows both elastic and inelastic collision cross-sections to be investigated. This is because the ability to tune the velocity provides control over the collisional energy. Recently, cross-sections for collisions between Stark decelerated OH molecules and Xe [28], He and D_2 [29] were measured for an energy range of several hundred cm^{-1}. In [28], the velocity tuned pulse of OH exiting the decelerator was scattered by a Xe beam travelling at a 90° angle. In [29], the OH molecules were first decelerated and loaded into a magnetic trap. A beam of He or D_2 was then made to travel through the trap. The velocity of this oncoming beam was tuned by changing the temperature of the valve.

An improved collision experiment is currently under way in Berlin. Two molecular beams are made to intersect perpendicularly in a standard cross-beam setup. The improvement in this experiment is that both beams exit from Stark decelerators, which will be used to tune the velocity of the two beams [30]. It is hoped that this experiment will mark the beginning of a new type of quantum chemistry where the reactions can be triggered on demand.

Controlling chemical reactions

Using external electric and magnetic fields to control chemical reactions has been an ongoing topic of research [31]. As the temperature of the gas is reduced, the collisional energy vanishes. This makes inelastic collision cross-sections extremely sensitive to intermolecular interaction potentials and relative energies of the initial and final states. Slight changes in molecular structure, induced for instance by external fields, could significantly change the outcome of an inelastic collision or chemical reaction. For instance, calculations predict the existence of bound states between pairs of diatomic molecules, but provided a DC electric field is present [32]. Not only would such control open new possibilities for selectively producing desired species, but would also be useful in testing reaction rate theories or finer details of molecular structure and interaction potentials. Such control may also allow studies of non-adiabatic and relativistic effects in chemical dynamics.

It has recently been shown that the H-abstraction channel between OH and H_2CO could be controlled by means of selectively populating some of the internal states or by applying an electric field [33]. This is not only an important reaction in the combustion of hydrocarbons, but is also the primary process for the removal of H_2CO (a pollutant) from the atmosphere. To this end, the group reports the successful Stark deceleration of H_2CO. They now plan to combine this experiment with their existing one for Stark decelerating OH [34].

1.1.3 Quantum degenerate gases with dipole-dipole interactions

After the first observation of a Bose-Einstein condensate of rubidium 87 atoms in 1995 [35], experimenters turned their attention to producing yet more novel phases of matter. In 2001, the first Fermi gas was produced in lithium [36]. In 2002, the first direct measurement of the phase transition from an incompressible superfluid to Mott insulator was observed [37]. Owing to their rich structure, molecules have been predicted to offer a large range of new, yet unobserved phases. In particular, the creation of an ultracold dipolar gas would allow the engineering of a rich variety of many body quantum phases, including supersolid, checkerboard and collapse phases in addition to the superfluid and Mott insulator phases already observed [38]. These new phases require the dipole-dipole interactions to dominate over the van der Waals interactions. The dimensionless quantity measuring the strength of the dipolar interactions relative to the s-wave scattering can be written as

$$\epsilon_{dd} = \frac{a_{dd}}{a_s} = \frac{1}{3}\frac{M}{m_e}\frac{a_0}{a_s}d^2, \tag{1.1}$$

where a_s and a_{dd} are the s-wave and effective dipole-dipole scattering lengths, M is the mass of the atom or molecule, m_e is the electron mass, a_0 is the Bohr radius and d is the value of the dipole moment in atomic units. For rubidium 87, ϵ_{dd} only approaches 1 in an applied electric field of 700kV/cm, an enormous field. On the other hand, taking M=50a.u., d=1Debye and a_s=100a_0 as typical values for a polarized molecule, ϵ_{dd} is around 47. The only fields required then would be to polarize the molecule, which is achievable at very moderate fields. This difference which spans across orders of magnitude is what makes dipolar molecules attractive candidates for investigating these quantum phase transitions.

Other potential novel effects include roton-maxon spectra in pancake-shaped dipolar condensates [39], BCS superfluidity in fermionic polar gases [40], fractional quantum-Hall states in rotating dipolar Fermi gases [41] and vortex lattices in rotating dipolar Bose gases [42].

There have also been proposals to use the dipole-dipole interaction of ultra-cold polar molecules for quantum information processing [43, 44, 45].

1.2 Cooling molecules

The lack of closed transitions make laser cooling difficult to apply to molecules, although there are nonetheless some proposals to do so [46]. Any manipulation or cooling of molecules must be achieved without laser cooling. Several schemes have been developed in the recent years.

1.2.1 Buffer gas

In this technique originally developed by Doyle, the atoms or molecules of interest are produced in a cryostat filled with He. The helium acts as a buffer gas, allowing the molecules to reach thermal equilibrium through collisions [47]. The atoms can be ablated off a solid target placed inside the cryostat, cooled, then trapped in an anti-Helmholz magnetic trap. Using this technique, 10^{12} Europium [48] and 10^{11} Chromium [49] atoms were trapped at temperatures between 0.3K to 1.4K. 10^8 CaH molecules were also successfully trapped with a temperature of 800mK [50]. More recently, NH was also trapped using the buffer gas method [51]. However, instead of ablating a target inside the cell, the molecules were first created in a beam, then injected into the buffer gas cell [52].

In order to obtain an isolated sample, the buffer gas needs to be pumped away after loading the trap. This has successfully been demonstrated for Europium and Chromium, where the buffer gas was pumped away in an impressive 20 seconds. Unfortunately, it was found that the lifetime of the CaH molecules in the trap was too short (at around 0.6 seconds) to allow the buffer gas to be pumped away. They attributed the shorter lifetime to the shallower trap depth, arising from the magnetic dipole moment of CaH being only around 1 Bohr-magneton (in comparison to the 6-7μ_B for Europium and Chromium). Nonetheless, this represented one of the first trapped samples of heteronuclear dipolar molecules. In our laboratory, we are currently working on a buffer gas source for YbF molecules as a potential alternative to a supersonic source for the EDM experiment.

1.2.2 Photoassociation / Feshbach resonance association

One possibility of avoiding the problem of cooling molecules is to associate laser cooled atoms. In order to conserve energy and momentum, two colliding atoms can only form a molecule if a third particle is present. The role can be fulfilled by a photon, resonantly absorbed to allow the atoms to bond in an electronic excited state [53]. Although the original proposal for using laser cooled Na was realised in 1993 [54], it also led to a whole family of ultra-cold homonuclear molecules to be formed using the same technique, including H_2 [55], He_2^* [56], Ca_2 [57], Li_2 [58], K_2 [59], Rb_2 [60, 61] and Cs_2 [62]. Although the production rate is comparable to bound-bound transition rates, the lifetime in the upper state is usually very low, at around a few ns. With the exception of Rb_2 and Cs_2 where the long-range excited states possess a double well structure favouring a bound-bound decay, most of these molecules decay back to being two separate atoms. As for the molecules which do decay to a bound state, optical pumping methods can be applied to vibrationally cool the molecules down to a single (preferably ground) state [63]. Attempts have been made to produce heteronuclear molecules this way, but have proven to be difficult due to unfavourable Franck-Condon overlaps [64]. Nonetheless, NaCs [65], KRb [66], RbCs [67] and LiCs [68] have been produced this way.

In recent years, another method for associating molecules has enjoyed great success. A Feshbach resonance occurs when an applied magnetic field Zeeman-shifts the energy of a bound state to cross over the threshold energy of the dissociation continuum. As the energy levels approach this resonance, the inelastic cross-section can be tuned to produce molecules upon collision [69]. This technique first produced ultra-cold samples of a range of homonuclear molecules, including $^{85}Rb_2$, $^{133}Cs_2$, $^{87}Rb_2$, $^{23}Na_2$, $^{40}K_2$ and $^{6}Li_2$ (see page 3 of [69]). The technique has since successfully produced heteronuclear ^{40}K-^{87}Rb [70, 71] and ^{41}K-^{87}Rb [72] molecules at the μK regime.

The advantage of these techniques is that the resulting molecules have the same temperature as the atoms they are made from. The limitation of photoassociation and Feshbach resonance techniques lies in the restricted number of species which are amenable to it, as both species need to be laser cooled. Ideally, a more widely applicable technique would be desirable.

1.2.3 Velocity selection

One possible solution is velocity selection [73]. Molecules from a room temperature source are guided using a curved quadrupole guide. The faster molecules have too much kinetic energy to be guided. However, some of the slower molecules at the tail end of the velocity distribution will be caught in the guide. These slow molecules are then spatially separated from the faster ones, producing a sample of slow moving molecules. Formaldehyde (H_2CO) and deuterated ammonia (ND_3) molecules were successfully produced using this technique, with an H_2CO flux of approximately 10^9/s and a longitudinal temperature of a few Kelvin. More recently, this technique has been used to study collisions between neutral CH_3F molecules and Ca^+ ions by placing an ion trap at the exit of the curved guide [74].

1.2.4 Stark deceleration

The method covered in this thesis involves bringing a supersonic pulse of cold molecules to rest using time-varying inhomogeneous electric fields. This technique is known as Stark deceleration. The supersonic pulse is first created by expanding a pressurized noble gas, typically Ar, Kr or Xe into vacuum via a nozzle. The result is a pulse travelling at several hundred m/s across the lab. However, the expansion cools the translational temperature in the centre-of-mass frame down to around 1K. The molecules of interest are mixed in with the noble gas or are formed just outside the nozzle. These molecules collide with the expanding jet and take on its characteristic velocity distribution. The result is a pulse of molecules which, although cold in its centre-of-mass frame, travel at several hundred m/s. The second step is to bring this pulse to rest. The Stark shift caused by inhomogeneous electric fields can be used to create potential hills along the molecular beam. When climbing a potential, the molecules will lose kinetic energy. When the molecules reach the top of a potential, the fields are switched off to prohibit an acceleration along the descent. Over this cycle, the molecules will have lost some kinetic energy. Repeating this procedure can eventually bring the molecules to rest.

The first successful experimental implementation of Stark deceleration reduced the speed of a pulsed beam of neutral metastable CO molecules from 225 m/s ($E_{kin} = 59\text{cm}^{-1}$) to 98m/s ($E_{kin} = 11\text{cm}^{-1}$) [2]. CO molecules in the metastable ($a^3\Pi$) state were used because of the large dipole moment (1.37 Debye) which is not present in the ground state. The Stark decelerator used in this experiment consisted of an array of 63 synchronously pulsed electric field stages, each designed to have a focusing effect which forced the molecules to stay together during the entire process.

A gas mixture of Xe and CO was expanded into vacuum through a pulsed valve cooled to 160K. This produced a pulse travelling at $\approx$ 230m/s. A few cm down the beamline, a UV laser excited the CO molecules to the first electronic excited state ($a^3\Pi$). The molecular pulse then travelled through a 5cm-long hexapole, which acts as a positive lens for molecules in the $M\Omega = -1$ state. Once the preparation of the molecular beam was complete, this was injected into the 35cm long decelerator. Each stage comprised two parallel rods, onto which a voltage of ±10kV is applied. This generated a field of 100kV/cm. The stages were alternately placed vertically then horizontally. This is to allow focusing in both transverse directions. Vertical stages were all electrically connected together, as were the horizontal ones. This setup caused a kinetic energy loss in the molecules of 0.8cm^{-1} per stage. Downstream from the decelerator, the time of flight profile (TOF) of the molecular pulse was observed. The TOF was recorded using a flat gold surface, from which electrons were emitted when a CO molecule collided with it. Increasing the number of stages used delayed the arrival of the pulse.

Since the original paper in 1999 [2], many low-field seekers have been decelerated using the same technique. These include OH [75, 76], ND_3 [77], NH [78], H_2CO [33] and SO_2 [79]. Once the molecules have been decelerated to rest, they can be confined in electric traps, e.g. [80], magnetic traps, e.g. [29] or storage rings [81, 82].

1.2.5 Alternating-gradient (AG) Stark deceleration

The Stark deceleration technique covered in the previous section was developed for molecules in 'weak-field seeking states', states in which the molecules are repelled from regions of high electric field strengths. Unfortunately, all ground state molecules are high-field seeking. The problem of decelerating ground state molecules is then that they are attracted to the electrodes, making it difficult to maintain a collimated beam (or indeed any beam at all). Furthermore, it is not possible to create maxima of electric field strength in free space [83]. In order to circumvent this problem, dynamic focusing schemes such as alternating-gradient (AG) focussing were proposed. Originally proposed for focusing ions in linear systems by Courant, Livingston and Snyder [84], AG focussing treats each electric field (in the case of [84], magnetic field) stage as a lens. This lens has the ability to focus the ions in one direction, but defocuses it by the same amount in a perpendicular one. A completely analogous treatment can be done for neutral molecules in inhomogeneous electric fields [85]. AG focusing of molecular beams was first achieved by Günther *et al.* [86] and Kakati and Lainé [87]. In 1999, high-field seeking Cs atoms in a fountain were focused and decelerated using time-varying electric fields [88]. In 2002, Bethlem *et al.* reported the first experimental implementation of this technique in a Stark decelerator [89], where an acceleration of the metastable CO molecular pulse from 275m/s to 289m/s as well as a deceleration from 275m/s to 260m/s was demonstrated. Following this, ^{174}YbF molecules were decelerated and 7% of the energy removed [90]. This consituted an improvement in the deceleration technique as YbF molecules are 7 times heavier than anything previously decelerated. This was also the first experiment to have decelerated ground state molecules using this technique.

1.2.6 Stark deceleration of Rydberg atoms

Stark deceleration is most effective when the species of interest has a large electric dipole moment to mass ratio. By exciting atoms or molecules to very high electronic states, the electric dipole moment increases by several orders of magnitude over that of the ground state. These 'Rydberg atoms/molecules' are therefore very attractive candidates for Stark deceleration. For Rydberg atoms, the Stark deceleration of supersonic beams of Ar [91] and H [92] have successfully been demonstrated. The H atoms were first excited to Rydberg states with principal quantum numbers n = 20-40 and were decelerated to zero velocity. They were then trapped in a two dimensional electrostatic trap [93]. In contrast to electric fields required to decelerate molecules in their low-lying electronic states, fields of a few kV/cm are sufficient to bring a 750m/s beam of H atoms to rest in a single deceleration stage.

In 2004, the Stark deceleration of H_2 molecules in the n = 17 state [94, 95] was also demonstrated. 13cm^{-1} out of the 570cm^{-1} of initial kinetic energy (corresponding to 2600m/s), was removed by applying an inhomogeneous field of around 700V/cm. Although promising, it is difficult to extend the deceleration process over several stages, as losses due to decay and state-changing processes become rapidly significant when working with Rydberg atoms/molecules. Nonetheless, since all molecules possess Rydberg states, this is an interesting route for providing cold samples of a large variety of molecules.

1.2.7 Optical Stark deceleration

Barker *et al.* showed that it is also possible to decelerate a beam of molecules in an optical field [96, 97]. A one-dimensional travelling optical lattice is formed by the interference pattern from two nearly counter-propagating optical fields. A molecule travelling through such a lattice feels a potential proportional to the intensity of the light. As the molecule climbs the potential 'hill', kinetic energy will be lost. By applying the lattice for the time needed by molecules to travel up the lattice site, the molecules are decelerated. With sufficient intensity, the potential can be made large enough to decelerate molecules to rest. The lattice was produced by two single-mode injection seeded, Q-switched Nd:YAG lasers, providing intensities of over 10^{11}W/cm^2. A key advantage of the technique is that it can be applied to a very wide range of molecules in a variety of states including the ground state. Using this technique, the deceleration of nitric oxide from 400m/s to 321m/s, benzene from 380m/s to 269m/s as well as xenon atoms were demonstrated.

1.2.8 Deceleration using pulsed magnetic fields

Another variant for decelerating a beam of molecules is to apply an external inhomogeneous magnetic field. The resulting Zeeman shift replaces the Stark shift created in electric fields to produce a force proportional to the gradient of the field. Using this technique, Raizen's group report the successful deceleration of neon atoms from 446m/s to 56m/s [98], and Merkt's group report a deceleration of H atoms from 313m/s to 225m/s [99]. Oxygen molecules have also been decelerated from 389m/s to 83m/s [100].

1.3 Sympathetic cooling of molecules using ultra-cold atoms

Apart from photoassociation and Feshbach resonance association, the techniques for manipulating molecules outlined in the previous section produce samples at temperatures of a few mK. In order to reach the ultra-cold regime, where the dipole-dipole interactions dominate, further cooling mechanisms will have to be harnessed. One proposal is to sympathetically cool the molecules using ultra-cold atoms. By overlapping trapped molecules with laser-cooled atoms, the molecules would collisionally cool to the temperature of the atoms. Although sympathetic cooling has successfully been demonstrated for ions [101] and atoms [102], it has never been applied to molecules. On a theoretical level, it is very hard to predict the outcome of such an experiment. The critical parameter is the ratio between elastic and inelastic cross sections, neither of which are well known. Calculations performed for OH-Rb collisions [103] indicates that inelastic scattering could be quite significant unless the molecules are in their absolute ground state. Also, indications are that atoms and molecules of similar mass would be favourable.

On the experimental side, the technology to trap Stark decelerated molecules and laser cooled atoms both exist. The challenge will be to overlap the two clouds. An experiment at the FHI is currently under way to sympathetically cool OH using laser cooled Rb. Recently, they have reported the successful trapping of Rb atoms in an AC electric trap [104].

Sympathetic cooling of molecules is also the long term aim of our experiment. We have chosen

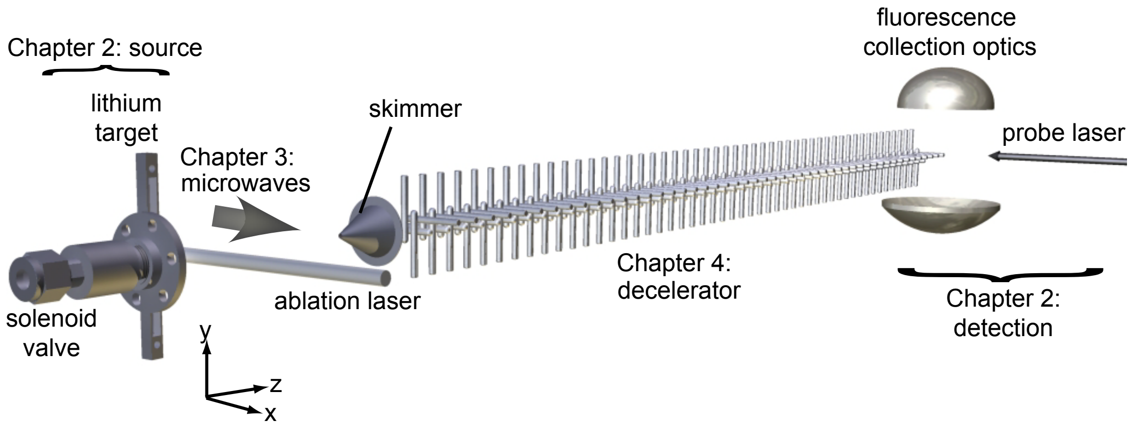

Figure 1.1: Schematic of the experiment, along with the relevant chapters associated with each step

Li as our atoms, as recommended by [103], and LiH as our molecules for the experiment. A Li MOT is currently under construction for this purpose. This thesis covers the molecular Stark deceleration.

1.4 Overview of the experiment

Our approach to producing samples of ultra-cold dipolar molecules is to start out by creating a cold pulsed supersonic beam. These pulses have translational temperatures of about 1K, but have a mean speed of several hundred m/s. The molecules are then brought to rest using a Stark decelerator. We then plan to cool this sample further through collisions with ultra-cold atoms. This thesis covers the formation and deceleration of cold LiH molecules. The experimental details are divided into 3 main sections: production and detection of LiH molecules, state preparation preceding deceleration and Stark deceleration itself. Figure 1.1 is a schematic of the experimental setup, illustrating its main components.

The very first step is the creation of a beam of cold LiH molecules (covered in chapter 2). This is achieved by laser ablation of Li into a supersonically expanding jet of Ar or Kr containing a small fraction of H_2. The Li reacts with the H_2 to form LiH which thermalises with the inert gas, adopting roughly the same speed and temperature as the carrier gas.

In the source, most of the molecules are produced in the absolute ground state. This is a strong-field seeking state - the energy decreases as the electric field increases. The decelerator only works for molecules in weak-field seeking states. Therefore, in the second step shown in figure 1.1 and discussed in detail in chapter 3, the molecules are prepared in the first rotationally excited state by driving the transition at 444GHz. This $|j = 1, m_j = 0\rangle$ state is weak-field seeking. The 444GHz microwaves are produced by a Gunn oscillator whose output frequency is quintupled using non-linear crystals.

Once the molecules are prepared in the desired state, they pass through a skimmer into a region of high vacuum. The beam then encounters the Stark decelerator (covered in chapter 4). The molecules are decelerated over 100 stages using time varying inhomogeneous electric fields of up to 100kV/cm.

In the final step shown in figure 1.1, the molecules are detected through time-resolved laser induced fluorescence (covered in chapter section 2). This involves pumping the molecules up to an electronically excited state and observing the spontaneous emission using a photomultiplier tube. The wavelengths required for the $X^1\Sigma^+$ to $A^1\Sigma^+$ transitions in LiH are around 370nm, which we obtain by frequency doubling a Ti:Sapphire laser. By time-resolving the fluorescence, we obtain the time-of-flight profile of the molecules. This is the primary signal in the experiment. An analysis of these time-of-flight profiles allows us to reconstruct the velocity distribution exiting the decelerator, and so understand the operation of the decelerator.

Chapter 2

Production and detection of cold lithium hydride beams

2.1 How to make a cold lithium hydride beam

It is well known that alkali hydrides are very difficult to make in gaseous form [105]. This is due to the large reaction barrier set by the binding energy of molecular hydrogen as shown in figure 2.1. In the case of LiH, this causes the single step reaction of $\mathrm{Li} + \mathrm{H_2} \rightarrow \mathrm{LiH} + \mathrm{H}$ to be endothermic by 2.05eV when the reactants are in their ground states. To make a cold beam, we are faced with the challenge of cooling the molecules down to a few Kelvin after having overcome a 24000K reaction barrier. This is why all previous experimental work on gas-phase LiH has been carried out in hot beams. Although there has been a previous effort to create a cold supersonic beam, the rotational temperature of the molecules turned out to be around 600K which is far higher than anticipated [106]. This chapter covers how a supersonic source with low rotational as well as translational temperature can be built.

2.1.1 Why supersonic beams are suited for Stark decelerators

The technique of supersonic expansion has been successfully harnessed for producing a wide range of cold molecular beams [107]. The phenomenon occurs when a highly pressurized gas is brought into contact with vacuum via an aperture. Thermodynamically, the cooling mechanism can be understood as an adiabatic expansion where all energy from the pressurized gas is converted into forward motion [108]. For molecules, both the internal ro-vibrational energy and their thermal kinetic energy is converted into a directed flow of energy out of the nozzle. Although the resultant beam has a relatively high velocity in the lab frame, typical translational velocity spreads correspond to a temperature of about a Kelvin. The gas jet is often pulsed for increased intensity [109, 110]. The result is packets of molecules in the same state travelling at the same speed.

These sources are ideal for Stark deceleration experiments. On one hand, the high phase-space density of the molecules allows a large number of them to be successfully matched to the decelerator's acceptance (see chapter 4). Furthermore, the restricted state population distribution

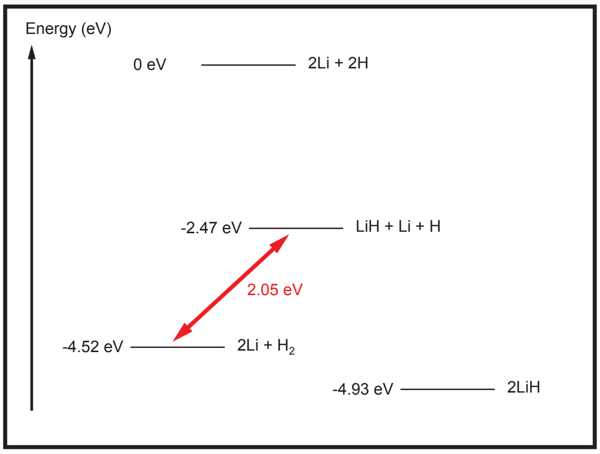

Figure 2.1: Energy level diagram showing the 2.05eV reaction barrier for producing LiH.

is a great advantage, as the Stark decelerator can only be set to be phase synchronous for molecules in a particular state (or states with identical Stark shifts). The Stark decelerator can then bring the high lab frame velocities down to rest. Under proper operating conditions, the result of combining a supersonic source and a Stark decelerator is a dense trappable sample of cold dipolar molecules [2, 111, 76, 77, 78, 33].

2.1.2 Supersonic beams

Successful Stark deceleration requires accurate knowledge of the molecules' velocity. The simplest way of calculating this is by equating the stagnation enthalpy (total usable energy behind the nozzle) of the pressurized gas and the final kinetic energy. This gives an approximate velocity for an ideal supersonic expansion:

$$H_0 = C_pT = \frac{1}{2}wv^2 \tag{2.1}$$

where H_0 is the stagnation enthalpy, C_p is the molar heat capacity at constant pressure, w is the molar mass of the gas pulse and v is its forward velocity after the expansion. In an ideal monoatomic gas, $C_p = C_v + R = \frac{5}{2}R$. We can replace C_p in 2.1 and rearrange the units to consider a single atom. The result is the following expression:

$$v_{T=0} = \sqrt{\frac{5k_bT}{m}} \tag{2.2}$$

where m is now the mass of the atom (in a.u.), T is the temperature before the expansion and k_b is Boltzmann's constant. The quantity $v_{T=0}$ is the terminal velocity which is reached when the temperature after the expansion is reduced to zero [108]. It is apparent from Eq.(2.2) that this terminal velocity is dependent on the initial temperature and the atomic mass of the gas. Given that our final aim is to have a stationary cloud of molecules, a low pulse velocity is obviously desirable. In order to lower the velocity of the gas pulse, we can either decrease the initial temperature or increase the mass of the gas. This is why most supersonic beam sources for Stark deceleration use a heavy inert carrier gas such as argon, krypton or xenon in which they seed their molecule of

Table 2.1: Terminal speeds for an ideal expansion for different carrier gases and initial temperatures

	mass (a.u.)	v_{pulse} in m/s (T=293K)	v_{pulse} in m/s (T=193K)
He	4	1745	1416
Ar	39.95	552	448
Kr	83.8	381	309
Xe	131.29	305	247

interest. As long as the volumetric ratio of carrier to seed is large, the resulting beam will take on the characteristic beam velocity of the carrier gas while pumping out the molecular internal energy through collisions. Table 2.1 shows the calculated pulse velocities for different carrier gases.

In a more rigorous treatment, the temperature T, velocity v and pressure P of the gas can be expressed in terms of the Mach number M, and are given by

$$\frac{T}{T_0} = \left(1 + \frac{\gamma - 1}{2} M^2\right)^{-1}, \tag{2.3}$$

$$v = M \left(\frac{\gamma R T_0}{W}\right)^{1/2} \left(1 + \frac{\gamma - 1}{2} M^2\right)^{-1/2} \tag{2.4}$$

and

$$\frac{P}{P_0} = \frac{T}{T_0}^{\gamma/(\gamma-1)} = \left(1 + \frac{\gamma - 1}{2} M^2\right)^{-\gamma/(\gamma-1)}, \tag{2.5}$$

where T_0 and P_0 are the temperature and pressure behind the valve, W is the atomic mass and γ equals 5/3 for a monatomic gas [108]. This is beneficial because the Mach number is only a function of the distance from the valve:

$$M = A \left(\frac{z - z_0}{d}\right)^{\gamma - 1} - \frac{\frac{1}{2}\left(\frac{\gamma+1}{\gamma-1}\right)}{A \left(\frac{z - z_0}{d}\right)^{\gamma - 1}}, \tag{2.6}$$

where $A = 3.26$ for Ar and Kr, and z_0/d is 0.075 [108]. In our experiment, d is 1mm. Eq.(2.6) is valid as long as $z/d \geq 2.5$. By substituting M in Eq.(2.3), (2.4) or (2.5) with the expression in Eq.(2.6), we can express the temperature, velocity and pressure as functions of the distance from the nozzle z. Figure 2.2 shows $M(z)$, $T(z)$, $v(z)$ and $P(z)$ for the first 25mm after exiting the nozzle. Initial temperature and pressure were set to 293K and 4 bar. As z increases, so does M. This results in a very rapid increase in velocity accompanied by a decrease in pressure and temperature. In the limit of $M^2 \gg 1$, T and P both vanish. In this limit, Eq.(2.2) is recovered from Eq.(2.4).

The values of M, T, v and P at the skimmer, placed 110mm downstream from the nozzle, calculated for a beam of Ar and Kr are shown in table 2.2. As shown later in this chapter (section 2.4.1), the final velocities are in good agreement with experimental observations. The temperature, however, will be found to be higher in the experiment. We believe one main cause to be the additional energy released during cluster formation, but further investigation is required.

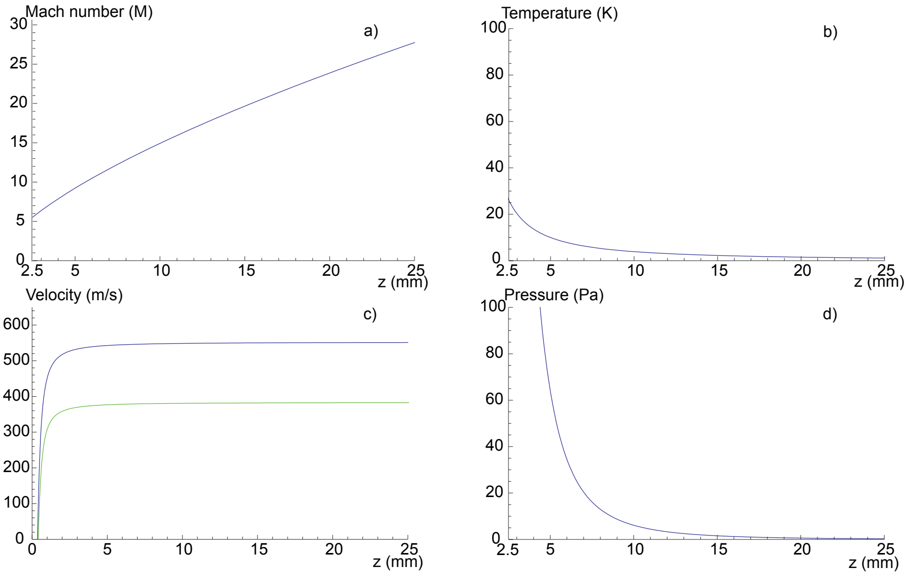

Figure 2.2: Dynamics of a supersonic expansion for $T_0 = 293$K and $P_0 = 4$ bar over the first 25mm of the expansion. a) Mach number, b) temperature, c) velocities (Ar in blue, Kr in green) d) pressure as functions of distance from the nozzle z in mm.

Table 2.2: Characteristic values for M, T, v and P at the skimmer ($z = 110$mm)

	Ar	Kr
M_{sk}	75	75
T_{sk} (K)	0.15	0.15
v_{sk} (m/s)	552	381
P_{sk} (Pa)	0.0027	0.0027

Further experimental parameters which may disturb this ideal expansion include pumping speed on the vacuum side, valve opening times, nozzle shape and heating in the solenoid of the valve (if such a valve is used). Heating can also occur if electric discharges or laser ablation is used for the creation of molecules (see sections 2.4, 2.9.1 and other work on deceleration [111]).

2.1.3 Methods for embedding molecules into supersonic sources used for Stark deceleration

In principle, it is possible to make supersonic gas pulses containing almost any molecule. This is done by seeding the molecule of interest into an inert carrier gas whose behaviour is understood (see section 2.1.2). The intensity of the beam then depends only on how efficiently the molecules can be embedded in the carrier gas. Experimentally however, there is a certain amount of black magic involved in order to achieve this. The most efficient method for embedding molecules varies greatly depending on the molecular species. The most ideal cases are when the molecules of interest are a gas, or have high vapour pressure at room temperature [2, 80]. For other species, gaseous precursors of the molecule can be seeded in the carrier, which can then be subjected to an electric

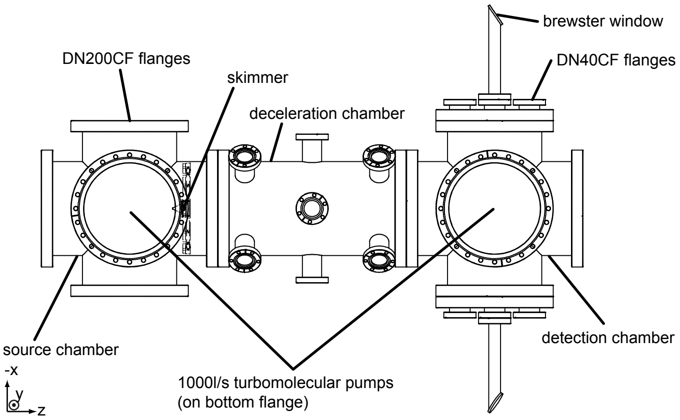

Figure 2.3: The 3 vacuum chambers viewed from the top

discharge [75]. In more awkward cases where one or more of the precursors are solids at room temperature, one can resort to laser ablation of the solid placed next to the nozzle exit [112]. The plume formed by the ablation is captured by the gas jet when the two are superimposed. This is how we make our LiH. However, it is also possible to imagine many other, often even more complex, schemes which may yield high intensities. The yield of a particular beam source is difficult to predict a priori, so I spent quite some time trying some of them out. This chapter covers the apparatus we built and the data showing cold LiH which we obtained from it. In the second half, I discuss several other production methods I attempted in the hope of increasing the LiH flux.

2.2 Hardware

2.2.1 Vacuum system

The entire experiment is housed in the three vacuum chambers shown in figure 2.3. Two DN200CF 6-way crosses act as source and detection chambers, while a custom built cylinder designed for housing the decelerator is sandwiched between the two. Details on the decelerator chamber are given in chapter 4. For the early part of the project, while the source was being optimized, the middle chamber (along with the decelerator) was absent. Two 1000l/s turbomolecular pumps evacuate the chambers. A conical skimmer, with an opening of diameter 2mm, acts as a differential aperture between the source chamber and the other two chambers. With the source pulsed at a 10Hz repetition rate, typical pressures in the source and detection chambers are 10^{-5}mbar and 2×10^{-7}mbar respectively. When the source is not operating, the typical pressure is 5×10^{-8}mbar throughout. A rotary pump provides a rough vacuum of 5×10^{-3}mbar on the exhaust side of the turbomolecular pumps. With the exception of the rotary pump, the entire system sits on a Bosch frame.

2.2.2 Laser systems

The Li is ablated using light from a Nd:YAG laser at a wavelength of 1064nm. Most of the time, the spot size is focused to match the size of the target. All the data is taken using one of two Nd:YAG lasers. The first of the two Nd:YAG lasers (I will refer to this one as YAG1) is a Spectra Physics INDI-30 capable of delivering up to 450mJ at 1064nm or 110mJ at 355nm over a 7ns pulse. YAG1 also offers a 'long pulse mode' where it delivers a 150μs long train of 1μs long pulses. The use of this feature in our experiment will be discussed in section 2.9.6. The second (YAG2) is a Continuum MiniLite laser, which delivers up to 100mJ at 1064nm. In section 2.9.5, we investigate the effect of dual ablation where we use two pulses, one from each YAG, to ablate the target.

The probe laser is a single-mode CW Ti:Sapphire laser (Coherent MBR110) whose output is frequency-doubled by an LBO crystal in a build up cavity (Coherent MBD200). The Ti:Sapphire laser is pumped by an 8W frequency doubled Nd:YVO$_4$ laser (Coherent Verdi V8). The MBR-110 is a ring cavity laser with a linewidth below 1MHz. Coarse laser frequency tuning is achieved with a birefringent filter (BRF). This makes the polarization of the light frequency-dependent, resulting in losses for light at frequencies which do not match the cavity's preferred axis of polarization. A thin Fabry-Perot etalon then selects out a single longitudinal mode of the cavity. The reflection from the etalon is fed back to ensure that the laser is locked to a particular cavity mode. In order to stabilize the frequency of this mode, a small fraction of the laser's output beam is fed to a temperature stabilized reference cavity. The error signal from this cavity controls Brewster plates mounted on galvo-drives, as well as a piezoelectric crystal holding one of the mirrors of the laser cavity. The Brewster plates provide long term stability, while the piezo-mounted mirror compensates for rapid changes in cavity length.

The frequency doubler cavity is also a ring. This cavity stores the pump light in order to increase the output from the non-linear crystal. The doubled light does not see the cavity at all. The aim is therefore to make sure the cavity stays on resonance with the input beam. This is done by using a Hansch-Couillaud locking scheme [113]. While the Ti:Sapphire laser is scanned the internal electronics keep this cavity on resonance such that no external scanning is required.

Typical output from the Ti:Sapphire laser and the doubling cavity are about 450mW and 15mW respectively. For our set of mirrors and birefringent filter inside the laser cavity, the tuning range is about 40nm around 370nm.

2.2.3 Computer control

The entire experiment is controlled from a desktop computer fitted with National Instruments PCI-6534 pattern generator and PCI-6251 data acquisition boards. This ensures the proper scanning of lasers, operation of the source and decelerator as well as recording of data. Furthermore, a GPIB board allows us to scan the 444GHz microwave frequency. An in-house C# program known as ScanMaster (mostly written by J.J. Hudson and M.R. Tarbutt) operates the entire experiment.

A block diagram of the experiment is shown in figure 2.4. Upon receiving TTL trigger pulses from the computer, the valve is opened and the YAG is fired at the Li target. This leads to the creation of a cold pulse of LiH. Figure 2.4 also shows the detection setup. The photocurrent

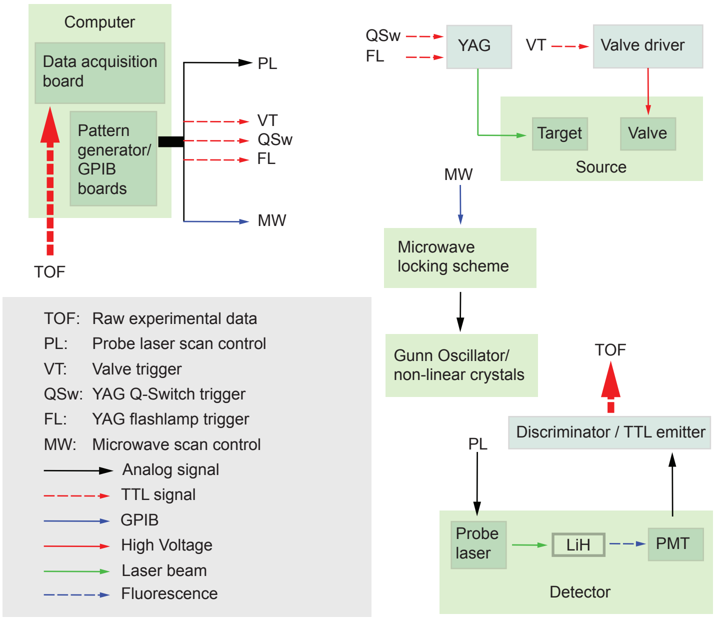

Figure 2.4: Block diagram showing the elements of the experiment, the control and acquisition systems.

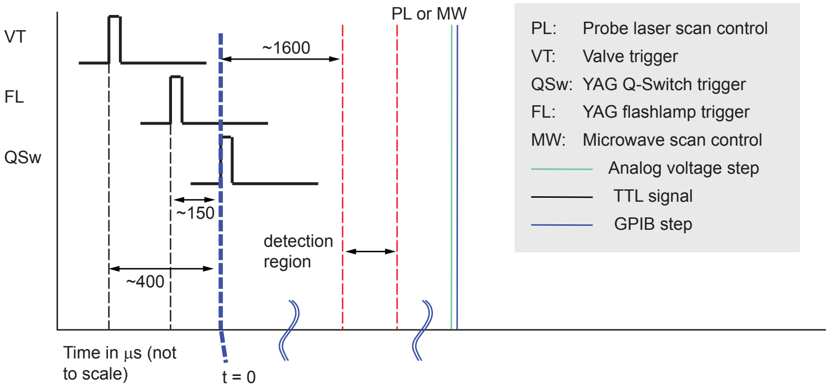

Figure 2.5: Event-chain diagram of one experimental cycle.

emitted by the PMT is converted to TTL and sent to the data acquisition board. This allows a time-resolved photon-count rate to be measured. The detection time is gated around the approximate arrival time of the molecules in order to reduce noise. After the pulse travels past the detector, experimental parameters such as probe laser frequency, microwave frequency and source trigger timings can all be stepped in preparation for the next shot.

The timing sequence for one experimental cycle is illustrated in figure 2.5. The Q-switch of the Nd:YAG laser is taken to be $t = 0$, as it is the closest approximation to when the molecules are formed. The valve is triggered first at $t \approx -400\mu$s, followed by the flashlamps of the Nd:YAG at $t \approx -150\mu$s. The data acquisition board records the photon count rate for a typical time window of 1ms around the transit time of the molecules. Finally, experimental parameters can be stepped as required, in preparation for the next cycle. Typically, this cycle is repeated at a rate of 10 to 15 Hz. The probe laser and microwaves are left on for the duration of the cycle.

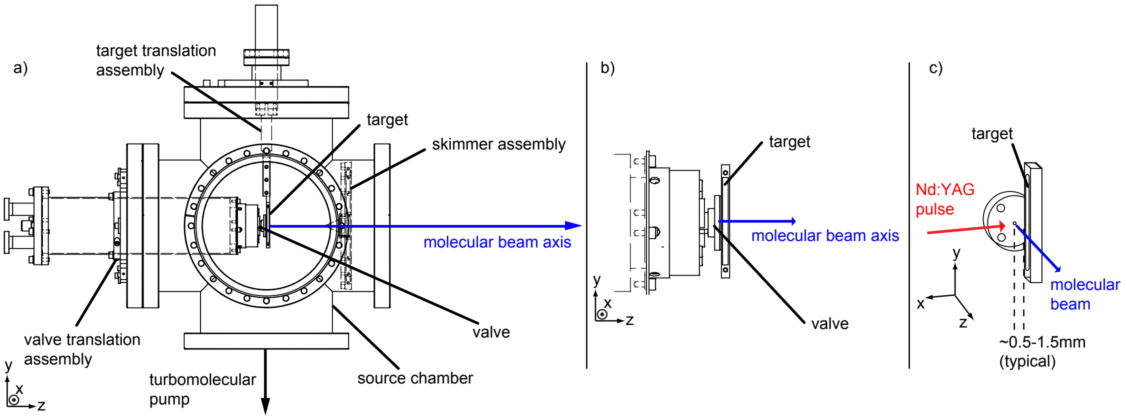

Figure 2.6: a) Side view of experimental layout in source chamber. b) Close-up of expansion region. c) Rotated view of expansion region.

All the data analysis is carried out using Wolfram Research's Mathematica.

2.3 The source: some more hardware

The molecular source lives inside the first DN200CF 6-way cross evacuated by a Leybold 1000l/s MagLev turbomolecular pump as shown in figure 2.6.

The valve, a General Valve Series 99 (orifice size 0.8mm) positioned at the centre of the chamber, is attached to a translational assembly. This assembly gives us full 3 dimensional control over the position of the valve with high accuracy. Furthermore, the design allows the valve position to be adjusted within a range of ±5mm in the x-y plane without breaking vacuum. The carrier gas seeded with molecular hydrogen (with a ratio of 98% to 2%) is held behind this valve, at a typical pressure ranging between 2 and 6 bar. The assembly is also designed for cold nitrogen gas to flow around the body of the valve for temperature regulation, but this feature was never used.

A pot of width 3mm in the z-direction and 50mm in the y-direction filled with lithium is attached to a translational assembly on the top of the chamber. The translational range in the x-z plane is ±5mm. This allows us to vary the position of the target without affecting the valve or the gas jet. The shape of the pot is deliberately much longer than the vertical size of the gas jet. By moving the translational feedthrough's position, we are able to reach new spots on the target when needed. The range of the linear feedthrough is 50.8mm, allowing the entire length of the pot to be used.

The valve is operated by applying a voltage pulse of around 250V for 300μs. The magnetic field created by the solenoid inside the valve pulls the poppet back, allowing the gas to flow. The most dense part of the beam is then picked off by a 2mm diameter skimmer placed 110mm downstream from the centre of the chamber.

In order to align the Nd:YAG correctly with the target, the beam is sent into the source chamber at low pulse energy. The beam should be in the horizontal plane, at an angle perpendicular to the gas jet (along the $-x$ axis, at $y = 0$). The focal point of the YAG pulse must be displaced from the window, as this may damage the latter. Turning up the YAG energy and looking into the vacuum chamber (wearing goggles!) from a viewing window on the top flange, it is possible to observe the ablation plume caused by the YAG pulse. The plume is a very distinct glowing jet. If the YAG pulse is too far upstream (-z direction), the stainless steel on the valve assembly will be ablated instead, producing a faint yellow jet. Steering the YAG beam over to the Li should produce a bright red ablation plume.

The next step is to synchronize the YAG pulses with the arrival of the gas pulse. If the delay between the valve and the YAG triggers are set correctly (typically a few hundred μs) and the YAG pulse is hitting the target at the correct height, the ablation plume will noticeably change direction, bending downstream along z. This is due to the carrier gas hitting the plume and carrying away a fraction of the atoms. The YAG beam path can then be walked to maximize this effect. Once this is done, the YAG energy must be turned down until the plume is only barely visible. Experimentally, this was found to be the optimum condition for finding a LiH signal. Once a signal is observed, all parameters can be tweaked again to optimise for the signal.

2.4 The results. We have a source!

2.4.1 The gas pulse

The first thing to verify is that the source is aligned with the skimmer and detector downstream. This was done by placing a fast ionization gauge (FIG) 330mm downstream from the skimmer. This is an ionization gauge which has a temporal response of about 5μs. Using this, we can observe the temporal profile of the gas jet. The result of optimizing the valve's transverse position is shown in figure 2.7. The solid line shows the time of flight profile from the gas pulse. The dashed line shows what happens to the gas pulse as the YAG is fired. From the solid line, the temperature and velocity of the gas pulse can be deduced. A full discussion of how to do this is presented in section 2.4.2. Using Eq.(2.11) for a gas pulse with zero initial width, we find that the velocity and temperature is 582m/s and 3.68K. Our best guess for the initial pulse width is $\approx 150\mu$s. Factoring this into Eq.(2.14) brings the temperature down to 1.4K. Although this is higher than calculated estimates from section 2.1, it is in good agreement with the translational temperature of the LiH molecules, as will be shown below.

The dashed temporal profile shows us that the lithium atoms, which were ablated by the Nd:YAG laser, hit the gas, causing a slight indentation in the jet which grows as the Nd:YAG energy is increased. The temporal position of the indentation can be varied by changing the delay between the valve and YAG trigger pulses. At full Nd:YAG energy (around 450mJ), this dip reaches down to the base pressure level, indicating that atoms are punching a hole through the gas jet. It is important to note that this dip is still visible in spite of the dispersion which occurs during the free flight to the FIG. This adds testimony to the pulse's low temperature in its rest frame. It is also worth noting that the Li atoms only interact with a fraction of the entire gas jet. This will become more relevant in section 2.9.5.

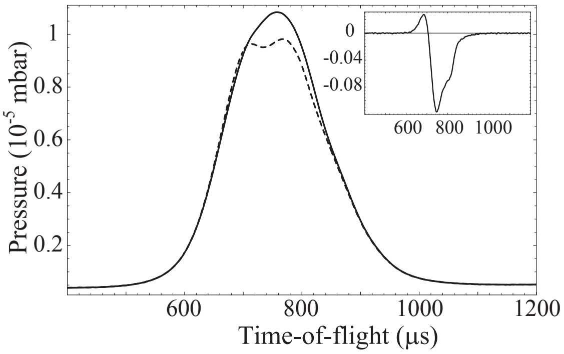

Figure 2.7: Gas pulse observed on the fast ionization gauge placed 330mm downstream from the source. The solid/dashed line is when the Nd:YAG is turned off/on. The inset shows the difference between the two.

2.4.2 The molecular pulse

Typical time-of-flight (TOF) datasets obtained from a beam of LiH are shown in figure 2.8. Figure 2.8 a) shows the TOF obtained using Kr as a carrier gas, while b) shows a TOF using Ar. This is the basic format for all our raw LiH data. These signals were obtained by laser induced fluorescence detection of the LiH molecules, as will be explained in section 2.5.

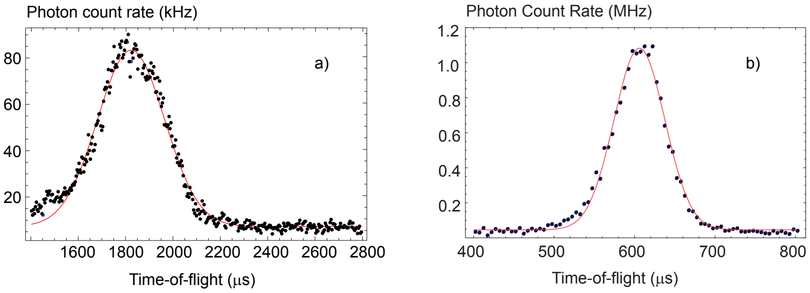

Figure 2.8: The time of flight profile of LiH molecules obtained when using a) krypton b) argon as a carrier gas. The arrival times and widths give the temperature and mean velocity to be 417m/s and 0.99K for krypton and 628m/s and 1K for argon.

From the arrival time of the molecules, knowing the distance from the source to the probe laser, the mean velocity can be extracted trivially. These are found to be 417m/s and 628m/s for Kr and Ar carrier gases respectively. Note that the data shown in figure 2.8 b) was taken before the decelerator and its chamber were built into the experiment.

In order to extract the translational temperature of the pulse, we construct a model for the time dependent signal $h(t)$ obtained from a LIF detector placed at a distance L away from the source [112, 114]. This signal, $h(t)$, is the result of a sum over the contributions from each slice of molecules formed at positions s and times t_s at the source. If a molecule is formed at s at time t_s, the resulting signal is given by $h(t, t_s, s)$. A function $g(t_s, s)$ describes the spatio-temporal distribution of molecules at the source. The total signal $h(t)$ is then the integral over the product of these two terms:

$$h(t) = \int_{-\infty}^{\infty}\int_{-\infty}^{\infty} h(t, t_s, s) g(t_s, s) dt_s ds. \tag{2.7}$$

In order to obtain an expression for $h(t, t_s, s)$, we use the expression for the flux of molecules in a supersonic jet with beam-axis velocities between v and $v + dv$ [115]:

$$f(v)dv = Av^3 e^{-M\frac{(v-v_0)^2}{2k_b T}} \tag{2.8}$$

where M is the mass, T is the translational temperature, v_0 is the central velocity and A is a constant. Applying a change of variables $v = (L - s)/(t - t_s)$ gives the following expression for $h(t, t_s, s)$:

$$h(t, t_s, s) = \frac{A(L-s)^4}{(t-t_s)^5} \exp\left(\frac{-Mv_0^2}{2k_b T}\frac{(t_0 - s/v_0 - t + t_s)^2}{(t-t_s)^2}\right) \tag{2.9}$$

where t_0 is the central arrival time L/v_0. We then simplify Eq.(2.9) by assuming the detector is far away from the source, i.e. $s \ll L$ and $t_s \ll t_0$. The time range of interest is smaller than the central arrival time, so we can write $t \approx t_0$ except in the numerator of the exponent. This simplifies equation (2.9) to

$$h(t, t_s, \rho) = \frac{AL^4}{t_0^5} \exp\left(\frac{-4 \ln 2\ (t_0 - \rho - t + t_s)^2}{w^2}\right), \tag{2.10}$$

where $w^2 = 8 \ln 2\ k_b T t_0^2 / M v_0^2$. s has been expressed in units of time $\rho = s/v_0$ to match the data.

We do not have any information on the spatio-temporal distribution $g(t_s, \rho)$. The simplest approximation would therefore be to express it as two Kronecker delta functions $g(t_s, \rho) = \delta(t_s)\,\delta(\rho)$, implying that the molecules were all created at the origin ($s = t = 0$). This immediately reduces Eq.(2.7) to the following:

$$h(t) = \frac{AL^4}{(t_0)^5} \exp\left(\frac{-4 \ln 2\ (t_0 - t)^2}{w^2}\right). \tag{2.11}$$

Here, the entire width of the pulse w is treated as being due to the finite translational temperature of the molecules. Solving for T in the expression for w then provides an upper bound on the temperature by ignoring source effects.

A more realistic approach is to treat $g(t_s, \rho)$ as a Gaussian in both space and time:

$$g(t_s, s) = \frac{4 \ln 2}{\pi \Delta_{t_s} \Delta_\rho} \exp\left(\frac{-4 \ln 2\ t_s^2}{\Delta_{t_s}^2}\right) \exp\left(\frac{-4 \ln 2\ \rho^2}{\Delta_\rho^2}\right). \tag{2.12}$$

The logarithms which appear in front of various terms are only inserted to ensure that the widths w, Δ_{t_s} and Δ_ρ correspond to full widths at half maxima. Integrating Eq.(2.7) using the expressions for $h(t, t_s, \rho)$ and $g(t_s, \rho)$ from Eq.(2.10) and (2.12) now gives

$$h(t) = \frac{AL^4}{(t_0)^5} \frac{w}{w'} \exp\left(\frac{-4 \ln 2\ (t_0 - t)^2}{w'^2}\right) \tag{2.13}$$

where

$$w'^2 = w^2 + \Delta_{t_s}^2 + \Delta_\rho^2. \tag{2.14}$$

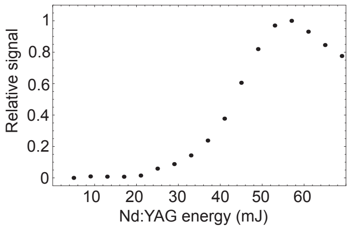

Figure 2.9: LiH signal as a function of Nd:YAG energy

This shows that the width obtained in a TOF is the quadrature sum of a contribution from dispersion due to the finite temperature of the molecules (w) and a contribution from their spatio-temporal profile at the source (Δ_{t_s} and Δ_ρ).

Having two spatially separated detectors allows w to be measured directly, giving an accurate measurement of the translational temperature [114]. However, we only have one detection region to probe from. Instead, we were able to measure the temporal width t_s of the source by using a dual ablation technique (see section 2.9.5), where we measured the interaction time to be 5μs long. The spatial width was measured in a different experiment and found to be less than 8.5mm [114]. In figure 2.8 a), w' is measured to be around 334μs. The discrepancy between using point source and Gaussian source profiles for Eq.(2.7) is therefore $1 - w'^2/(w'^2 - \delta_{t_s}^2 - \delta_\rho^2) \approx 1\%$. Given that this difference is very small, translational temperatures quoted in the rest of this thesis will always refer to the upper bound, i.e. where $w' = w$. For both datasets shown in figure 2.8, the temperature was found to be 1K, in good agreement with the gas pulse temperature.

Another source of uncertainty is also the temporal resolution of our detector. However, this is ignored here as the contribution is small (see section 2.5).

2.4.3 Optimizing the beam

Two critical parameters should be mentioned: the Nd:YAG energy and the timing between the valve opening and the Nd:YAG's Q-switch firing. Figure 2.9 shows the molecular signal plotted against the amount of Nd:YAG energy used for the ablation. This shows an optimum energy of around 55mJ. For a spot size of 4mm in a 10ns long pulse, this corresponds to an intensity of 44MW/cm^2. Too little YAG energy produces no signal, as it fails to ablate any Li atoms. Too much YAG energy also causes a reduction in the signal, as the carrier gas pulse appears to have a critical density of Lithium atoms it can 'catch', beyond which the presence of more Li atoms does not affect the yield, or damages the gas pulse.

Figure 2.10 shows the signal as a function of the timing between the valve trigger and the Q-switch trigger pulses. There is quite naturally an optimum value for this parameter, which was found to be 380μs. Note that the optimum value in figure 2.10 is approximately 100μs earlier than the value required to centre the YAG-induced hole in the FIG signal, as shown in figure 2.7. This implies that LiH formation is favoured in the front of the gas pulse.

In the experiment, a voltage pulse of typical amplitude 250V is applied to the valve for a typical duration of 300μs. The optimum voltage and pulse duration are correlated such that a higher/lower voltage for a shorter/longer time seems to yield a similar total LiH flux, although the temperature

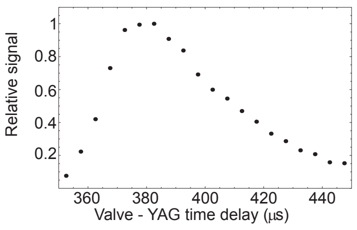

Figure 2.10: LiH signal as a function of valve to Q-Switch timing

of the pulse is affected. We believe this to be because the LiH flux depends on the amount of gas emitted from the valve, which remains constant for a range of combinations of voltages and pulse lengths. Finally, maximizing the 'plume capture' effect described in section 2.1 is very useful for optimizing the ablation laser beam path.

It is important to remember however, that all of these values are only meant to be a starting point for anyone making a molecular beam source. The optimum parameters tend to drift over different time-scales. On a time-scale of minutes or hours, the optimal Nd:YAG energy increases as the quality of the target deteriorates. As the energy is increased the lithium atoms end up hotter and the temperature of the beam increases. One can sometimes bring the temperature of the pulse back down by increasing the backing pressure behind the valve (typically > 2bar). The valve to Q-switch timing is also slightly dependent on the target's position along the beam axis, as well as the YAG beam's position on the target. These sensitivities can be minimized by making the Nd:YAG beam profile bigger while keeping the intensity constant. The optimum voltage applied to the valve varies, both in amplitude and length of pulse on a much longer time-scale of weeks. These are correlated to the backing pressure and the condition of the poppet. Shorter voltage pulses of higher amplitude tend to produce colder pulses, but put a higher constraint on the valve to Q-switch timing and Nd:YAG energy. Finding a 'good spot' on the target and optimizing all the other parameters can be a bit of a challenge, especially as the target approaches the end of its lifespan. All these parameters are tweaked several times a day to ensure a good LiH signal.

Finally, it should also be mentioned that we do not fully understand the formation mechanism for our beam. For instance, we observe a LiH signal after several days of taking the H_2 seed out of the carrier gas, even after flushing out the gas-handling system. Also, target spots seem to improve after being left as fallow: we observe that returning to a used spot can often produce a reasonable signal. I will return to this issue in section 2.9, as some of the alterations to the source also provide a few more clues about the mysterious reaction mechanism.

2.5 How to detect lithium hydride in a beam

Having covered the production of the beam in previous sections, I will now cover the state selective detection of LiH molecules in a beam.

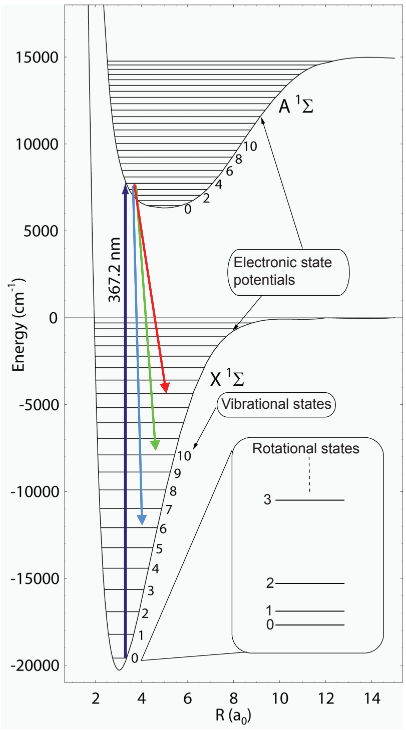

Figure 2.11: Energy level structure of LiH. The vibrational states within the $X^1\Sigma^+$ and $A^1\Sigma^+$ states are shown. In the inset, the ground vibrational state is magnified to show the first few rotational states. In laser-induced fluorescence, the laser is tuned to a resonance between two electronic states. A molecule which is excited by the laser then decays back down, releasing a photon which we observe on a PMT.

2.5.1 Laser-induced fluorescence

Laser-induced fluorescence (LIF) is a common method for detecting both atomic and molecular beams. It forms the base of our detection system. The idea is to excite the population of a particular state by subjecting it to a laser beam whose frequency corresponds to a transition to an upper electronic state. The spontaneous emission from the upper state gathered at a photomultiplier tube (PMT) provides information on the population of the initial state, as is illustrated in figure 2.11.

2.5.2 Energy level structure of lithium hydride

The energy level structure of LiH is shown in figure 2.11. This energy level structure is more complex than for atoms, owing to the extra nuclear degrees of freedom. The energy difference between electronic states is very large. For instance, the ground state of the $X^1\Sigma^+$ potential and the ground state of the $A^1\Sigma^+$ potential exceeds 25000cm^{-1}. This is in contrast to vibrational states which have a typical separation of the order of 1000cm^{-1}. The rotational state separation is even smaller, typically ranging in the tens of wavenumbers. This section is devoted to calculating transition frequencies and amplitudes of the LiH molecule, thereby briefly outlining some basic

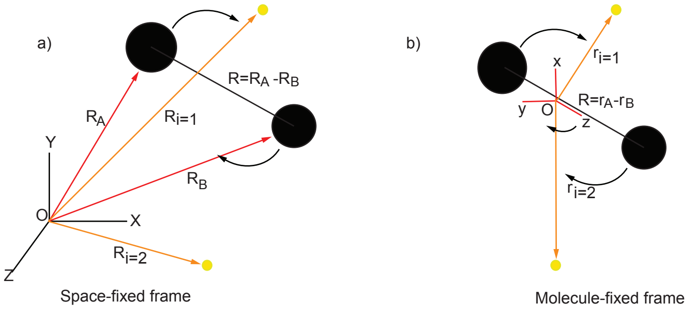

Figure 2.12: Illustration of the molecule in a) the space-fixed frame and b) molecule-fixed frame.

concepts in molecular physics. Any reader interested in a more detailed treatment of the theory of diatomic molecules is directed to the very extensive literature, including Herzberg [116], Brown and Carrington [117] or Joachain and Bransden [118]. In this thesis, we consider a diatomic molecule of N electrons at positions $\mathbf{R}_i$ in the laboratory frame with nuclei A and B of masses M_a and M_b, with charge Z_a and Z_b at positions $\mathbf{R}_a$ and $\mathbf{R}_b$ as shown in figure 2.12 a).

It is most desirable to write the full Hamiltonian for this system as the sum of an electronic Hamiltonian H_e and a nuclear Hamiltonian H_N, such that

$$\hat{H} = \hat{H}_e + \hat{H}_N, \tag{2.15}$$

where H_N and H_e are given by

$$\hat{H}_N = -\frac{\hbar^2}{2\mu}\nabla_R^2 + \frac{Z_a Z_b e^2}{4\pi\epsilon_0 R} \tag{2.16}$$

and

$$\hat{H}_e = \sum_{i=1}^{N} -\frac{\hbar^2}{2m}\nabla_i^2 + \sum_{i<j}\frac{e^2}{4\pi\epsilon_0 R_{ij}} - \sum_{i,\alpha}\frac{Z_\alpha e^2}{4\pi\epsilon_0 R_{i\alpha}}. \tag{2.17}$$

μ is the reduced mass of the nuclei, α equals a or b and R_{ij} is $\mathbf{R}_i - \mathbf{R}_j$. Small correction terms have been neglected in Eq.(2.17) (see [117]). The full Schrödinger equation is given by

$$\hat{H}\Psi = \left(\hat{H}_e + \hat{H}_N\right)\Psi = E\Psi, \tag{2.18}$$

where Ψ is the overall molecular wavefunction. Having separated the Hamiltonian, the next natural step would be to apply a separation of variables, which requires that $[\hat{H}_e, \hat{H}_N] = 0$. As $\hat{H}_e$ is a function of the nuclear positions, this is in general not the case. In order to proceed, Born's adiabatic approximation is made.

Although the Coulomb interaction between electrons and nuclei are of the same order of magnitude, their masses differ significantly. In LiH, $M_{a,b}/M_e$ exceeds 10^4. It can therefore be assumed that nuclear motion is very slow compared to electronic motion. Born's adiabatic approximation uses this to assume that the electrons follow the nuclei 'adiabatically' as the nuclei slowly change their position. In order to develop this approximation, it is natural to change the coordinate system from the space-fixed (or lab-fixed) frame to a frame gyrating with the internuclear axis, the ‘molecule-fixed’ frame. It can be shown that in the most general case, the two coordinate systems are related by 3 Euler angles θ, ϕ and χ [119]. We also fix the origin at the centre-of-mass of the nuclei, thus ignoring any translational motion of the entire molecule. In this coordinate system, the nuclear effect on the electrons is reduced to a single parameter $R = \mathbf{R}_a - \mathbf{R}_b$. Furthermore, the adiabatic approximation allows R to be treated as a constant when solving $\hat{H}_e$. For a particular value of R, $[\hat{H}_N, \hat{H}_e]$ then equals 0, allowing us to proceed with the separation of variables. An illustration of the relevant vectors is shown in figure 2.12. In the molecule-fixed frame, Φ^n are eigenfunctions of the electronic Hamiltonian, (which must also be written in the molecule-fixed frame, see [117]), which satisfy

$$\hat{H}_e \Phi^n \left(R, r_i, ..., r_N\right) = E_n(R)\ \Phi^n \left(R, r_i, ..., r_N\right). \tag{2.19}$$

The wavefunctions Φ^n taken at a particular value of R form a complete orthonormal set.

Next, define a set of functions $\psi^n(R)$ which describe the axial (vibrational) motion of the nuclei in the molecule-fixed frame. We then expand the total wavefunction $\Psi\left(R, r_i, ..., r_N\right)$ in terms of the basis set Φ^n.

$$\Psi\left(R, r_1, ..., r_N\right) = \sum_n \psi^n\left(R\right) \Phi^n \left(R, r_i, ..., r_N\right), \tag{2.20}$$

where $\psi^n(R)$ now resembles an expansion coefficient with a parametric dependence on R.

Finally, in order to insert this wavefunction back into the space-fixed Hamiltonian Eq.(2.15), the rotation of the molecule-fixed frame with respect to the lab frame must be accounted for. This is done by including an additional term $\mathcal{H}\left(\theta, \phi, \chi\right)$ in Eq.(2.20). This is the rigid rotor wavefunction for symmetric top molecules, given by

$$\mathcal{H}\left(\phi, \chi\right) = \left(\frac{2J+1}{8\pi^2}\right)^{1/2} \mathcal{D}^{(J)}_{m_J, K}\left(\theta, \phi, \chi\right)^*, \tag{2.21}$$

where $\mathcal{D}^{(J)}_{m_J, K}\left(\theta, \phi, \chi\right)^*$ is a Wigner rotation matrix [117]. J is the rotational angular momentum quantum number, K is its projection onto the gyrating molecule-fixed frame and m_J is its projection onto the lab fixed frame. In the case of a symmetric top molecule, the additional quantum number K arises because of rotations with respect to the molecule-fixed frame, which can occur from nuclei lying off the central axis of the molecule. In a diatomic molecule, K is always 0. The ansatz for the full wavefunction in space-fixed coordinates thus takes the form

$$\Psi\left(R, r_1, ..., r_N, \theta, \phi, \chi\right) = \sum_n \psi^n\left(R\right) \mathcal{H}\left(\theta, \phi, \chi\right) \Phi^n \left(R, r_i, ..., r_N\right). \tag{2.22}$$

Inserting Eq.(2.22) into Eq.(2.18) gives

$$\left(\hat{H}_e + \hat{H}_N - E\right) \sum_n \psi^n\left(R\right) \mathcal{H}\left(\theta, \phi, \chi\right) \Phi^n \left(R, r_i, ..., r_N\right) = 0, \tag{2.23}$$

or re-writing Eq.(2.23) in Dirac notation,

$$\left(\hat{H}_e + \hat{H}_N - E\right) \sum_n |v\rangle_n |J, m_J\rangle |n\rangle = 0 \tag{2.24}$$

where $\psi^n(R) \rightarrow |v\rangle_n$, $\mathcal{H}(\theta, \phi, \chi) \rightarrow |J, m_J\rangle$ and $\Phi^n(R, r_i, ..., r_N) \rightarrow |n\rangle$. In the Born-Oppenheimer approximation, the electronic, vibrational and rotational energy levels are treated as being separate, owing to the difference in energy scales involved. This approximation arises quite naturally once the adiabatic approximation is applied: electronic motion is instantaneous in comparison with vibrations in the molecule-fixed frame, while rotation arises only from a coordinate transformation.

Multiplying Eq.(2.24) by $\langle n'|$ gives

$$\langle n'| \left(\hat{H}_e + \hat{H}_N - E\right) \sum_n |v\rangle_n |J, m_J\rangle |n\rangle = 0. \tag{2.25}$$

By expanding Eq.(2.25), we obtain

$$\sum_n \langle n'|\hat{H}_N|n\rangle |v\rangle_n |J, m_J\rangle + \langle n'| \left(\hat{H}_e - E\right) |n\rangle |v\rangle_n |J, m_J\rangle = 0. \tag{2.26}$$

Here, we make the Born-Oppenheimer approximation which ignores the dependence of $|n\rangle$ on nuclear coordinates. Thus, remembering that $\langle n'|n\rangle = \delta_{n,n'}$ and that $\hat{H}_N$ is not a function of electronic coordinates, Eq.(2.26) simplifies to

$$\hat{H}_N |v\rangle_n |J, m_J\rangle + (E_n(R) - E) |v\rangle_n |J, m_J\rangle = 0, \tag{2.27}$$

where Eq.(2.19) was used to obtain $E_n(R)$. Finally, substituting Eq.(2.16) into Eq.(2.27), we obtain

$$-\frac{\hbar^2}{2\mu} \nabla_R^2 |v\rangle_n |J, m_J\rangle + (V + E_n(R) - E) |v\rangle_n |J, m_J\rangle = 0 \tag{2.28}$$

where $V = Z_a Z_b e^2 / 4\pi\epsilon_0 R$. In the Born-Oppenheimer approximation, the ‘electronic wave equation’ of Eq.(2.19) is solved at different values of R to obtain $E_n(R)$. These result in potential energy curves which for LiH are shown in figure 2.11. They are then used in the ‘nuclear wave equation’ Eq.(2.28) as potentials within which the molecule can vibrate or rotate.

It is easy to show that the rotational energy is $E_r = BJ(J + 1)$ where $J = 0, 1, 2...$ and B is the rotational constant, and in the absence of an external field, the eigenstates are $2J + 1$-fold degenerate. Analytic but approximate solutions for $|v\rangle$ can then found by making a parabolic approximation around the bottom of the potential R_0, giving eigenvalues $E_v = \hbar\omega_v(v + 1/2)$ where $v = 0, 1, 2...$. ω_v has the usual form $(k_n/\mu)^{1/2}$, where k_n equals $d^2E_n/dR^2|_{R=R_0}$, the curvature at the bottom of the potential.

To summarize, a state of the molecule $|\Psi\rangle$ is given by

$$|\Psi\rangle = |n\rangle |v\rangle |J, m_J\rangle, \tag{2.29}$$

where n is the electronic, v is the vibrational and J is the rotational quantum numbers. m_J is the projection of the rotational angular momentum on the internuclear axis. Although so far omitted from the discussion, Λ is the projection of the total orbital angular momentum onto the internuclear axis. For LiH, Λ equals 0 in both the X and A states. The total spin is also zero (the S=1 states are unbound). The total electronic angular momentum is therefore zero. These are therefore $^1\Sigma^+$ states which have no fine structure.

As seen in figure 2.11, the anharmonicity of the electronic potential grows for the higher lying states. The parabolic approximation used for the bottom of the potential is no longer accurate. Instead, the full anharmonic potential can be described using a power series

$$U = a_0\xi^2\left(1 + a_1\xi + a_2\xi^2 + ...\right), \tag{2.30}$$

where $\xi = (R - R_0)/R_0$. The resulting energy levels follow the expression

$$E\left(v, J\right) = \sum_{lj} Y_{lj}\left(v + \frac{1}{2}\right)^l \left[J\left(J+1\right)\right]^j. \tag{2.31}$$

The coefficients Y_{lj} are known as the Dunham coefficients. Provided these coefficients for a particular electronic potential $E_n(R)$ are known, the rotational and vibrational states can be calculated. The Dunham coefficients we used to calculate the X-A transitions in ^{7}Li^{1}H are listed in table 2.3. The X (ground) state and A (first excited) state coefficients were taken from references [120] and [121] respectively. The values of $E(v, j)$ calculated for the A state use the bottom of the A-state potential as the reference energy. The energy gap between the bottom of the X and the A state potentials T_e for ^{7}Li^{1}H is 26516.20134cm^{-1} [121]. For readers interested in calculating the energy levels for the ^{6}Li^{1}H isotope, the mass-dependent correction factors needed are also given in reference [121]. All the masses and reduced masses are found in reference [122].

2.5.3 The X$^1\Sigma^+$ to A$^1\Sigma^+$ transition

Having discussed the energy level structure of the X and A states of LiH, we now turn to transitions which can occur between various states of LiH. As a result of the Born-Oppenheimer approximation, the transition frequency ν can be expressed as a sum of the electronic, vibrational and rotational contributions to the energy, giving

$$\nu = \frac{\left(E_{n'} + E_{v'} + E_{J'}\right) - \left(E_{n''} + E_{v''} + E_{J''}\right)}{h}. \tag{2.32}$$

This can be re-written as

$$\nu = \nu_{n''n'} + \nu_{v''v'} + \nu_{J''J'}, \tag{2.33}$$

where $\nu_{i''i'} = \left(E_{i'} - E_{i''}\right)/h$ for $i = n, v, J$. In Eq.(2.33), $\nu_{n''n'}$ is just the energy gap between the X and the A state T_e (expressed in cm^{-1}). For readers unfamiliar with spectroscopic convention, x' (where x is any quantum number) denotes 'the upper state' of a transition while x'' means 'the lower' one. For LiH, A-X transitions with small v' and v'' lie in the 375nm region of the spectrum.

The rotational energies $E_{J'}$ and $E_{J''}$ are characterized by quantum numbers J' and J'', which both have the restriction $J \geq \Lambda$. In the general case, selection rules for conserving angular momentum are that $\Delta J = 0, \pm1$. When scanning the rotational spectrum of a molecule, we obtain a set of lines (referred to as 'branches') for each of these ΔJ values. A set with ΔJ of $+1$, -1 and 0 are referred to as R, P or Q branches, respectively. For instance, the R(0) line designates the transition between $J'' = 0$ to $J' = 1$. In the special case of a Σ to Σ transition, the selection rules also exclude $\Delta J = 0$. In other words, the Q branch is forbidden for a transition between the X and

Table 2.3: Dunham Coefficients for the ^{7}Li^{1}H, taken from [120] and [121].

Dunham Coefficients for the X$^1\Sigma^+$ state of ^{7}Li^{1}H (all values in cm^{-1})

Y_{lj}	$j = 0$	1	2	3	4	5
$l = 0$	0	7.51373151	-8.5858332 10^{-4}	1.079035 10^{-7}	-1.69331 10^{-11}	2.2296 10^{-19}
1	1405.49805	-0.21639109	1.592615 10^{-5}	-0.7635 10^{-9}	-1.4020 10^{-13}	0
2	-23.167899	0.00202305	-1.0308 10^{-7}	-5.963 10^{-11}	0	0
3	0.170928	-2.3166 10^{-5}	-1.3581 10^{-8}	0	0	0
4	-0.0017168	-2.2579 10^{-6}	0	0	0	0
5	-1.1328 10^{-4}	0	0	0	0	0

Dunham Coefficients for the A$^1\Sigma^+$ state of ^{7}Li^{1}H

Y_{lj}	$j = 0$	1	2	3	4	5
$l = 0$	0	2.80105948	-0.0013154943	5.802684 10^{-7}	7.991012 10^{-10}	-8.0302704 10^{-13}
1	233.729831	0.120380	0.0005691534	-5.947009 10^{-7}	-2.298233 10^{-10}	2.322702 10^{-13}
2	30.058843	-0.06641632	-0.00017490204	2.294224 10^{-7}	1.584424 10^{-11}	1.6115146 10^{-14}
3	-4.9507034	0.022951896	3.053481 10^{-5}	-4.338219 10^{-8}	0	0
4	0.7811279	-0.005051864	-3.0429935 10^{-6}	4.424877 10^{-9}	0	0
5	-0.09351255	0.0006860389	1.611465 10^{-7}	-2.351552 10^{-10}	0	0
6	0.007242689	-5.608104 10^{-5}	-3.51020 10^{-9}	5.080346 10^{-12}	0	0
7	-0.0003202396	2.532087 10^{-6}	0	0	0	0
8	6.113479 10^{-6}	-4.853228 10^{-8}	0	0	0	0

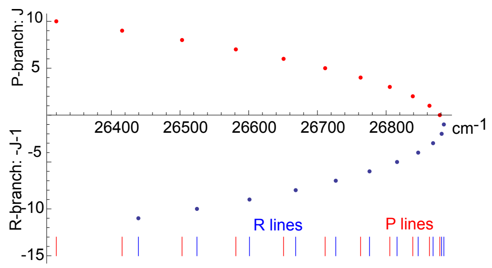

Figure 2.13: Fortrat diagram for the $X^1\Sigma^+(v''=0)$ to $A^1\Sigma^+(v'=3)$ transition. The R/P-branch is shown in blue/red.

Table 2.4: Transition frequencies for $A^1\Sigma^+(v'=0-5)$-$X^1\Sigma^+(v''=0)$ R(0), R(1) and P(1) lines.

v'	R(0) (cm^{-1})	R(1) (cm^{-1})	P(1) (cm^{-1})
0	25948.720	25945.266	25928.221
1	26229.837	26226.559	26209.254
2	26542.827	26539.611	26522.215
3	26878.544	26875.347	26857.923
4	27231.330	27228.124	27210.715
5	27597.126	27593.883	27576.529

A states of LiH. The equation for the rotational transitions for LiH's P-branch can be obtained by rearranging Eq.(2.33) and substituting for $J'+1=J''=J$. This is given by

$$h\nu^p = h\nu_{sv} + B'J(J-1) - B''J(J+1), \tag{2.34}$$

where $B=\hbar/2I$ as before and $h\nu_{sv}$ represents the electronic and vibrational contributions to the energy. Similarly, as $J'-1=J''=J$ for the R-branch, this is given by

$$h\nu^r = h\nu_{sv} + B'(J+1)(J+2) - B''J(J+1). \tag{2.35}$$

It is apparent from Eq.(2.34) and Eq.(2.35) that the rotational structure of electronic bands are quadratic in J. Plots of J versus transition frequency are called Fortrat diagrams. The Fortrat diagram for the $X^1\Sigma^+(v''=0)$ to $A^1\Sigma^+(v''=3)$ transition is shown in figure 2.13. Since B'' and B' for ^{7}LiH are not the same ($\sim$ 222GHz and $\sim$ 85GHz respectively), the transition frequency shows a parabolic dependence on J.

A parabola like the one shown in fig 2.13 is obtained for each set of transitions which involves a change in electronic and vibrational state. As a reference, the R(0), R(1) and P(1) lines for the $A^1\Sigma^+$-$X^1\Sigma^+(v''=0-5)$ transitions are quoted in table 2.4, as these lines are the most often probed in the experiment.

We now turn to calculating the amplitudes for electric dipole transitions. The quantity of interest is the projection of the dipole operator $\hat{\mathbf{D}}$ onto the electric field axis $\hat{E}$, operating between the two states of interest. This gives the coupling of the molecule to an electric field mode in lab-fixed space. The transition amplitude for electric-dipole allowed emission or absorption of radiation between states a and b is thus proportional to

$$\mathbf{D}_{ab} = \langle \Psi_b | \hat{\mathbf{D}} | \Psi_a \rangle. \tag{2.36}$$

$\hat{\mathbf{D}}$ is given by

$$\hat{\mathbf{D}} = e \left(\sum_i Z_i \mathbf{R}_i - \sum_j \mathbf{r}_j \right), \tag{2.37}$$

where the first sum is over the positions and charges of the nuclei and the second sum is over the positions of the electrons. e is the electron charge. The Franck-Condon principle is a means of solving Eq.(2.36). This principle is related to the Born adiabatic approximation where electronic time-scales are assumed to be much faster than nuclear ones. An electronic transition will therefore occur at a constant internuclear separation, as the nuclei will not have had enough time to move significantly over the time-scale of the transition. Probabilities for transitions between various vibrational states can therefore be extracted from the overlap in their wavefunctions. Details of the calculation can be found in the literature, e.g. [117, 118]. The final result is that the transition amplitude is proportional to the overlap integral of the vibrational wavefunctions $\langle v' | v'' \rangle$:

$$\mathbf{D}_{ab} = \ \mathbf{D}_{el}(R) \ \langle v' | v'' \rangle \ \langle J', m'_J | \ Y_{l,m}(\theta, \phi) \ | J'', m''_J \rangle, \tag{2.38}$$

where $\mathbf{D}_{el}(R)$ is given by

$$\mathbf{D}_{el}(R) = -e \int \Phi^*_{n'} \left(\sum_i \mathbf{r}_i \right) \Phi_{n''} d\mathbf{r}_i. \tag{2.39}$$

The final factor, involving the rotational states and a spherical harmonic $Y_{l,m}(\theta, \phi)$, gives rise to the selection rules discussed above. Although not detailed here, this rotational term leads to three-J symbols. These are well known factors, allowing the full transition amplitude from state a to b to be calculated. For this section, coefficients from rotational states will simply be quoted when required.

In reference [123], the squares of the dipole matrix elements $\mathbf{D}^2_{ab}$ are available along with the spontaneous photon emission intensities $I(v', v'')$. These intensities are given by

$$I(v', v'') \propto \left| \langle \Psi_b | \hat{\mathbf{D}} | \Psi_a \rangle \right|^2 \nu^3, \tag{2.40}$$

where ν is the transition frequency as defined in Eq.(2.32). Knowing the frequencies and intensities of the transitions, emission spectra of ^{7}LiH from a particular $\mathrm{A}^1\Sigma^+(v')$ state can be calculated. Note that the rotational factor was ignored in reference [123]. Figure 2.14 shows the normalized calculated emission spectrum expected from the lowest 6 vibrational states in the $\mathrm{A}^1\Sigma^+$ band. The transition down to the $v'' = 0$ states are highlighted in blue.

2.5.4 The laser excitation

The behaviour of the LiH signal as a function of probe laser intensity is helpful in characterizing the detector as well as the molecular beam itself. Figure 2.16 shows the LiH signal obtained at

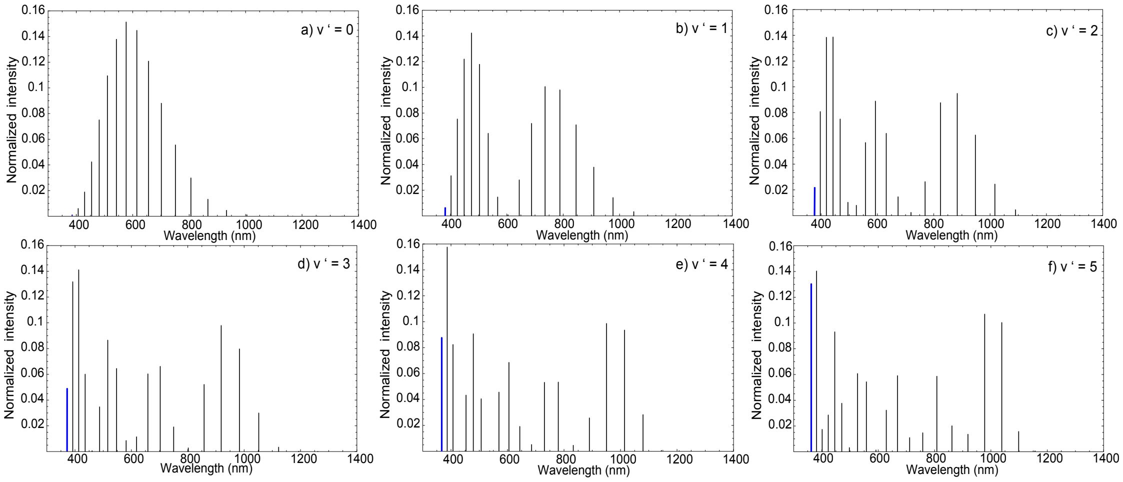

Figure 2.14: Calculated emission spectra for different vibrational states in the $\mathrm{A}^1\Sigma^+$-$\mathrm{X}^1\Sigma^+$ band. The transition down to the $v'' = 0$ state is highlighted in blue. (a) $v' = 0$, (b) $v' = 1$, (c) $v' = 2$, (d) $v' = 3$, (e) $v' = 4$, (f) $v' = 5$

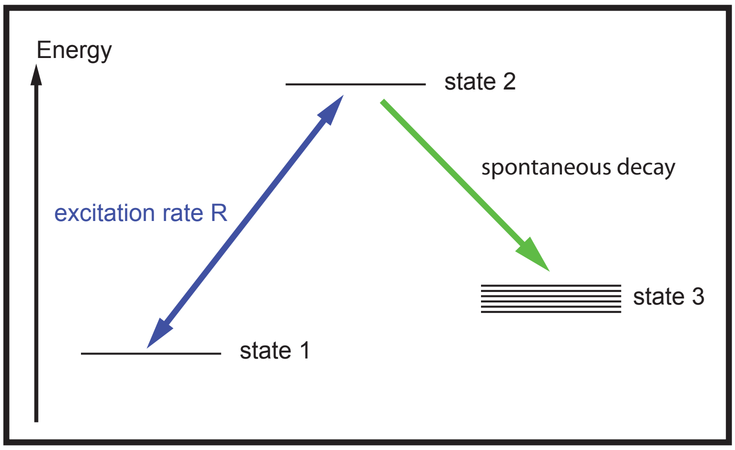

Figure 2.15: Energy level diagram showing the states accounted for by the model.

different probe intensities for the ($v'' = 0$) to ($v' = 4$) $R(1)$ line. At low laser intensities, the signal observed is proportional to the laser intensity. However, the signal then deviates toward saturation. In order to understand this behaviour, a model following reference [114] is constructed. This model solves rate equations obtained from treating the molecule as a 3-level system. The first level is the initial state, before the probe laser excitation. The second is the excited state, while all other states to which the molecule can decay to are collectively labelled 'level 3'. Figure 2.15 shows the energy level diagram of the model.

By taking the Bloch equations in the limit where the coherences have reached a steady state, one finds that the laser excitation rate R from state 1 to state 2, which is equal to the stimulated emission rate, is given by:

$$R = \frac{\Gamma/2}{(1 + 4\delta^2/\Gamma^2)} \frac{I}{I_{sat}} \tag{2.41}$$

where Γ is the spontaneous decay rate of level 2, $\delta = \omega_L - \omega_{12}$ is the detuning of the laser from the resonance angular frequency, I is the laser intensity and $I_{sat} = \epsilon_0 c\hbar^2(\Gamma/2)^2/D^2$ is the usual

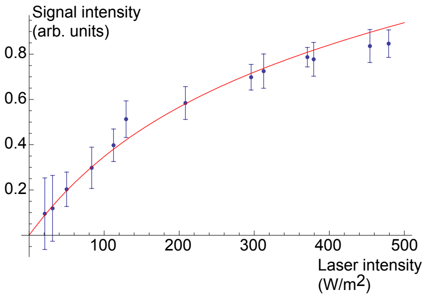

Figure 2.16: LiH signal obtained at various laser intensities for the $(v''=0)$ to $(v'=4)$ $R(1)$ transition. The red curve shows the expected behaviour as calculated using the 3 state model.

'saturation intensity' familiar to atomic cases, where D is the matrix element of the dipole operator connecting levels 1 and 2, covered in the previous section. It should be noted that the molecular signal does not saturate at the 'saturation intensity' I_{sat}. This becomes obvious by remembering that the quantity I_{sat} is defined as the intensity for which the excitation rate matches the decay rate in a closed transition. In our experiment where the transition is anything but closed, the intensity which extracts the maximum signal from the molecules is the intensity required to pump all molecules into the dark state (state 3). This also means that the maximum number of photons to be expected from a LiH molecule is just over 1 (if the branching ratio r equals 0, then it would be exactly 1). If we make r be the branching ratio between emissions to level 1 and 3, the molecule can either decay from level 2 back to level 1 at a rate of $r\Gamma$, or decay to level 3 at a rate of $(1-r)\Gamma$. We ignore any decay or excitation out of level 3. It is thus possible to write down the rate equations for each state. For state 1, we obtain

$$\frac{dN_1}{dt} = -RN_1 + r\Gamma N_2 + RN_2, \tag{2.42}$$

while for state 2, we get

$$\frac{dN_2}{dt} = RN_1 - RN_2 - r\Gamma N_2 - (1-r)\Gamma N_2. \tag{2.43}$$

The last two terms in Eq.(2.43) are only separated to indicate that one of them represents the spontaneous decay to state 1, while the other is the decay to state 3. Finally, for state 3, we obtain

$$\frac{dN_3}{dt} = (1-r)\Gamma N_2. \tag{2.44}$$

Solving for these equations give expressions for $N_1(t)$, $N_2(t)$ and $N_3(t)$. The integral of $\Gamma N_2(t)$ (the sum over the last two terms in Eq.(2.43)) over the laser interaction time τ then gives the number of fluorescent photons emitted per molecule n_p:

$$n_p = \int_{t=0}^{\tau} \Gamma N_2(t) = \frac{R\Gamma}{R_+ - R_-}\left(\frac{e^{-R_+\tau}-1}{R_+} - \frac{e^{-R_-\tau}-1}{R_-}\right). \tag{2.45}$$

$R_\pm$ are given by

$$R_\pm = R + \frac{\Gamma}{2} \pm \sqrt{R^2 + rR\Gamma + \Gamma^2/4}. \tag{2.46}$$

Table 2.5: Various numbers used for calculating the LiH signal vs probe laser intensity curve. *used for calculating the detuning. **used for calculating intensity

D^2	$2/9 \times 1.910 \times 10^{-2}$ $(e\ \text{Å})^2$ [123]
Γ	$31.7 \times 10^6 s^{-1}$ [124]
r	0.057 [123]
τ	5×10^{-6} s
Doppler width*	60MHz
width of laser beam**	3mm
height of laser beam**	8mm

The relevant parameters for determining n_p in this experiment are given in table 2.5. The factor of 2/9 in the value for D^2 is to account for the angular part of Eq.(2.38). Γ is the inverse of the excited state lifetime. r is the Franck-Condon factor. τ is based on a 600m/s beam and a laser width of 3mm along the molecular beam axis, giving an interaction time of 5μs. Intensities are calculated by assuming a 'top hat' beam profile 3mm × 8mm. 1mW is therefore approximately 42W/m^2. Finally, the Doppler width must be accounted for when calculating n_p. Because of the velocity spread of the molecules, there is a Doppler shift in the perceived laser frequency. The result is that for a molecule travelling off axis, the excitation rate is lower than for a molecule travelling along the beam axis. To account for this, we integrate the product of n_p with a Gaussian distribution $G(\delta)$ of width δ_0, giving

$$\bar{n}_p = \frac{\int_{-\infty}^{\infty} n_p(\delta)\, G(\delta)\, d\delta}{\int_{-\infty}^{\infty} G(\delta)\, d\delta}. \tag{2.47}$$

To our best estimates from scanning the laser frequency, the Doppler width of our molecular beam was found to be around 60MHz. The result of applying this model is shown in figure 2.16, where good agreement is obtained. When taking this data, the major difficulty was the random fluctuations in molecular beam intensity over the period of measurement. In order to minimize this effect, the signal was measured at 13.7mW before and after every data point. The data was then normalized against the average of the two signals measured at 13.7mW. The results of the model were also normalized to the value at that power. Therefore, '1' in figure 2.16 does not mean saturation. At 13.7mW (a typical amount of power available for the $v'' = 0$ - $v' = 4$ transition) n_p is found to be around 0.26. The laser intensity required to saturate this transition (90% of molecules are pumped to the dark state before they leave the laser) was found to be 8750W/m^2. In a later section, the model will be used to estimate the power needed to saturate various v' transitions in order to determine the transition with the highest detection efficiency.

2.6 The detector's hardware

The detection assembly is mounted in the second DN200CF 6-way cross (see figure 2.17), which is also pumped out by a 1000l/s turbomolecular pump. The molecules cross the probe laser beam at the centre of the chamber. The typical operating pressure is 2×10^{-7}mbar.

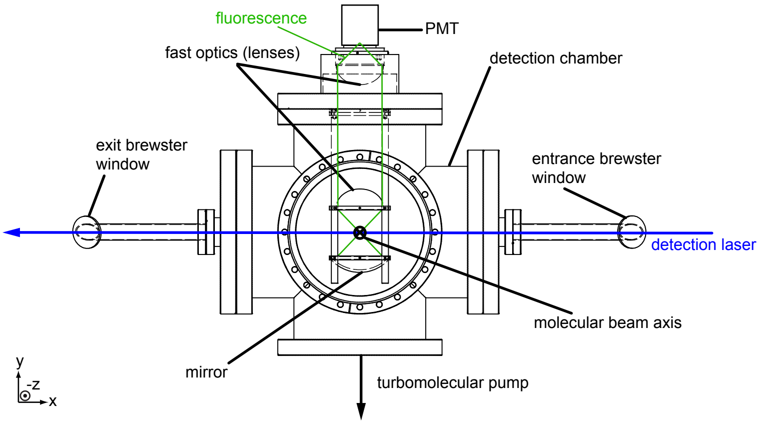

Figure 2.17: Experimental layout for detection chamber, looking down the beam axis.

LIF detection is a two step process. Its success depends on the efficiency with which the molecules can be driven to an excited state, and on the efficiency with which the fluorescence from the molecules can be collected and detected. As the fluorescence comes from spontaneous emission, it is emitted over a large solid angle. It is therefore important for the detector to be able to match the wide solid angle around the detection region at the centre of the chamber. Our detection optics consisting of a spherical mirror (Melles Griot 01MCG023) of diameter 90mm and focal length 30mm and two condenser lenses (Comar 55AF73) of diameter 73mm and focal length 55mm allow a 1:1 image of the gas pulse to be recreated on the photocathode of the photomultiplier tube (a Hamamatsu R928P) while subtending a solid angle of 1.27 steradians (see figure 2.17). The PMT signal can be sent to an ADC/discriminator, which sends out a TTL pulse for each observed photon (photon counting mode). Alternatively, if there is sufficient signal coming from the PMT to produce a continuous current, this is converted to a voltage and amplified (current mode). The signal is then sent to the PCI-6251 data acquisition board (DAQ). In either data acquisition mode, the DAQ measures the signal at a rate of 1MHz. As seen in figure 2.14, most of the fluorescence is emitted at wavelengths which are significantly longer than the probe laser. By placing a glass filter (Schott GG395) in front of the PMT, we can reduce the background laser scatter. However, the downside is that fluorescence at short wavelengths is also filtered. The laser polarization is linear, and parallel to the molecular beam axis. Experimentally, rotating the linear polarization of the probe light by 90° did not produce any measurable change in molecular signal.

2.7 Results for the detector

2.7.1 The rotational and vibrational temperatures

The raw time-of flight data has already been shown in section 2.4.2. If the probe laser's frequency is scanned over a resonance, a series of TOF profiles is obtained. Each TOF corresponds to a specific probe frequency. By integrating over the flight time of the pulse, we obtain the total number of photons recorded at each frequency. Figure 2.18 (a) shows a laser-induced fluorescence signal from ^{7}LiH while scanning over the $A^1\Sigma^+$(v"=3) - $X^1\Sigma^+$(v"=0) R(0) resonance at 801798.1GHz. Fitting a Gaussian profile, shown in red, shows a peak amplitude of approximately 55 photons per shot with a width of around 80MHz. This is consistent with predictions based on the transverse velocity distributions of the molecules. The calculated frequency given in table 2.4 is 26878.544cm^{-1} or 801798.5GHz. The uncertainty in our wavemeter (a HighFinesse WS-6) is 600MHz, so the observed frequency is in very good agreement with the calculated value.

For ^{7}LiH, we also observe similar resonances for the ($v' = 2$) and ($v' = 4$) transitions at 795734.0GHz and 816375.0GHz. Figure 2.18(b) shows the same transition for ^{6}LiH, the other stable isotope of lithium. Once the laser intensity difference for the two frequencies are accounted for, the amplitude ratio between ^{6}LiH to ^{7}LiH is found to be $7.7 \pm 0.5\%$ which is consistent with the natural abundances in lithium, which is $7.5\%/92.5\% = 8.1\%$.

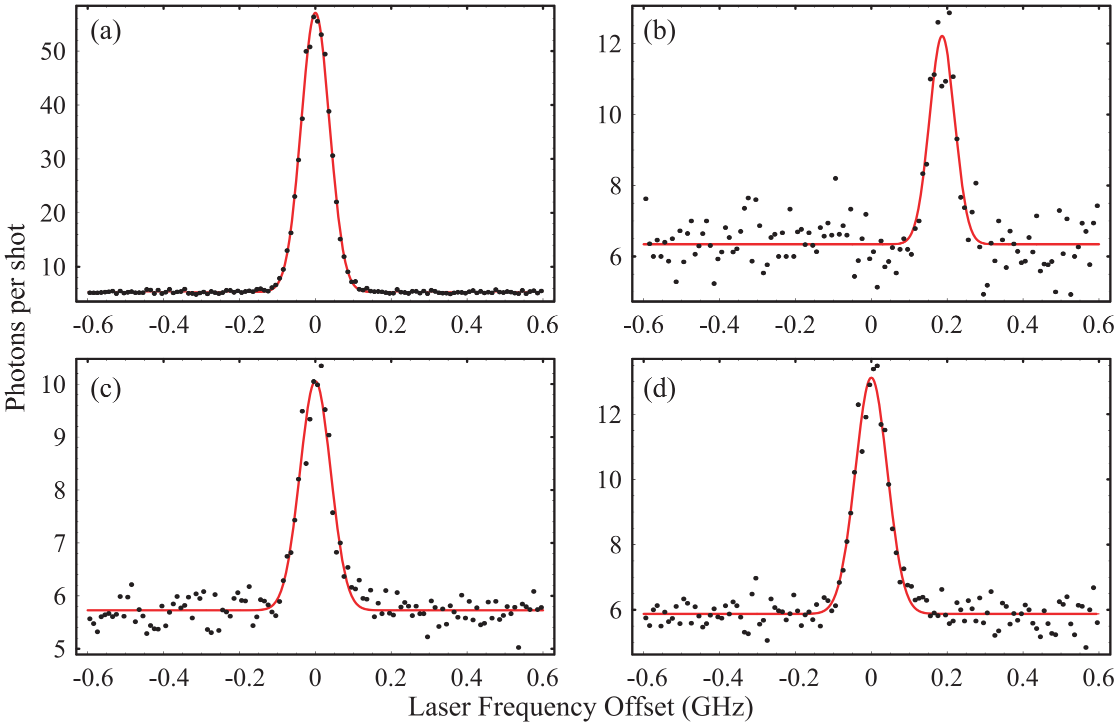

Figure 2.18: Probe laser scanned over several LiH resonances. (a) ^{7}LiH $X^1\Sigma^+(v'' = 0)$ - $A^1\Sigma^+(v' = 3)$ $R(0)$, (b) ^{6}LiH $X^1\Sigma^+(v'' = 0)$ - $A^1\Sigma^+(v' = 3)$ $R(0)$, (c) ^{7}LiH $X^1\Sigma^+(v'' = 0)$ - $A^1\Sigma^+(v' = 3)$ $R(1)$ and (d) $X^1\Sigma^+(v'' = 1)$ - $A^1\Sigma^+(v' = 6)$ $R(0)$.

The rotational temperature can be estimated from figure 2.18 (c), which shows the ($v'' = 0$) to ($v' = 3$) R(1) line. The sum of the squared matrix elements for the R(1) line is twice that of the R(0) line. Taking this and the change in laser intensity into account, we find the population ratio between ground and first rotationally excited state to be $N(J = 1)/N(J = 0) = 8.2 \pm 2.5\%$. If we assume all rotational states are in thermal equilibrium with each other, this implies a rotational temperature of $T_{rot} = 5.9 \pm 0.5K$. This is significantly hotter than the translational temperature, found in section 2.4.2 to be $0.99K$. A search for an R(2) resonance at 805336GHz did not yield any signal. This put an upper bound on the population ratio $N(J = 2)/N(J = 0) < 4\%$, which is consistent with the estimate from the R(1) line. Figure 2.19 shows the velocities and temperatures of molecules in the $J = 0$ and 1 states, extracted from probing the R(0) and R(1) lines. The

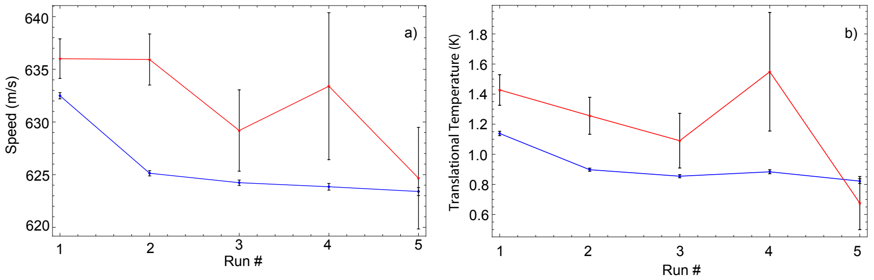

Figure 2.19: Molecular pulse a) velocities and b) temperatures extracted from the time of flight profiles when probing the R(0) (in blue) and R(1) (in red) lines. The data was taken by alternating between the transitions. Each run corresponds to an R(0)-R(1) pair of data sets.

blue points show the R(0) data, while the R(1) data is shown in red. This data was taken by alternating between the two transitions. Each run therefore corresponds to an R(0)-R(1) pair of data sets. A systematic difference in velocity is clearly observable. On average, the rotationally excited molecules are travelling 5.9±1.3m/s faster than ground state molecules, with a translational temperature which is also hotter than the $J = 0$ molecules by $0.25 \pm 0.07K$. This indicates that the rotational states have not completely reached thermal equilibrium with the carrier gas.

Turning to the vibrational states, comparing the $X^1\Sigma^+(v'' = 1)$-$A^1\Sigma^+(v' = 6)$ R(0) frequency scan (figure 2.18(d)) to the $X^1\Sigma^+(v'' = 0)$- $A^1\Sigma^+(v' = 3)$ R(0) scan (figure 2.18 a)) also gives an amplitude ratio. In order to calculate the temperature, we need to correct the measured amplitudes by accounting for differences in laser intensities and Frank-Condon factors. The corrected amplitude ratio is given by

$$\frac{N(v''=1)}{N(v''=0)} = \frac{N(v''=1)_{obs}}{N(v''=0)_{obs}} \frac{P_{v''=0}}{P_{v''=1}} \frac{FC_{v''=0}}{FC_{v''=1}}, \tag{2.48}$$

where N_{obs} are the observed amplitudes, $P_{v''=i}$ are the laser intensities available for the transition and $FC_{v''=i}$ are the Franck-Condon factors. We thus find that $N(v'' = 1)/N(v'' = 0) = 1.5 \pm 0.2\%$. If we assume all vibrational states are in thermal equilibrium amongst each other, they will follow a Boltzmann distribution. T is then given by

$$T = \frac{-h\ c\ v_{10}}{k_b\ ln\left[N(v''=1)/N(v''=0)\right]}, \tag{2.49}$$

where v_{10} is the vibrational splitting in m^{-1}. This gives a temperature of $T_{vib} = 468 \pm 17K$. This rather high temperature also comes from the vibrational states not reaching equilibrium with the other degrees of freedom. We then searched for a signal from molecules in higher lying vibrational states by scanning 4GHz around 804948GHz, the expected frequency for the $X^1\Sigma^+(v'' = 2)$ to $A^1\Sigma^+(v' = 10)$ $R(0)$ transition. We did not see any signal, which constrained the amplitude ratio to $N(v'' = 2)/N(v'' = 0) < 1\%$. This is consistent with the vibrational temperature estimated using the $(v'' = 1)$ state, but does not constrain that value any further.

This data shows that although the LiH beam does depart somewhat from the ideal expansion case, we nonetheless end up with a cold beam of LiH where approximately 90% of the molecules are in their absolute ground state.

2.7.2 Temporal resolution of the detector

The temporal resolution of our detector depends on the probe laser intensity, the laser's spatial profile along the molecular beam axis and the velocity of the molecules. Figure 2.20 shows the time needed to optically pump out of level 1 as a function of laser power. This was calculated using the model presented in section 2.5.4. The times shown on the graph are the times needed for 90% of the molecules to be pumped out of state 1. On the same graph, the maximum interaction time for a 420m/s and a 53m/s beam and a laser width of 3mm are shown.

In the low power limit (when some molecules exit the detector without having been excited), the detection is spread out over the entire laser profile. The resolution is then simply given by $d_{laser}/v_{molecules}$ where d_{laser} is the spatial width of the laser and $v_{molecules}$ is the velocity of the molecules. Increasing the laser intensity then decreases the time it takes to pump all the molecules into a dark state. Having pumped all the molecules away, any 'left over' laser width no longer affects the signal. In the high intensity limit, this extinction time therefore becomes the relevant time-scale.

Decelerating the molecules along the molecular beam axis (z) increases the interaction time between the laser and the molecule. This affects the temporal resolution of the detector. As an example, the interaction times at 8mW of laser power for different molecule velocities are shown as vertical lines in figure 2.20. At 420m/s, the duration of the fluorescence pulse is determined by the spatial width of the laser. At 53m/s, the interaction time has increased significantly. The duration of the fluorescence is now given by the time it takes to pump the molecules to the dark state. This increases the uncertainty from 7μs to about 32μs. Note that decreasing the molecular velocity does increase the signal amplitude because more molecules are pumped to the dark state.

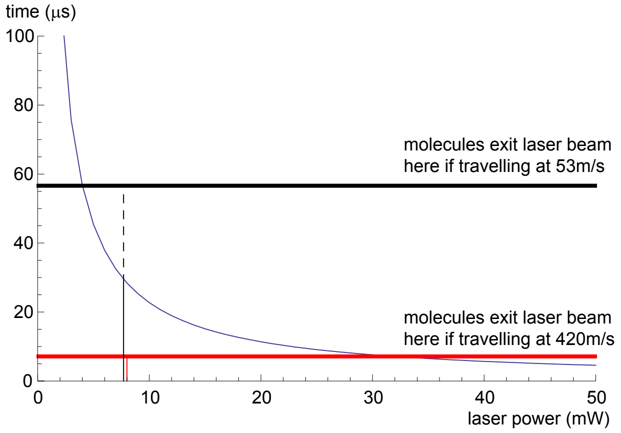

Figure 2.20: Decay time of ground state population as a function of laser power (in mW). At high power, this defines the resolution for our detector. Also shown are, the laser interaction times for a laser width of 3mm and beam velocity of 420m/s (red) and 53m/s (black).

Other smaller factors include the PMT response time (the time it takes to convert a photon to a current pulse) which is of order of 10ns, the discriminator bandwidth which is just over 1MHz, the DAQ sampling rate which is also 1MHz and the upper state lifetime which is around 30ns.

2.7.3 Troubleshooting: detecting Fe in the beam

This may be of interest to anyone attempting to build a molecular beam, as fluorescence from iron is a good test for both the source and the detector. One reason for this is that iron has a large number of transitions reaching across the spectrum. In our case, the Fe I ground state (a^5D) to z^5F^0 state transition at 805677.0GHz was found to be the most convenient. Furthermore, stainless steel is often available for ablation in most machines. In our case, the Li target holder can be ablated simply by adjusting the YAG beam path. Iron was the first signal to be observed in our machine. It was only after using an Fe signal to verify that the source and detector worked correctly that we were able to observe a LiH signal. Figure 2.21 shows a frequency scan around the resonance, while figure 2.22 shows the time-of-flights obtained at different YAG energies. These energies were not measured accurately. Nonetheless, I estimate the energy to be approximately 50mJ (green), 100mJ (blue) and 300mJ (red).

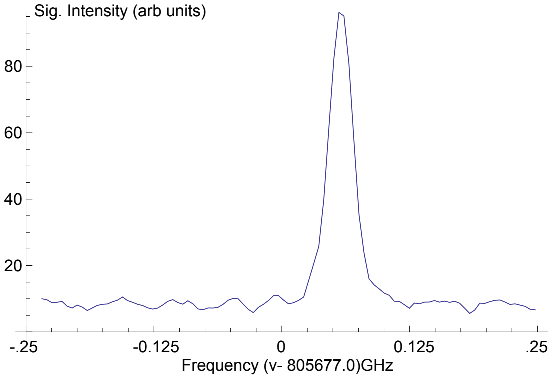

Figure 2.21: 500MHz scan around 805677.0GHz showing fluorescence from iron.

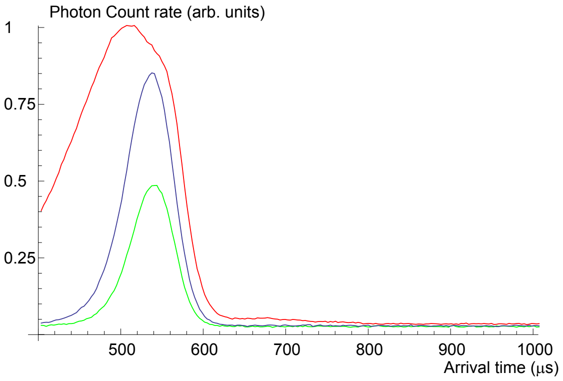

Figure 2.22: TOFs showing signals from iron for different ablation energies.

2.8 The LiH detection efficiency

The overall detection efficiency depends on the choice of transition. In this section, the upper vibrational state (v') which maximizes detection efficiency is determined. Although the emission spectra from the various upper states are all broad (see figure 2.14), there is an overall blue-shift as the vibrational quantum number is increased. This means that the amount of signal lost to

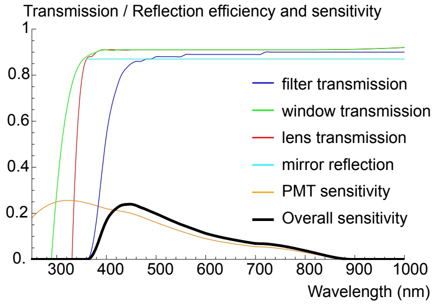

Figure 2.23: Transmission efficiency for window, T_w, lens, T_l, and filter, T_f, together with reflectivity of mirror , R, and PMT quantum efficiency, χ, plotted against wavelength. Overall sensitivity vs wavelength (using Eq.(2.50) also shown in black

the filter increases with higher v'. Furthermore, the PMT quantum efficiency is also a function of wavelength, thus affecting the signal. Another critical criterion is how efficiently the particular probe transition can be driven, as was discussed in section 2.5.4. The laser power available for the various wavelengths must also be considered.

If we assume the detection efficiency is constant across the interaction region, we can calculate the detector sensitivity ϵ for our setup using the following expression:

$$\epsilon = \frac{\Omega}{4\pi} \sum_i q_i (1 + R(\lambda_i)) T_l(\lambda_i)^2 T_w(\lambda_i) T_f(\lambda_i) \chi(\lambda_i) \tag{2.50}$$

where q_i is the fraction of fluorescent photons in the emission line whose wavelength is λ_i, and Ω is the solid angle subtended by the detection optics. R, T_l, T_w, T_f and χ are the mirror reflectivity, lens transmission, window transmission, filter transmission and PMT quantum efficiency, which are all functions of wavelength. To determine the most efficient transition to probe on, ϵ was computed for 5 vibrational states from $v' = 1$ to $v' = 5$. Figure 2.23 shows T_f, T_w, T_l, R , χ as well as $\epsilon(\lambda)$, the overall sensitivity as functions of wavelength which is given by

$$\epsilon\,(\lambda) = (1 + R(\lambda)) T_l(\lambda)^2 T_w(\lambda) T_f(\lambda) \chi(\lambda). \tag{2.51}$$

The window is made out of BK7, which has a typical cut-off in transmission at around 300nm. The manufacturer specified R to be $\geq 87\%$ between 400nm and 800nm. T_f is designed to deliver a very sharp cut-off in transmission below 395nm, which significantly reduces the laser scatter which arrives at the PMT. Finally, the quantum efficiency of the PMT, χ, is significantly reduced at longer wavelengths, which is the limiting factor at that end of the spectrum. Note that there is some uncertainty in these figures as they were reconstructed from diagrams in manuals, but I believe they are correct to about 5%.

$\epsilon(\lambda)$ and the emission spectra calculated in section 2.5.3 are used to give the overall detector sensitivity ϵ for each transition, following Eq.(2.50). The results are shown in table 2.6.

The next step is to estimate the laser power available. Figure 2.24 shows the measured output power from our Ti:Sapphire laser as a function of frequency. The MBD-200's doubling efficiency is 10%/W. From this, we can work out the expected probe laser power.

Table 2.6: Detector Sensitivity ϵ for various v' transitions

v'	ϵ
0	0.0131
1	0.014
2	0.0129
3	0.0109
4	0.0092
5	0.0080

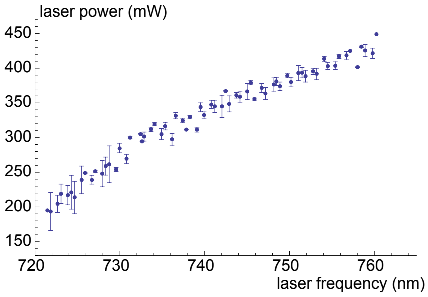

Figure 2.24: Ti:Sapphire output power versus wavelength

Estimates of the laser power available for each transition wavelength, along with the number of photons per molecule n_p emitted by probing the transition (calculated using the 3-state model described in section 2.5.4) is shown in table 2.7.

Table 2.8 shows a summary of the results of the calculation. The total detection efficiency, which is the product of ϵ and n_p is shown in the last column. This number, with units of 'detected photons per molecule' allows the flux of the beam to be calculated. This analysis shows that the most suited transition to probe on is $v'' = 0$ - $v' = 3$. However, one of the main uncertainties associated with the calculation is the laser power. Although the error bars in figure 2.24 are small, this only pertains to the measurement error on the particular day the data was taken. The laser power varies significantly from week to week depending on cleanliness and alignment. Given that

Table 2.7: Laser powers and corresponding values of n_p for R(1) lines of ^{7}LiH.

v'	laser power (mW)	n_p
0	22.77	0.019
1	19.67	0.086
2	16.29	0.174
3	12.76	0.239
4	9.14	0.265
5	5.49	0.243

Table 2.8: Efficiency of our detector for $v' = 0$-5. *Convert to intensity by assuming a top hat profile of 3mm by 8mm.

v'	transition frequency (cm^{-1})	available laser power (mW)*	saturation intensity (W/m^2)	ϵ	n_p	total detection efficiency
0	25948.72	22.77	$1.2\ 10^6$	0.0131	0.019	$2.5\ 10^{-4}$
1	26229.837	19.67	$2.0\ 10^5$	0.014	0.086	0.0012
2	26542.827	16.29	$6.5\ 10^4$	0.0129	0.174	0.0022
3	26878.544	12.76	$2.5\ 10^4$	0.0109	0.239	0.0026
4	27231.33	9.14	$2.5\ 10^4$	0.0092	0.265	0.0024
5	27597.126	5.49	$8.5\ 10^3$	0.0080	0.243	0.0019

ϵ is actually larger for $v' = 4$, the balance tips in favour of the $v' = 4$ transition when the laser power is high. Almost all of our data has been taken by probing on one of the two transitions. As a reference, the intensities required to saturate these transitions for a molecular beam of Doppler width of 65MHz is also shown in table 2.8.

2.8.1 Flux of molecules

We finally arrive at determining the flux of the molecules. In order to measure the flux as accurately as possible we expanded and collimated the laser beam, then sent it through an aperture of height $H = 4$mm along y and width $W = 3$mm along z. We also inserted a small aperture in the molecular beam around 5cm upstream from the detector. This has the effect of picking out the molecules of lowest transverse velocity, which in turn decreases the Doppler width to about 25MHz. Experimentally, we measured the flux to be 29 photons/shot. n_p is calculated using the model presented in section 2.5.4, and is found to be 0.272. Following section 2.8, ϵ for the $v' = 3$ transition is $\epsilon = 1.09\%$. We obtain a value for the molecular flux to be 4.5×10^7 molecules per steradian per shot when using argon as the carrier gas. The error associated with this is ±35%, which is dominated by the error in the shot to shot fluctuation in signal intensity. In comparison to other molecular beams, this flux is low. For instance, YbF signals observed in other experiments in our lab are typically 100 times larger. We attribute this to the unfavorable energetics described in the first paragraph of this chapter.

2.9 Things we tried to optimize the LiH flux

In this section, I will present several alterations to the laser ablation method as well as alternative methods for making LiH which we tried out.

2.9.1 Electric discharge at nozzle exit

An electric discharge is commonly used to make the molecules of interest from seeded precursors. In the hope of dissociating the H_2 to make the LiH reaction barrierless, we designed a lithium target holder which incorporated a pair of tungsten electrodes (see figure 2.25). The electrodes were placed directly above the Li pot, placed approximately 2mm away from the valve face. The electrode spacing could be adjusted, but was set to approximately 1.5mm. The pot was designed to be bolted in on the side, such that it could be removed for maintenance without having to adjust the electrodes. The larger pot at the bottom of the unit acts as a tray to prevent material from reaching the turbomolecular pump Although this was not a concern for Li, it may be crucial if other ablation targets are used. This allowed us to easily switch between laser ablation and electric discharge, or to run both simultaneously. In order to prevent any surface discharges along the target holder, the entire unit (with the exception of the removable Li pot) was machined out of polyetheretherketone (PEEK).

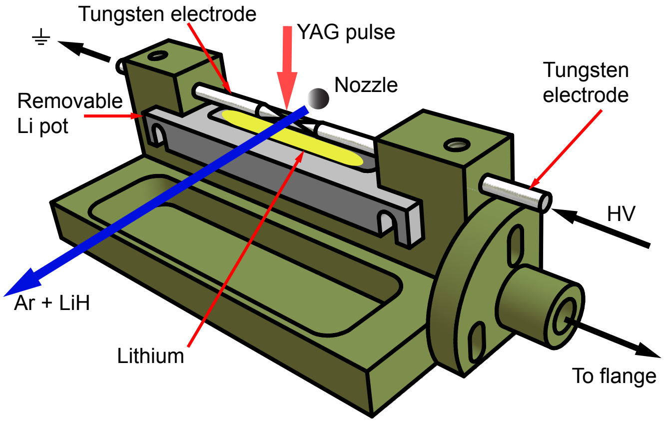

Figure 2.25: A pair of electrodes mounted on the Lithium target holder.

The discharge was triggered by a home-made circuit of transistors attached to a Lukas DLB01 ignition coil. The transistors would cut off the current flowing through the primary coil very quickly, causing a large voltage spike in the secondary one. Although some changes have been made to the design, the circuit was based on the diagram found in reference [125]. This produced a $\approx 200\mu$s long spike of controllable amplitude ranging from -7 to -15kV (depending on the voltage applied across the primary coil). After optimizing the LiH signal using the usual ablation technique, we applied a discharge onto every second shot to observe its effect on the LiH signal. Looking into the source chamber, the entire gas pulse glows when the discharge is applied. Our detector registered a lot of frequency independent light coming from the beam, at very early arrival times ($<100\mu$s). In spite of trying a large range of different discharge trigger times and energies, we only observed that the discharge destroyed the LiH signal. In an attempt to understand what happens to our signal, we changed our detector to probe for lithium atoms. The results are shown in figure 2.26. The blue TOF signal was obtained using the usual mode of operation. The red curve shows the effect of applying a 7kV discharge across the gas pulse $\approx 150\mu$s before the Q-switch is fired.

Analysing the TOF for when the discharge is applied, we observe that the atoms are travelling 23.7m/s faster, with a translational temperature which is also 1.87K hotter than the atoms which

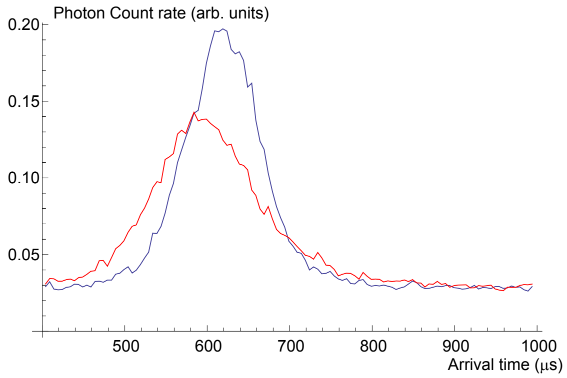

Figure 2.26: TOF signal obtained by ablating the Li target and probing for lithium in the beam. The blue curve shows the signal from a normal ablation. The red curve shows the effect of applying a 7kV discharge across the gas pulse ≈150μs before the ablation.

were not subjected to the discharge. Although this may be related to the disappearance of the LiH signal, we were unable to determine anything specific. We did search for signals from higher-lying rotational states of LiH in case the molecules were being severely heated. We did not observe any LiH signal.

2.9.2 Other precursors: Butyllithium, $LiAlH_4$ and LiH

Butyllithium, an organometallic, is soluble in Hexane which has a significant vapour pressure. It was hoped that this would act as a better precursor to LiH, as it contains both Li and H. We bubbled Argon through this Hexane/Butyllithium mixture, and used it to make a supersonic jet. Unsurprisingly, this jet on its own did not contain any measurable amount of LiH. Ablating the Li target did then yield a LiH signal, but the flux was the same as using H_2. We also applied a discharge to this new mixture, but this only destroyed the signal obtained from the ablation. Electric discharge of the mixture, without the ablation, did not yield any signal either.

We made a brief attempt at ablating other targets. Lithium aluminium hydride is known to decay to LiH when heated. Unfortunately, $LiAlH_4$ is a powder. Our first approach was simply to fill the target pot with the powder, and to proceed to ablate as usual. We found that the powder is simply blasted away within a few hundred shots, covering the inside of the vacuum chamber with a layer of dust. Our second approach was to attach a commercially available pellet of $LiAlH_4$ to the valve. The Nd:YAG also cracked the pellet within a few minutes, in spite of having lowered the laser energy to a minimum. During these few minutes, we did not observe any LiH. Although we had planned to proceed with ablating LiH directly, we did not as it is also a powder.

2.9.3 Using a reaction channel

The literature on molecular beam sources sometimes suggests the use of a reaction channel at the exit of the valve. By injecting the ablated atoms into the channel, the chemistry is driven within a region of higher pressure than the freely expanding jet. The claim is that this leads to higher molecular yields [126]. Figure 2.27 shows our channel design. A 3mm diameter Li wire is attached

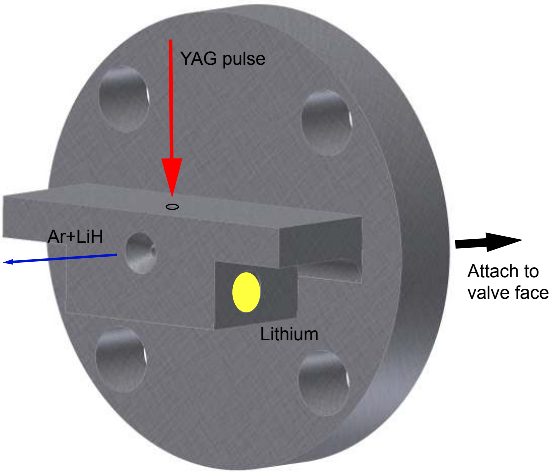

Figure 2.27: Reaction channel design.

to the bottom, while the Nd:YAG laser is shot through the small hole at the top of the channel. The gas pulse flows over the ablated target, confined to the channel and then exits the conical opening.

Experimenting with this reaction channel, we observed intense light pulses at the detector of photon count rates exceeding 1MHz, but these were independent of probe laser frequency. We propose that this is due to metastable states of iron coming from ablating the reaction channel. We were unable to determine whether we observed any LiH with this setup, as the tightly focused YAG beam had drilled through the lithium wire. After a few hours, a downward facing ablation plume (toward the vacuum pump!) was visible. A second attempt was made with a slightly larger hole for the Nd:YAG pulse, only to find that most of the plume was now directed upwards, out of this newly widened YAG entrance hole, instead of along the beam axis. No LiH signal was observed.

2.9.4 Exciting the Li atoms to reduce the reaction barrier

Myers *et al.* reported that exciting the lithium atoms into the 2p state increases the LiH signal in an oven, as it reduces the barrier in the reaction $\mathrm{Li} + \mathrm{H}_2 \rightarrow \mathrm{LiH} + \mathrm{H}$ from 2.05eV down to 0.20eV [127]. In order to reproduce this enhancement in our beam, 88mW from a tapered amplifier laser at 446810GHz (the ^{7}Li $2\mathrm{s}_{1/2}$ - $2\mathrm{p}_{3/2}$ transition frequency) was sent through the interaction region where the ablation plume crosses the carrier gas jet. The frequency of the tapered amplifier laser was scanned over a 10GHz region. When the laser hits the target, it is difficult to observe anything in the source chamber due to the scattered light. However, by moving the beam downstream by approximately 1cm, fluorescence from the Li atoms is visible with the naked eye (with protection goggles for the YAG light!) at the position where the laser crosses the gas jet. Having established that the laser frequency is on resonance, the resultant LiH signal can be compared to the one obtained without the extra laser. The results are shown in figure 2.28. The Ti:Sapphire laser was scanned over the $v' = 4$ resonance while alternating between blocking and unblocking the Li (2s-2p) laser. Scans with the extra laser are shown in blue, while the scans without it are shown

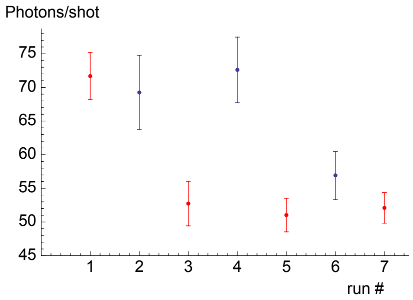

Figure 2.28: Possible enhancement of the LiH signal by exciting the 2s - 2p transition in the Li atoms at the source. Blue/Red points shows the data taken when the enhancement laser was unblocked/blocked.

in red. Although the measurement was limited by fluctuations in the signal amplitude, an upper limit of about 16% on the enhancement can be extracted.

2.9.5 The effect of dual ablation

Recent literature on laser induced breakdown spectroscopy (LIBS) of solid targets reports large increases in signals when a two-pulse ablation scheme is used [128]. These schemes usually involve one of two geometries. The first is a co-linear one where both beams hit the target within a time interval of a few μs. The second, more peculiar, setup involves two orthogonal beams, of which the first hits the target while the other travels along the surface of the target. The underlying mechanisms for this enhancement are the focus of current research in the area. Because we share some experimental features with the LIBS setup, we searched for an enhancement of our LiH signal by using two nearly co-linear Nd:YAG pulses. Two separate Nd:YAG lasers were used for this experiment.

After optimizing the single-pulse signal generated by each YAG separately, we fixed the valve to Q-switch timing for YAG1 while scanning the Q-switch timing of YAG2. Throughout this experiment, we modulated between single shot operation with YAG1 and dual ablation. Figure 2.29 shows the typical results. For this dataset, YAG1 was set to an energy and spot diameter of 42mJ/pulse and 4mm while YAG2 was set to 19.5mJ/pulse and a spot size of 2mm. Figure 2.29(a) shows the signal ratio as a function of time delay scanned with 2μs resolution. Between -10 and +40μs, there is a clear increase in LiH signal. This increase occurs because YAG2 creates a second cloud of molecules in a different part of the gas pulse. As the timing between the YAG pulses approaches zero, the signal returns to the value obtained from the single pulse ablation. This shows that the interaction time of atoms from a single YAG pulse is around 5μs. In this regime, the second plume has very little effect, as the gas pulse is already optimally saturated with Li atoms by the first plume. The asymmetry in Figure 2.29(a) comes about because YAG1 interacts with the early part of the gas pulse, as was discussed for figures 2.10.

Figure 2.29(b) also shows the signal ratio versus Q-switch timing delay plot, but with an increased resolution of 50ns and centred around zero time delay. We find that there is in fact a second dip when the pulses are synchronous to within 250ns. This is because the target and gas

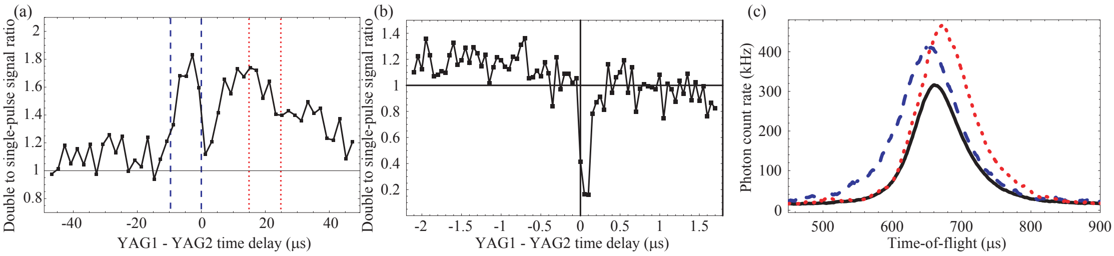

Figure 2.29: The effect of dual ablation on the LiH yield. (a) shows the ratio between single and dual ablation for different time delays between YAG pulses over a range of 100μs. (b) shows the same plot with a resolution of 50ns around zero time delay. (c) shows the time-of-flight profiles for single ablation (solid line), dual ablation with delays of -10 to 0μs (dashed line) and dual ablation with delays between 15 and 25μs.

pulse now effectively only see one YAG pulse of very high energy. And as discussed above for figures 2.9, this implies a local destruction of the gas pulse resulting in signal loss.

The final part, figure 2.29(c) shows the time of flights which we obtain for different Q-switch delay times. We see that when YAG2 fires first the TOF profile is broadened on the early-arrival side, but when YAG2 fires after YAG1, the profile is broadened on the late-arrival side. If the delay between the YAG pulses is set to be greater than 50μs, then we observe two distinct peaks in the TOF. This really shows that the enhancement for our LiH signal comes from filling different parts of the carrier gas pulse.

2.9.6 Long pulse mode

The natural extension to dual ablation is multiple ablation in order to fill the entire carrier gas pulse. YAG1 has a convenient long pulse mode where the energy from one Q-switched pulse can be distributed over a 150μs train of pulses by operating without a Q-switch. This train of 1μs pulses are the laser undergoing relaxation oscillations. In order to obtain a LiH signal, the drop in intensity had to be compensated for by increasing the total energy to 450mJ. The radius of the YAG beam size was decreased from 1.3mm to 300μm. The result is shown in figure 2.30. The LiH signal obtained when running in long pulse mode is shown in red (labelled (a)). The usual LiH signal is shown in blue.

The area under the curves show a 38-fold increase in the number of molecules per pulse. However, the signal decays significantly on the time-scale of tens of seconds. We believe this decay is caused by the drastic changes in surface conditions following the increased energy per pulse and tighter focussing. It is therefore difficult to quantify the enhancement. Nonetheless, a simple model predicts this factor of 38. We postulate that the LiH signal is proportional to the amount of YAG energy deposited on the area of the target which subtends the expanding gas jet (We assume the instantaneous energy never reaches the threshold for gas pulse depletion). This allows us to relate the signal ratio to an expression for the 'useful' energy deposited onto the lithium:

$$\frac{S_{lp}}{S_q} = \frac{\epsilon_{lp}}{\epsilon_q} \times \frac{A_{lp}}{A_q} \tag{2.52}$$

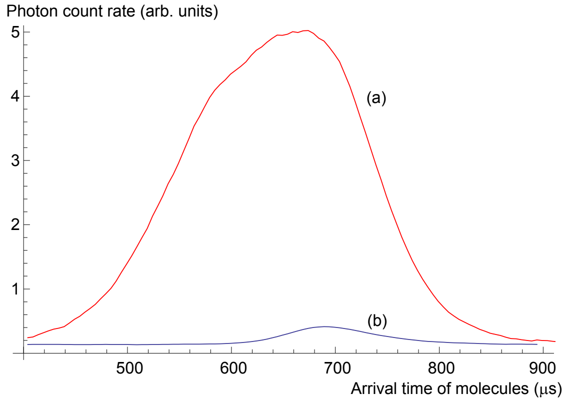

Figure 2.30: TOF profile obtained from running YAG1 in long pulse mode (a), plotted next to a TOF from operating in Q-switched mode (b).

where ϵ_i =(Energy$_i$/spot cross-section$_i$) are the YAG pulse energy densities and the A_i are the overlapping areas between the YAG pulse and the gas jet for the long pulse mode (lp) and the Q-switched mode (q). We then assume the YAG spot size in both modes to be much larger than the expanding jet, giving $A_i = h_{jet} \times 2R_i$ where R_i are simply the radii of the YAG spots. Plugging in the expressions for ϵ_i and A_i reduces equation 2.52 to:

$$\frac{S_{lp}}{S_q} = \frac{E_{lp}\ R_q}{E_q\ R_{lp}} = \frac{450 \times 1.3}{50 \times 0.3} = 39 \tag{2.53}$$

giving a predicted increase in LiH signal by a factor of 39. However, without further investigation, this remains a convenient hypothesis. Although these multiple ablation techniques offered insight into how the source works, they are not particularly useful for Stark deceleration, as the decelerator only accepts molecules arriving in a time window of a few μs. Furthermore, the strong focussing of the YAG pulse, required to obtain a signal using the long pulse mode, destroys the target spot very quickly, leading to very short signal lifetimes. We therefore decided to continue with the project using only a single-ablation pulse.

2.10 Conclusion

We have developed a source of cold LiH molecules for Stark deceleration and trapping experiments. Lithium metal is ablated from a solid target into a supersonically expanding carrier gas. The translational, rotational and vibrational temperatures are 0.9±0.1K, 5.9±0.5K and 468±17K respectively. Although they have not completely reached thermal equilibrium with the carrier gas, we estimate that 90% of the LiH molecules are in the ground state, $X^1\Sigma^+$ (v=0, J=0). The molecules are detected through laser-induced fluorescence using a frequency doubled Ti:Sapphire laser tuned to the $A^1\Sigma^+$-$X^1\Sigma^+$ transitions at around 375nm. The number of molecules in the ground state vibration-rotation is $4.5 \pm 1.8 \times 10^7$ molecules per steradian per shot.

It is difficult to understand the reaction mechanism in our source. Had the reaction been the straightforward $Li + H_2 \rightarrow LiH + H$, I would have imagined that some of these alternative setups would have yielded larger signals. After 2 and a half years of playing with this molecule, my best guess is that LiH (or a very convenient precursor) is pre-formed on the surface of the target. This is then simply ablated off the surface and captured by the gas jet. This would explain the lack of signal with the discharge setup, as well as the signal observed long after H_2 was removed from the gas. Our signal is then limited by the abundance of LiH on the surface as well as the capture efficiency of the gas jet. Nonetheless, this source produced enough LiH molecules to enable us to decelerate them down to trappable velocities, as will be shown in section 4.

Chapter 3

Driving the transition to the rotationally excited state

3.1 Introduction

For the decelerator to work, the molecules need to be in a 'weak-field seeking' state, a state in which the molecule is repelled from regions of high electric field strength. As discussed in chapter 2, most of the molecules we produce are in the strong-field seeking ground state. Before injecting the molecules into the decelerator, we must drive them to the closest weak-field seeking state, the $J = 1$, $m_J = 0$ state. In zero field, the transition is at 444GHz, which falls into the spectral region often referred to as the 'THz gap'. On one hand, this region is beyond the upper limit of frequencies achievable through electronic devices. Yet, the frequencies are too low for any conventional optical sources. The result is that it is unusually difficult to drive excitations at these frequencies. We resorted to using non-linear crystals to frequency quintuple the output of a Gunn oscillator, a solid state device which produces radiation at 88.8GHz.

3.2 Driving a rotational transition

In this section, the amount of power required to drive the $X^1\Sigma^+$(v=0, J=0)-$X^1\Sigma^+$(v=0, J=1) transition is calculated and the expected lineshape is derived.

We begin by evaluating the dipole moment D_{ab} between two rotational states. As discussed in section 2.5.3, $\mathbf{D}_{ab}$ is given by $\langle\Psi_b|\hat{\mathbf{D}}|\Psi_a\rangle$ and is given in Eq.(2.38) as

$$\mathbf{D}_{ab} = \mathbf{D}_{el}(R)\ \langle v'|v''\rangle\ \langle J', m'_J|\ Y_{l,m}(\theta,\phi)\ |J'', m''_J\rangle,$$

where $\mathbf{D}_{el}(R)$ is defined in Eq.(2.39) as

$$\mathbf{D}_{el}(R) = -e\int \Phi^*_{n'}\left(\sum_i \mathbf{r}_i\right)\Phi_{n''}d\mathbf{r}_i,$$

where $i = 1$ to N, the number of electrons in the system. In the rotational transition the electronic and vibrational states do not change, so $n' = n''$ and $\langle v'|v''\rangle = \langle v'|v'\rangle = 1$. The matrix elements along the diagonal of $\mathbf{D}_{el}(R)$ represent the permanent electric dipole moment of the molecule. For the ground state of LiH, this takes the value of 19.6×10^{-30} Cm (Coulomb · metres) or 5.88 Debye at the equilibrium internuclear separation [129]. Note that a purely rotational transition between states in the same electronic and vibrational state would be forbidden if the permanent electric dipole moment were to vanish.

A wealth of literature is available on how to evaluate the rotational factor $\langle J', m'_J | Y_{l,m} (\theta, \phi) | J'', m''_J \rangle$, including chapter 5 of Brown and Carrington's book [117], chapter 3 of Sakurai's [130] as well as Zare's [119] and Edmonds' [131] books. Using the Wigner-Eckart theorem, the term reduces to well known functions called 3-J symbols. For driving the 444GHz transition between the J=0 and J=1 state, the rotational factor is found to be $1/\sqrt{3}$, making the total dipole moment D equal to $(19.6 \times 10^{-30})/\sqrt{3}$.

We can now calculate the power required to drive the transition. For a two level atom in the presence of a driving field $E_0 \exp[i\omega t]$, the Rabi formula expresses the excitation probability for the upper state $|c_2(t)|^2$, and is given by

$$|c_2(t)|^2 = \frac{\Omega^2}{\Omega^2 + (\omega - \omega_{12})^2} \sin^2 \left\{ \frac{1}{2} \left[\Omega^2 + (\omega - \omega_{12})^2 \right]^{1/2} t \right\} \tag{3.1}$$

where ω_{12} is the resonance frequency between states 1 and 2 and Ω is defined as $(D\ E_0)/\hbar$. The sinusoidal factor causes the well known Rabi flopping [130]. The probability of observing the atom in its excited state oscillates in time at the frequency Ω', given by

$$\Omega' = \sqrt{\Omega^2 + (\omega - \omega_{12})^2}. \tag{3.2}$$

$|c_2(t)|^2$ is maximal when the argument of the $\sin^2$ in Eq.(3.1) is equal to $\pi/2$ (or any odd multiple of $\pi/2$ thereafter). The interaction time t is fixed by the transit time of the molecules t_0. For a beam travelling at 600m/s and a microwave beam diameter of 3cm, the interaction time is 50μs. The criteria imposed by Eq.(3.1) for the power required to drive a π pulse (a pulse which inverts the population of the states) is therefore given by $\Omega' t_0 = \pi$ and $(\omega - \omega_{12}) = 0$. Remembering that power P can be expressed in terms of E_0 as

$$\frac{P}{A} = I = \frac{1}{2} c \epsilon_0 \left(E_0 \right)^2 \tag{3.3}$$

where I is the intensity of the light and A is the area covered by the microwave beam, the power required to drive a π pulse is given by

$$P = \frac{\pi}{8} c\ \epsilon_0 \left(\frac{\pi \hbar v_0}{D} \right)^2, \tag{3.4}$$

having used the fact that t_0 equals $2R/v_0$ where R is the radius of the microwave beam. Taking v_0 to be 600m/s and D to be $(19.6 \times 10^{-30})/\sqrt{3}$, Eq.(3.4) works out to be 328nW. Figure 3.1 a) shows the excitation probability as a function of microwave frequency calculated using Eq.(3.1) for 60μW of power, the maximum available from the source.

So far, broadening mechanisms have been ignored. The dominant contribution to broadening is the velocity distribution of the molecules. In particular, any velocity spread along the molecular

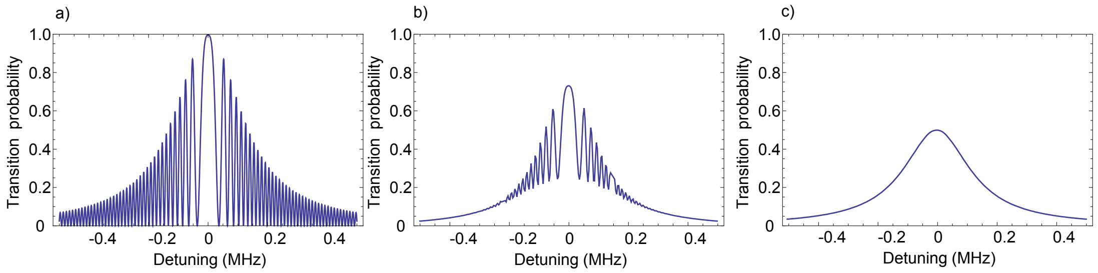

Figure 3.1: Excitation probability as a function of microwave frequency for the $X^1\Sigma^+$ ($v = 0$, $J'' = 0$) - $X^1\Sigma^+$ ($v = 0$, $J' = 1$) transition, a) ignoring all broadning mechanisms. b) and c) includes a 20m/s and 60m/s velocity distribution along the molecular beam axis. This results in a smearing out of the oscillations.

beam axis leads to a spread in interaction times t_0. This smears out the oscillations as shown in figure 3.1 b) and c) where the transition probability was integrated over a 20m/s and 60m/s longitudinal velocity distribution. The resulting excitation probability is a Lorentzian of amplitude 0.5 and width 268kHz. Other smaller mechanisms include the transverse velocity distribution of the molecular pulse and any divergence in the microwave beam, both of which lead to additional detuning in Eq.(3.1) via the Doppler effect.

3.3 The hyperfine structure of the $X^1\Sigma^+$ ($v = 0$, $J = 1$) state

Given that both $\hat{S}$ and $\hat{\Lambda}$ are equal to zero in the ground state, there is no fine structure nor electron-spin-nuclear-spin coupling. However, there are very small splittings due to other couplings. In order to account for these, further terms must be added to the Hamiltonian. The Ramsey Hamiltonian [132] accounts for these terms and is given by

$$\begin{aligned} H = \quad & BJ^2 + c_1\left(\mathbf{I}_{\mathrm{Li}}\cdot\mathbf{J}\right) + c_2\left(\mathbf{I}_{\mathrm{H}}\cdot\mathbf{J}\right) \\ & + c_3\left(\frac{3(\mathbf{I}_{\mathrm{Li}}\cdot\mathbf{J})(\mathbf{I}_{\mathrm{H}}\cdot\mathbf{J}) + 3(\mathbf{I}_{\mathrm{H}}\cdot\mathbf{J})(\mathbf{I}_{\mathrm{Li}}\cdot\mathbf{J}) - 2\mathbf{J}(J+1)\mathbf{I}_{\mathrm{Li}}\cdot\mathbf{I}_{\mathrm{H}}}{(2J-1)(2J+3)}\right) + c_4\left(\mathbf{I}_{\mathrm{Li}}\cdot\mathbf{I}_{\mathrm{H}}\right) \\ & - \mathrm{eq}_1 Q_1\left(\frac{3(\mathbf{I}_{\mathrm{Li}}\cdot\mathbf{J})^2 + \frac{3}{2}(\mathbf{I}_{\mathrm{Li}}\cdot\mathbf{J}) - \mathbf{J}^2\mathbf{I}_{\mathrm{Li}}^2}{2(2J-1)(2J+3)I_{\mathrm{Li}}(2I_{\mathrm{Li}}-1)}\right) - \mathrm{eq}_2 Q_2\left(\frac{3(\mathbf{I}_{\mathrm{H}}\cdot\mathbf{J})^2 + \frac{3}{2}(\mathbf{I}_{\mathrm{H}}\cdot\mathbf{J}) - \mathbf{J}^2\mathbf{I}_{\mathrm{H}}^2}{2(2J-1)(2J+3)I_{\mathrm{H}}(2I_{\mathrm{H}}-1)}\right). \end{aligned} \tag{3.5}$$

J is the usual rotational angular momentum, $\mathbf{I}_{\mathrm{H}}$ and $\mathbf{I}_{\mathrm{Li}}$ are the spins of the hydrogen and the lithium nuclei, whose spin quantum numbers are equal to 1/2 and 3/2 respectively. The first term is the usual rotational Hamiltonian. The second and third terms, with coefficients c_1 and c_2, represent the energy of the interaction between the nuclear spins and the rotation. The fourth term, with the coefficient c_3, is the through-space spin-spin interaction, whereby the magnetic dipoles interact directly. The c_4 term is the electron-coupled spin-spin interaction of the nuclei. The last two terms represent the interaction of the rotating electrons with the electric quadrupole moment of the nucleus. All the coefficients have been previously measured using electric and magnetic molecular beam resonance techniques [133] ($c_1 = 10.054$, $c_2 = -9.345$, $c_3 = 11.346$, $c_4 = 0.135$, $\mathrm{eq_1Q_1} = 346.78$ and $\mathrm{eq_2Q_2} = 0$). The electric quadrupole interaction makes the biggest contribution, so we choose a basis set for which this is already diagonal. The coupling

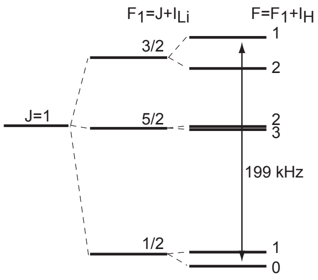

Figure 3.2: Energy level diagram of the hyperfine splitting of the $\mathrm{X}^1\Sigma^+$ $(v = 0,\ J = 1)$ state.

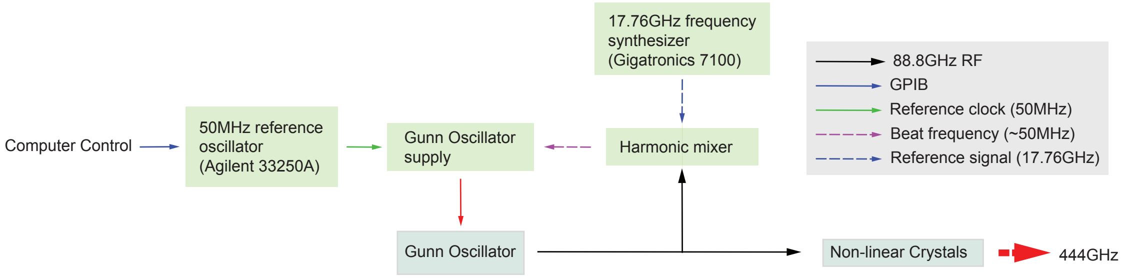

Figure 3.3: Schematic diagram of the microwave source.

scheme of choice is ((J ,I_{Li}) F_1, I_{H}) F, meaning the rotation and the Li nuclear spin are coupled together first, to form a resultant F_1. This is then coupled to the proton spin I_{H} to form the total angular momentum F. Since I_{Li}=3/2 and we are considering the hyperfine structure of the first rotationally excited state (J=1), the possible values of F_1 are 1/2, 3/2 and 5/2. Coupling to I_{H} then gives 6 states with total angular momentum values F=0,1,1,2,2,3.

Working out the matrix elements of the Hamiltonian and diagonalizing gives the eigenstates of the molecule accounting for the hyperfine structure. The energy level diagram is shown in figure 3.2. In our experiment, we have partially resolved these splittings, as will be shown later in the chapter. Note that there is also a splitting in the $J = 0$ state. However, the splitting is 270Hz, which is far below our resolution.

3.4 The experimental setup

3.4.1 The hardware

Figure 3.3 shows a block diagram of the apparatus. The microwaves at 444GHz were produced by quintupling the frequency of a Gunn oscillator. This is a solid state device which resonates at a frequency proportional to the voltage applied across it. It is one of the fastest electronic oscillators available, capable of delivering approximately 2W of power at 88GHz. This output is channelled through non-linear crystals which quintuple the frequency to 444GHz. Approximately 60μW of power is obtained at this frequency. The entire apparatus was commercially available from AB millimetre.

Figure 3.3 also shows the locking mechanism. A harmonic mixer picks off the 5th harmonic of a 17.76GHz frequency stabilized synthesizer (Gigatronics 7100) and beats it against the Gunn

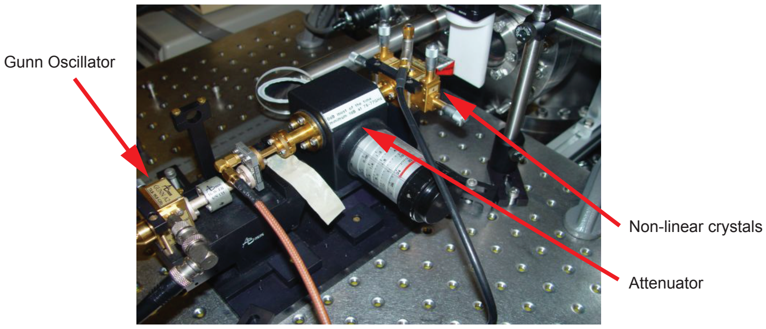

Figure 3.4: Photograph of the apparatus. A PTFE cylinder of diameter 4cm was cut in half to form a lens.

oscillator output. The beat note of the two is compared to a stabilized 50MHz reference (Agilent 33250A) to produce an error signal, which is then sent back to the power supply of the Gunn oscillator. This tunes the voltage fed to the Gunn oscillator such that the beat frequency remains a constant. The result is a phase stable RF signal at 88.8GHz with a linewidth of around 3kHz. The linewidth at 444GHz should therefore be approximately 15kHz.

3.4.2 Aligning the microwave source & scanning the frequency

Figure 3.4 shows a photograph of the microwave source. A lens machined out of a PTFE cylinder (transparent at these wavelengths [134]) is used to focus the microwaves into the chamber (also shown in figure). The diameter of the cylinder was 4cm. For the deceleration data, a commercial Teflon plano-convex lens (Thorlabs LAT100) of focal length 100mm was used.

An obstacle in the alignment of the apparatus was the lack of detection methods. The only way we could observe the microwaves was to use them to drive the rotational transition. The alignment procedure therefore consisted of parking the detection laser onto the R(0) transition and to move the source around in search of any change in signal size. If everything is on resonance, a dip in the LiH signal is observed when the microwaves hit the molecules. The procedure then was to minimize the LiH signal. Once this is done, the procedure is repeated for positioning the PTFE lens.

The computer is fitted with a GPIB board. This allowed the frequency of the 50MHz reference to be controlled remotely from the computer. The control software scans the frequency of the microwaves and records the laser-induced fluorescence as a function of this frequency.

3.5 The data

A laser-microwave double resonance technique was used to scan over the rotational transition. In one data taking mode, the laser frequency was fixed to be resonant with the R(0) or R(1) component of the $A^1\Sigma^+(v''=3)$-$X^1\Sigma^+(v''=0)$ transition, and the microwave frequency was scanned. In the second data-taking mode, the microwave frequency was fixed and the laser frequency was scanned over the optical resonances. Figure 3.5 shows frequency scans with the laser probing the $J''=0$ state and the microwaves on (blue) and off (red). The laser frequency was then changed to probe

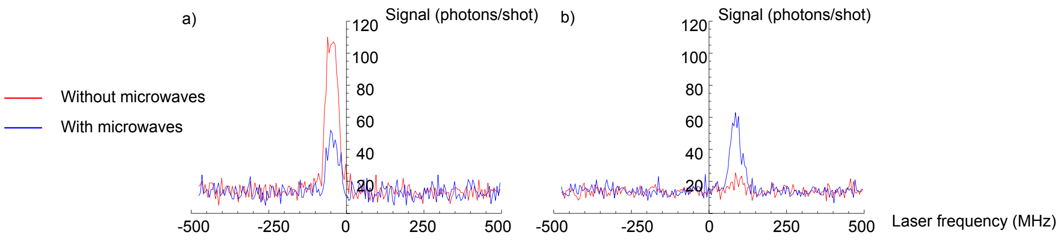

Figure 3.5: Laser frequency scans over the $A^1\Sigma^+(v' = 3)$-$X^1\Sigma^+(v'' = 0)$ resonances with (blue) and without (red) microwaves. a) R(0) line, b) R(1) line.

Table 3.1: Amplitudes from laser frequency scans.

Microwaves	Probe Transition	Amplitude (photons/shot)
On	R(0)	36
Off	R(0)	101
On	R(1)	45
Off	R(1)	7

the J”=1 state and scanned again, with the microwaves on and off. Comparing the signal intensities for the four scans allows the conversion efficiency to be extracted. The observed amplitudes from the 4 scans are shown in table 3.1. First of all, we note that the total number of molecules in the two states has not significantly changed over the data acquisition. With the microwaves off, we have $101 + (3/2)7 = 111$, where the factor of $(3/2)$ is added to compensate for the difference in excitation rates between the R(0) and R(1) transitions. With the microwaves on, we have $36 + (3/2)45 = 103$. We then find that the ratio of the two R(0) amplitudes shows that 64.5% of the molecules were sucessfully pumped out of the ground state and into a rotationally excited state.

Figure 3.6 shows data where the probe laser is tuned to the R(0) transition, while the microwave frequency is scanned. While the microwaves are off resonance, the R(0) signal does not change. As the microwaves become resonant with the J”=0-J’=1 transition, the population is depleted. This depletion gives the population transfer efficiency once the baseline is subtracted. The width of the microwave resonance is found to be 270±10kHz, which is in good agreement with the expected 268kHz estimated from the simple model above. The transfer efficiency measured from this graph is 68%, which is higher than predicted by our model shown in figure 3.1 c). Futher investigation is required in order to fully understand this increase.

Figure 3.7 a) shows 8 measurements of the $X^1\Sigma^+$ ($v = 0$, $J'' = 0$) - $X^1\Sigma^+$ ($v = 0$, $J' = 1$) transition. The grey points correspond to our initial attempts with an inferior locking scheme. The blue points were measured after replacing it with the setup shown in figure 3.3. We measure the transition frequency to be 443952.909MHz, with a statistical uncertainty of 0.0025MHz. The data spans a period of several months over which the microwave source position was repeatedly optimized for the LIF signal. The Doppler shift caused by any misalignment of the microwave beam is believed to be the dominant source of systematic errors. Assuming we know the position

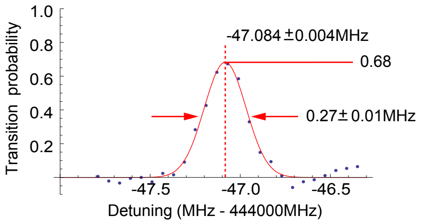

Figure 3.6: Population transfer efficiency for the rotational transition as a function of frequency, extracted from a microwave frequency scan over the J"=0-J'=1 resonance while probing the R(0) line on the detector.

of the beam to within ±0.5cm, the maximum possible deviation of the microwave beam from the molecular beam normal is geometrically constrained to be less than 5.7°, ignoring the effect of the collimating lens. This would lead to an upper bound of ±0.09MHz. This upper bound is very conservative since it is highly unlikely that this degree of angular misalignment was present. Further evidence for this is suggested by the scatter of the data points in the figure. The points have a standard deviation of 0.052MHz, even though the angular alignment was never controlled. Nevertheless, in the absence of any further information, we take the upper bound of 0.09MHz as a conservative estimate of the error bar. We believe that this value could easily be improved by putting more effort into the alignment of the microwave source.

In figure 3.7 b), our measurement of the transition is compared to the measurements made in previous experiments. Plummer *et al.* measured a value of 443952.80±0.05MHz [135] by sending frequency upconverted microwaves from a klystron through a heated absorption cell. 11 years later, Bellini *et al.* also used a heated absorption cell and measured 443952.916±0.12MHz [136], but produced the microwaves by a nonlinear mixing of two frequency stabilized CO_2 lasers and a microwave synthesizer. Despite the possibility of systematic errors, our measured value is very consistent with previous measurements. Our measurement is also the first one to be carried out in a cold molecular beam, which potentially offers an order of magnitude improvement in sensitivity once the systematics are more thoroughly investigated.

The data shown in figure 3.6 was taken with the microwaves at full power. Significant power broadening occurs, prohibiting the observation of the hyperfine structure discussed in section 3.3. By turning the power down, we were able to resolve some of the hyperfine structure, as shown in figure 3.8. Here, the probe laser was tuned to the R(1) line as the noise on the R(0) line was dominated by fluctuations in the molecular flux. Although the reduced microwave power reduces the driving efficiency to the J=1 state (and thus the signal on the R(1) transition), the linewidth narrows, allowing the partial resolution of the hyperfine structure. The $F_1 = 1/2$ states are completely resolved from the rest, and the $F_1 = 3/2$, $5/2$ states are partially resolved from one another. The red curve shows the fit to a sum of 6 Gaussians of equal width whose spectral separations were fixed to the hyperfine splittings calculated in the previous section. The free parameters were a width common to all 6 Gaussians, their amplitudes and a global frequency offset. As a reference, the positions of the peaks are shown in green. The linewidth observed in

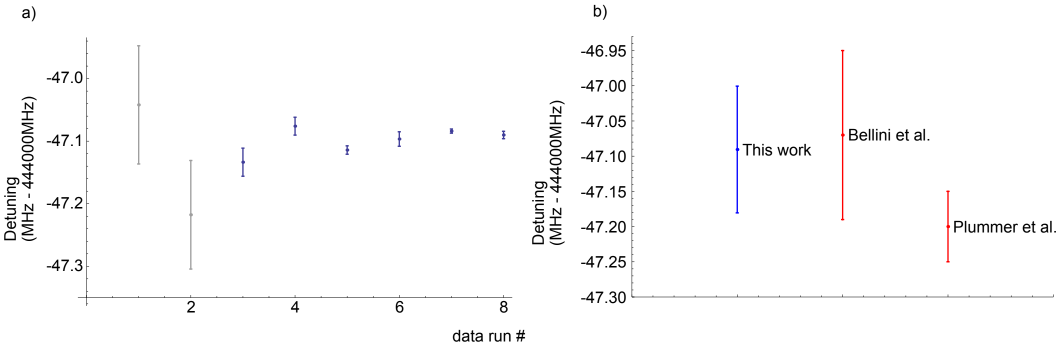

Figure 3.7: a) 8 measurements of the $X^1\Sigma^+$ ($v = 0$, $J'' = 0$) - $X^1\Sigma^+$ ($v = 0$, $J' = 1$) transition. The grey measurements (first two points on the left) are our first microwave scans, which were made with an inferior locking scheme. b) Our measurement in comparison to Plummer *et al.*'s [135] and Bellini *et al.*'s [136] values.

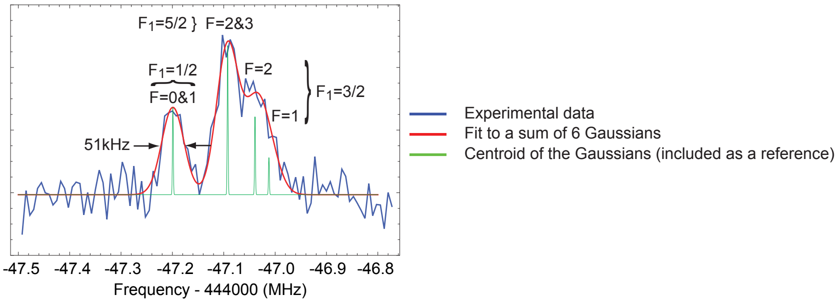

Figure 3.8: Microwave frequency scan over the J"=0-J'=1 resonance while probing the R(1) line by laser-induced fluorescence. The power was reduced to the minimum amount needed to observe a signal. The F_1=3/2, 5/2 states are partially resolved from each other. The F_1=1/2 states are completely resolved from the rest.

the spectrum is around 51kHz. This may indicate that the lines are still power broadened, but we could not afford to reduce the power any further as it would have resulted in more losses in signal.

3.6 Conclusion

In order to bring the molecules to rest using a Stark decelerator, they needed to be pumped from the ground state to the first rotationally excited J=1 state. This transition was driven using microwaves at 444GHz, obtained by frequency quintupling the output of a Gunn oscillator at 88.8GHz. The apparatus produced 60μW of power with a linewidth of around 15kHz. At full power, a driving efficiency of up to 68% was measured. By turning down the power, some of the hyperfine structure of the J=1 state, caused by nuclear electric quadrupole and nuclear magnetic dipole moments, was resolved. The measured rotational transition is at a frequency of 443952.91±0.09MHz, in agreement with the two other measurements of similar precision.

Chapter 4

Stark deceleration of lithium hydride molecules

4.1 Introduction

The interaction between electric fields and molecules, known as the Stark effect, can be used to decelerate and focus molecules. The first successful experimental implementation of Stark deceleration reduced the speed of a pulsed beam of metastable CO molecules in the $a^3\Pi$ state from 225 m/s ($E_{\text{kin}} = 59\text{cm}^{-1}$) to 98m/s ($E_{\text{kin}} = 11\text{cm}^{-1}$) [2]. The Stark decelerator used in this experiment consisted of an array of 63 synchronously pulsed electric field stages, each designed to have a focusing effect which forced the molecules to stay together during the entire process. Since the original paper in 1999 [2], several molecules have been decelerated using the same technique, including OH [75, 76], ND_3 [77], NH [78], H_2CO [33] and SO_2 [79].

This thesis reports the first successful Stark deceleration of lithium hydride molecules. Although its large dipole moment of 5.88 Debye [129] and low mass make LiH attractive for deceleration experiments, it has never previously been decelerated because of the difficulty of producing a low temperature gas-phase sample (see chapter 2). This chapter covers the theory of Stark deceleration, the experimental setup and the results obtained, and concludes with an outlook for future experiments.

4.2 Theory

4.2.1 Stark effect of LiH

Consider the interaction between a dipolar molecule and an applied electric field $\mathbf{E}$, which we choose to be along Z. This interaction adds a term $\hat{H}'$ to the total Hamiltonian, where

$$\hat{H}' = -\hat{\mathbf{D}} \cdot \hat{\mathbf{E}}. \tag{4.1}$$

$\hat{\mathbf{E}}$ is the operator for an external electric field and $\hat{\mathbf{D}}$ is the electric dipole moment operator as given in Eq.(2.37). The Schrödinger equation becomes:

$$\left(\hat{H}^0 + \hat{H}'\right)|\Psi'\rangle = E_n|\Psi'\rangle, \tag{4.2}$$

where $\hat{H}^0$ is the Hamiltonian of the molecule in the absence of the electric field (see section 2.5.2). We choose to solve the Schrödinger equation by working in the basis of the field-free states $|\Psi_a\rangle$. The new states $|\Psi'_n\rangle$ are therefore given by

$$|\Psi'_n\rangle = \sum_a w_{na}|\Psi_a\rangle, \tag{4.3}$$

where $w_{na} = \langle\Psi_a|\Psi'_n\rangle$ are the expansion coefficients. This is convenient because $H^0|\Psi_a\rangle = E^0_a|\Psi_a\rangle$. As shown on page 39 of [130], Eq.(4.2) is re-written

$$\sum_a \langle\Psi_b|\left(\hat{H}^0 + \hat{H}'\right)|\Psi_a\rangle\langle\Psi_a|\Psi'_n\rangle = E_n\langle\Psi_b|\Psi'_n\rangle. \tag{4.4}$$

Eq.(4.4) can then be written in matrix form, as

$$\begin{aligned}\begin{pmatrix} H'_{1,1}+E^0_{1,1} & H'_{1,2} & H'_{1,3} & \cdots \\ H'_{2,1} & H'_{2,2}+E^0_{2,2} & H'_{2,3} & \cdots \\ H'_{3,1} & H'_{3,2} & H'_{3,3}+E^0_{3,3} & \cdots \\ \cdots & \cdots & \cdots & \cdots \end{pmatrix} \cdot \begin{pmatrix} \langle\Psi_1|\Psi'_n\rangle \\ \langle\Psi_2|\Psi'_n\rangle \\ \langle\Psi_3|\Psi'_n\rangle \\ \cdots \end{pmatrix} \\ = E_n \begin{pmatrix} \langle\Psi_1|\Psi'_n\rangle \\ \langle\Psi_2|\Psi'_n\rangle \\ \langle\Psi_3|\Psi'_n\rangle \\ \cdots \end{pmatrix},\end{aligned} \tag{4.5}$$

where H'_{ab} is equal to $\langle\Psi_a| - \hat{\mathbf{D}}\cdot\hat{\mathbf{E}}\ |\Psi_b\rangle$. a and b represent the quantum numbers of our field-free states

$$|\Psi\rangle = |n\rangle|v\rangle|J, m_J\rangle,$$

where $|n\rangle$ is the electronic, $|v\rangle$ the vibrational and $|J, m_J\rangle$ the rotational states. The solutions to Eq.(4.5) are found by diagonalizing the matrix on the LHS. Noting that $\hat{\mathbf{D}}\cdot\hat{\mathbf{E}}$ is equal to $\hat{D}\ \hat{E}\cos\theta$, where θ is the angle between the lab-frame axis Z and the molecule-fixed axis z, the matrix elements are given by

$$\langle\Psi_a|\hat{\mathbf{D}}\cdot\hat{\mathbf{E}}|\Psi_b\rangle = D^X|\mathbf{E}|\langle J', m'_J|\ Y_{l,m}(\theta,\phi)\ \mid J', m'_J\rangle \tag{4.6}$$

where D^X is the permanent electric dipole moment of the X$^1\Sigma^+$ state, equal to 19.6 × 10^{-30}Cm. Using the mathematical formalism of spherical tensor operators and Wigner rotation matrices, the Stark Hamiltonian's matrix elements $\langle J', m'_J|H'|J, m_J\rangle$ can be written as

$$\begin{aligned} D|\mathbf{E}|\langle J', m'_J|\ \mathcal{D}^{(1)}_{0,0}(\theta,0,0)\ |J'', m''_J\rangle &= (-1)^{m_J} D\ |\mathbf{E}|\left((2J+1)(2J'+1)\right)^{1/2} \\ &\times \begin{pmatrix} J' & 1 & J \\ m'_J & 0 & -m_J \end{pmatrix}\begin{pmatrix} J' & 1 & J \\ 0 & 0 & 0 \end{pmatrix}. \end{aligned} \tag{4.7}$$

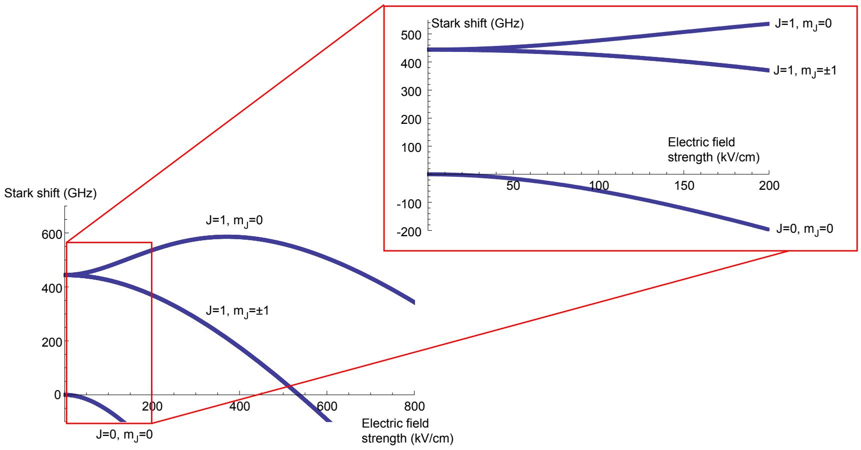

Figure 4.1: Energies of ^{7}LiH $^1\Sigma^+(v = 0, J = 0-1)$ states as a function of electric field strength

We are now in a position to diagonalize Eq.(4.5) for any value of $|\mathbf{E}|$. As 90% of the molecules in our beam are in the absolute ground state, we will only attempt to solve Eq.(4.2) for the first few rotational states. Since we are expressing the new states as a sum of field-free states (see Eq.(4.3)), the calculated shifts in energy are more accurate as more states are taken into account. However, this does require the diagonalisation of a larger matrix. Figure 4.1 shows the Stark shift of ^{7}LiH $^1\Sigma^+(v = 0, J = 0-1)$ states as a function of the electric field strength, calculated using the first nine J states (from $J = 0$ to $J = 8$). Figure 4.1 shows that the ground state shifts downwards as the electric field strength is increased. The degeneracy of the $J = 1$ states is lifted in the presence of an electric field. The $m_J = 0$ state is pushed upwards in energy with increasing field, while the $m_J = \pm 1$ states, which do remain degenerate, decrease in energy with increasing field. At around 400 kV/cm, however, the $m_J = 0$ state reaches a turning point beyond which the energy decreases again with increasing field strength. Note that the Stark shift is only dependent on the magnitude of the field $|\mathbf{E}|$, and not on its sign. The decelerator in our experiment makes use of the upward shift in the $J = 1$, $m_J = 0$ state.

4.2.2 Manipulating molecules in a decelerator

A molecule in the presence of an electric field feels a force given by the spatial gradient of the Stark shift, W:

$$\mathbf{F} = -\nabla W = -\frac{dW}{d|E|}\nabla|E|. \tag{4.8}$$

In some cases, such as CO in the $a^3\Pi_1(v = 0, J = 1)$ states, the Stark shift is almost linear in electric field [137]. This makes dW/dE a constant, prompting the introduction of an effective dipole moment d_{eff} equal to dW/dE. Given the non-linear Stark shift of LiH, this is a poor approximation (see figure 4.1) and thus will not be used.

The sign of the force is determined by the sign of dW/dE. Molecules in states with a positive dW/dE feel an attraction to high electric field strengths and are called ‘high-field seekers’. Conversely, molecules in states with a negative dW/dE feel a repulsion, thus labelled ‘low-field

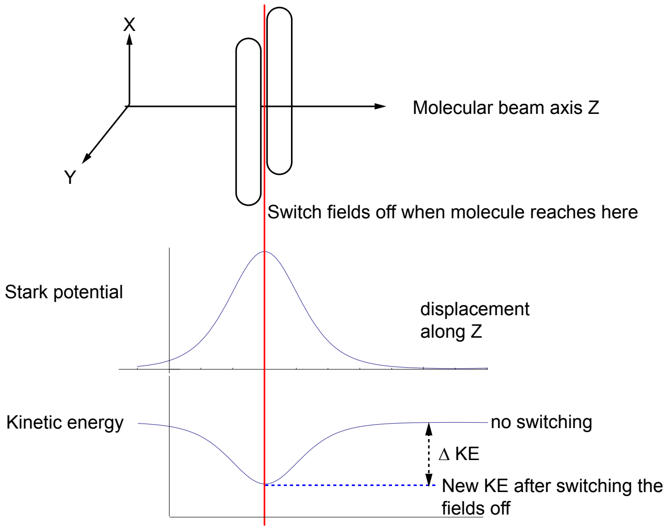

Figure 4.2: The Stark potential and kinetic energy along the molecular beam axis as the molecule travels between an electrode pair. The red line shows the position of the molecule when the voltage is switched off for maximum deceleration.

seekers'. Figure 4.1 therefore shows that molecules in the $J = 0$ ground state and $J = 1$, $m_J = \pm 1$ states are high-field seeking, while molecules in the $J = 1$, $m_J = 0$ state are low-field seeking up to around 400kV/cm. All states become strong-field seeking in very large fields. Note that the absolute ground state of any molecule is always high-field seeking [90].

Auerbach *et al.* showed that electrostatic focussing of weak-field seekers is possible because $\nabla \cdot \mathbf{F} < 0$ [85]. $\nabla \cdot \mathbf{F}$ is greater or equal to 0 for strong-field seekers, a situation analogous to Earnshaw's theorem for charged particles [83]. No electrode geometry can create an electrostatic free-space maximum where high-field seekers can converge to. Instead, they will be attracted to the electrodes where the field is strongest, making the manipulation of high-field seeking molecules very difficult. Attempts have been made to circumvent this problem, such as using alternating gradient focussing [138, 85]. The deceleration of YbF molecules in their ground state has been demonstrated using this technique [90]. However, we chose to drive the rotational transition to the $J = 1$, $m_J = 0$ weak-field seeking state instead of decelerating ground state molecules (see chapter 3).

Figure 4.2 is an illustration of how the Stark effect can be used to decelerate a molecule. For the moment, the motion of a single molecule referred to as the 'synchronous molecule' is considered. The molecule travels along Z passing between a pair of electrodes charged to high voltage. The potential created by the Stark shift causes a change in kinetic energy as the molecule travels between the electrodes. If the molecule is in a weak-field seeking state, the velocity v_Z will decrease as the molecule climbs the potential and will increase again as the molecule exits from between the electrodes. However, if the electric fields are switched off while the molecule is at the top of the potential, the molecule will not accelerate while exiting the stage, causing an overall loss of kinetic energy.

Figure 4.1 shows that the maximum kinetic energy which can be extracted from a single stage is the maximum Stark shift the electrodes can induce on the molecules. For LiH, this is on the order of 25GHz when applying ±10kV. Our source produces beams of LiH at 600m/s using Ar or 420m/s using Kr as the carrier gas (see chapter 2.1), corresponding to kinetic energies of h × 3.62THz and h × 1.77THz respectively. It is therefore impossible to bring the molecules to rest in a single stage. However, by aligning a series of electrode pairs the molecules can eventually be brought to rest. The minimum number of deceleration stages needed can be found from figure 4.1. The number of stages N is given by $mv^2/(2\Delta W)$, which is equal to 145 stages for Ar and 71 stages for Kr when working at 100kV/cm. As shown later the amount of extracted energy per stage must be reduced in order to allow the deceleration of a packet of molecules.

Our decelerator has 100 deceleration stages and is similar in design to those used previously e.g. [2]. The first stage consists of an oppositely charged pair of 3mm diameter rods whose axes lie parallel to the Y-axis and are positioned at X=±2.5mm. All odd numbered stages are identical to the first and form an array with a 12mm period along Z. Even numbered stages form a similar array, shifted by 6mm along Z and rotated by 90° about the Z-axis.

For a sequence of deceleration stages, the high voltage must be switched on and off at the correct times. A molecule should always enter a stage which is switched on. Then, once the molecule travels up the potential hill, the voltage must be switched off. This requires a specific switching pattern if the molecule is to be successfully decelerated. The kinetic energy lost over an even numbered stage is given by

$$\Delta W = -(W_{\mathcal{X}}(Z_{\mathcal{X}}, t) - W_{\mathcal{X}}(Z_{\mathcal{X}} + \Delta Z, t)), \tag{4.9}$$

where state '$\mathcal{X}$' has all stages orientated along the X axis switched on while those along Y are left off. In this state, the molecules will be focussed along Y. State '$\mathcal{Y}$' denotes the reverse, where the electrodes along Y are on and those along X are off, thus focussing along X. The decelerator switches between state $\mathcal{X}$ and $\mathcal{Y}$ depending on the molecular position. $Z_{\mathcal{X}}$ denotes the position of the molecule when the decelerator is switched to state $\mathcal{X}$, and ΔZ denotes the distance travelled by the molecule until the switch is thrown a second time. Figure 4.3 provides an illustration of a switching pattern and the kinetic energy lost in one stage. The kinetic energy loss along an odd numbered stage is found by reversing the $\mathcal{Y}$ and $\mathcal{X}$ labels.

We see from Eq.(4.9) that the most deceleration occurs when the difference in Stark potential between state $\mathcal{X}$ and $\mathcal{Y}$ is greatest, which is when the molecule reaches the top of a potential. If we now define the switch timings of the decelerator such that the molecule's position with respect to each stage is always the same, the time dependence of ΔW is dropped. A constant amount of kinetic energy is thus extracted at each deceleration stage, and ΔZ in Eq.(4.9) becomes L, the distance between two stages. This is illustrated in figure 4.3, where the switch timings are chosen such that the molecule is always 'at the same position on the potential' when the switch occurs. Because of the periodicity of Stark decelerators, spatial coordinates Z along the molecular beam axis are often expressed in terms of reduced position θ [139], such that $\theta = \pi z/L$ where L is the distance between two stages. Figure 4.3 shows the molecular beam axis coordinates expressed in terms of reduced position. The decelerator is switched every time the synchronous molecule reaches

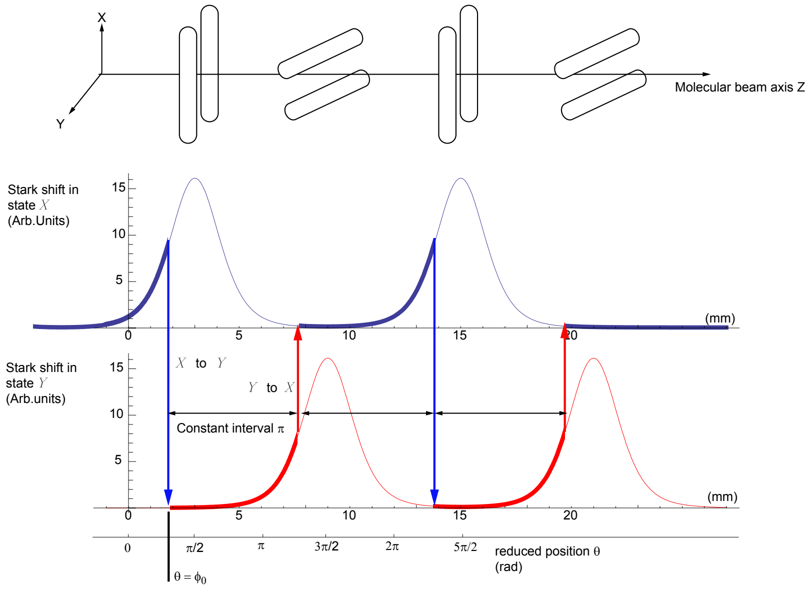

Figure 4.3: Stark potential along the molecular beam axis. The switch positions corresponding to $\Delta W = a\Delta W_{\max}$ (a is a constant) are shown by vertical arrows. The potentials seen by the molecule are highlighted. By switching when the molecule travels a fixed distance, a fixed amount of kinetic energy is extracted at every stage. The reduced position θ is also shown.

a particular position called the synchronous phase angle ϕ_0. This notation will be used throughout this thesis in order to remain consistent with the literature. For the synchronous molecule, θ increases by π between one switch and the next. ΔW can be written in terms of ϕ_0 as

$$\Delta W(\phi_0) = -(W(\phi_0) - W(\phi_0 + \pi)). \tag{4.10}$$

In the general case, Eq.(4.10) does not yield analytical expressions. This is because neither the Stark shift nor the electric fields in the decelerator can be expressed analytically. An exact map of the Stark potential as a function of position can only be obtained numerically through a finite element calculation, which is what is done to calculate the switch times for our decelerator. Figure 4.4 is a map of ΔW in the X-Z plane, obtained numerically by using Eq.(4.10), the Stark shift from figure 4.1 and a map of the electric field strength calculated using FEMLAB. Note that a negative ΔW implies an acceleration of the molecule. The switch times calculated using this Stark potential are applied to the decelerator. Once $\Delta W(\phi_0)$ is known, the kinetic energy change and velocity of the molecule after n stages can be calculated. These are given by

$$W_n = KE_i - n\Delta W(\phi_0), \tag{4.11}$$

$$v_n = \sqrt{v_i^2 - \frac{2n}{m}\Delta W(\phi_0)}, \tag{4.12}$$

where n is the number of stages used for the deceleration, m is the mass of the molecule and KE_i is the initial kinetic energy. The time $t_{\mathrm{off}}^{\mathrm{n}}$ for the n$^{\mathrm{th}}$ turn-off is given by

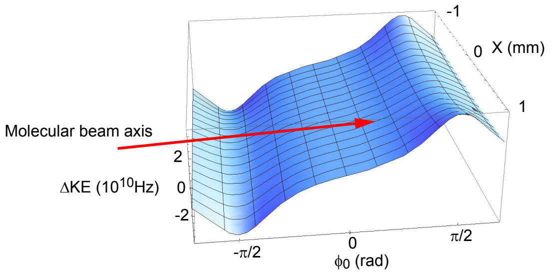

Figure 4.4: Map of ΔW in the X-Z plane, created using Eq.(4.10), the Stark shift from figure 4.1 and a map of the electric field strength calculated using FEMLAB. The molecular beam axis Z is indicated by the red arrow.

$$t^{\mathrm{n}}_{\mathrm{off}} = t^{\mathrm{n}}_{\mathrm{on}} + \int_{Z_{\mathrm{on}}}^{Z_{\mathrm{off}}} \frac{dz}{\sqrt{v_{n-1}^2 + 2\Delta W/m}}, \tag{4.13}$$

where $t^{\mathrm{n}}_{\mathrm{on}}$ is the n^{th} turn-on time.

Although the exact kinetic energy change of a molecule can only be calculated numerically, some approximations allow analytical expressions to be extracted. This is useful for understanding the behaviour of the decelerator. One common approximation is to Fourier expand ΔW, giving

$$\Delta W\left(\phi_0\right) = \sum_{n=1}^{\infty} k_n \sin\left(n\phi_0\right), \tag{4.14}$$

where k_n are constants and $\sum_n k_n$ is the maximum extractable energy per stage. In most previous experiments (e.g. OH [111, 76], NH_3 [140], CO [140]), W is almost linear in electric field strength, allowing everything except the first term of Eq.(4.14) to be omitted [140]. Having to account for higher order terms illustrates the difference between the behaviour of linear Stark-shift molecules and LiH in a decelerator. Other than LiH, SO_2 is the only molecule with a very non-linear Stark shift to have been successfully decelerated [79].

4.2.3 Phase stability

Having covered the deceleration of a single molecule (the synchronous one), we now turn to the trajectories of non-synchronous molecules. These are molecules whose initial positions and velocities are different to those of the synchronous one.

By switching the decelerator when the synchronous molecule is only part-way up the potential hill, there will be a group of molecules which are forced to stay close to the synchronous molecule throughout the process. Qualitatively, the effect is illustrated in figure 4.5. This figure shows a typical deceleration stage, where the fields are switched when the synchronous molecule reaches a certain height up the potential hill, marked by a green line. A non-synchronous molecule that is ahead of the synchronous one will climb further up the hill before the fields are switched. This will cause it to lose more kinetic energy than the synchronous molecule. Conversely, a molecule which is behind the synchronous one will see the fields switched before reaching the green line, meaning that it will lose less kinetic energy than the synchronous molecule. Thus, molecules that

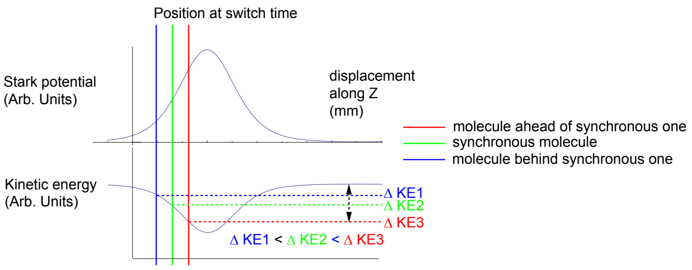

Figure 4.5: The change in kinetic energy of non-synchronous molecules. Molecules which are ahead/behind (in red and blue) than the synchronous molecule (in green) lose more/less kinetic energy, resulting in bunching of the molecular pulse.

are slightly displaced from the synchronous molecule are still caught in the 'travelling potential well' [141]. This principle is called 'phase stability'.

The phase of a non-synchronous molecule ϕ is related to the phase of the synchronous molecule by $\phi = \phi_0 + \delta$. The kinetic energy loss of a non-synchronous molecule $\Delta W(\phi)$ is then given by $\Delta W(\phi_0 + \delta)$. The equation of motion for the non-synchronous molecule relative to the synchronous one can be found by approximating the force on the synchronous molecule as being a constant in time. This approximation is valid so long as the change in velocity per stage, Δv, is small compared to the molecular velocity v. The equations of motion for the synchronous and non-synchronous molecules are then given by

$$m\frac{d^2 z_0}{dt^2} = \frac{\Delta W(\phi_0)}{L} \tag{4.15}$$

and

$$m\frac{d^2 z}{dt^2} = \frac{\Delta W(\phi)}{L}, \tag{4.16}$$

where m is the mass of the molecule, and L is the distance between two stages, as before. Here, we have made the further approximation that the distance moved by the non-synchronous molecule in the time between switches is also L. This is valid provided the difference in velocities between synchronous and non-synchronous molecules is small compared to the mean velocity. Remembering that $z = (\phi L)/\pi$ and $z_0 = (\phi_0 L)/\pi$, Eq.(4.15) and Eq.(4.16) are re-written as

$$\frac{mL}{\pi}\frac{d^2\phi_0}{dt^2} = \frac{\Delta W(\phi_0)}{L} \tag{4.17}$$

and

$$\frac{mL}{\pi}\frac{d^2\phi}{dt^2} = \frac{\Delta W(\phi)}{L}. \tag{4.18}$$

By subtracting Eq.(4.17) from Eq.(4.18) and rearranging, we obtain

$$\frac{mL^2}{\pi}\frac{d^2\delta}{dt^2} = \Delta W(\phi_0 + \delta) - \Delta W(\phi_0). \tag{4.19}$$

The kinetic energy change over a deceleration stage for a synchronous molecule, $\Delta W(\phi_0)$, was given in Eq.(4.10). We then define the relative velocity $\nu = v - v_0$. Since $v = (L/\pi)d\phi/dt$ and $v_0 = (L/\pi)d\phi_0/dt$, ν equals $(L/\pi)d\delta/dt$. It then follows that

$$\frac{d^2\delta}{dt^2} = \frac{d}{dt}\left(\frac{d\delta}{dt}\right) = \frac{d}{dt}\left(\frac{\pi}{L}\nu\right) = \frac{\pi}{L}\frac{d\nu}{d\delta}\frac{d\delta}{dt} = \frac{\pi^2}{L^2}\nu\frac{d\nu}{d\delta}.$$

Rearranging Eq.(4.19) then gives

$$m\pi\nu\frac{d\nu}{d\delta} = \Delta W\left(\phi_0 + \delta\right) - \Delta W\left(\phi_0\right). \tag{4.20}$$

Having eliminated time from the equation, the Fourier expansion of Eq.(4.14) can be inserted into the RHS of Eq.(4.20). Integrating with respect to δ then gives

$$\int m\pi\nu\frac{d\,\nu}{d\delta}d\delta = \int\sum_{n=1}^{\infty} k_n\left[\sin\left(n\left[\phi_0+\delta\right]\right) - \sin\left(n\phi_0\right)\right]d\delta,$$

$$\frac{1}{2}m\pi\nu^2 + \sum_{n=1}^{\infty} k_n\left[\frac{\cos\left(n\left[\phi_0+\delta\right]\right)}{n} + \delta\sin\left(n\phi_0\right)\right] = \text{constant}. \tag{4.21}$$

Remembering that $\sum_n k_n$ is the total extractable energy per stage, we define normalized Fourier expansion coefficients a_n such that $\sum |a_n| = 1$ and

$$k_n = \frac{kmv_i^2}{2}a_n, \tag{4.22}$$

where k^{-1} is the minimum number of stages required to extract the initial kinetic energy $1/2mv_i^2$. After inserting Eq.(4.22) back into the equation of motion, we obtain

$$\nu^2 + \frac{kv_i^2}{\pi}\sum_{n=1}^{\infty} a_n\left[\frac{\cos\left(n\left[\phi_0+\delta\right]\right)}{n} + \delta\sin\left(n\phi_0\right)\right] = \text{constant}, \tag{4.23}$$

where the constant in Eq.(4.23) is proportional to the energy of the molecule relative to that of the synchronous molecule. This is the energy conservation equation for the relative motion of a non-synchronous molecule, with the terms in the sum acting as a potential. This potential is shown in figure 4.6. a) shows the potential when retaining only the first term of the expansion, while b) shows the potential when the first 5 non-zero terms are retained. Potential wells are observed in both cases, allowing the molecules to be trapped around the synchronous molecule. Furthermore, as ϕ_0 is increased, the depth of these wells decrease. At $\phi_0 = 90°$, the well has vanished. For figure 4.6, k and v_i were set to 0.014 and 420m/s respectively. The coefficients a_n were found by fitting to ΔW calculated numerically. Figure 4.7 shows the numerical ΔW (blue line) as a function of ϕ, along with the Fourier expansion retaining the first five non-zero terms (red dashed line) and a simple sinusoid (green dashed line). We find that $a_1 = 0.791$, $a_3 = -0.178$, $a_5 = 0.027$ and $a_7 = -0.004$. The terms with even n are zero by symmetry, and all terms where $n > 7$ are smaller than 10^{-3}.

Phase space plots resulting from retaining only the first term in the Fourier expansion are shown in previous work on Stark deceleration [140], [142]. Figures 4.8 a) and b) reproduce this previous work, where the constant contours of Eq.(4.23) are plotted in phase-space for $\phi_0 = 0°$ and

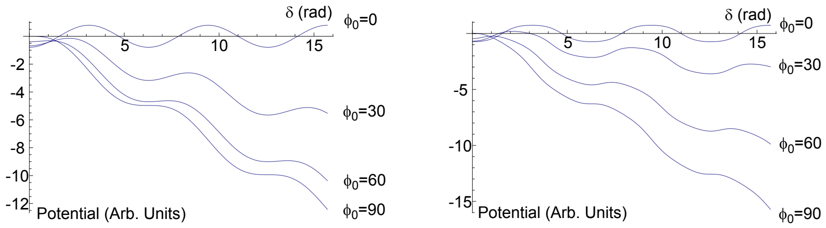

Figure 4.6: Potential seen by non-synchronous molecules. The potential was calculated by retaining a) only the first term b) the first 5 non-zero terms of the Fourier expansion in Eq.(4.14).

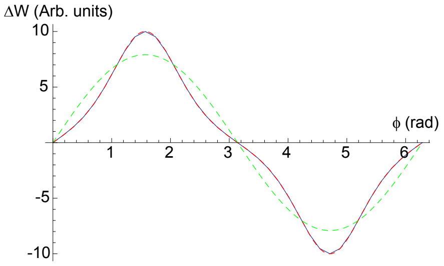

Figure 4.7: ΔW as a function of ϕ. The numerical result (blue line) is compared to Fourier expansion with five non-zero terms (red dashed line) and a simple sinusoid (green dashed line).

$\phi_0 = 60°$. The figure shows that non-synchronous molecules follow stable oscillations around the synchronous one, provided their energies are no greater than the height of the potential well. This is how a packet of molecules can be decelerated. The longitudinal acceptance of the decelerator is then given by the area enclosed by the largest closed trajectory, referred to as the separatrix. Figure 4.8 shows that increasing the switching phase angle ϕ_0 decreases the acceptance. This is a fundamental property of phase stability. On one hand, it is desirable to extract as much kinetic energy as possible. On the other hand, increasing the amount of kinetic energy extracted results in fewer molecules being successfully decelerated for a given initial phase space density. It is therefore critical to have a cold sample of molecules to begin with. Figures 4.8 c) and d) show phase space plots for the same ϕ_0 values, except five terms of the Fourier expansion have been retained. The differences between a) and c), b) and d) highlight the effect of the non-linear Stark potential of LiH. Although the trajectories are clearly deformed with respect to the linear case, 'travelling potential wells' are nonetheless formed allowing LiH molecules to be decelerated.

The separatrices for various phase angles ϕ_0 are shown in figure 4.9. Once again, a) shows the case of retaining only the first term of the Fourier expansion while b) shows the separatrices when the first five terms are retained. We notice that at high phase angles, b) has a larger acceptance. This is because more kinetic energy would be extracted at ϕ_0=60° if the potential were sinusoidal.

4.2.4 Transverse motion

In the transverse directions X and Y, the Stark shift works to our advantage in the case of molecules in weak field seeking states. The field strength is higher at the electrodes, causing molecules to be repelled by them. A 2-D model of the electric field from a single electrode pair gives some insight

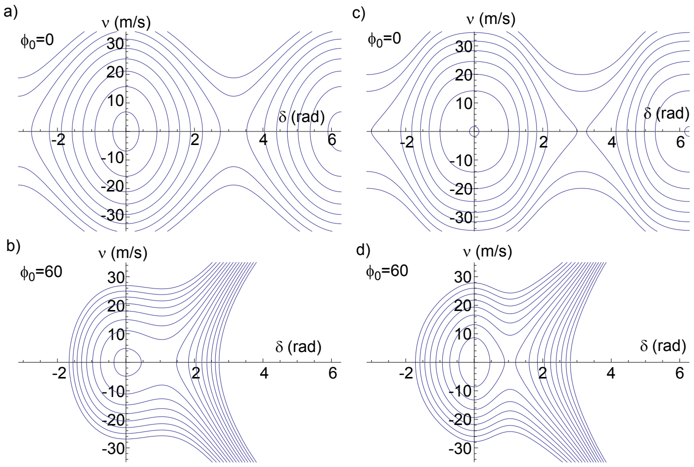

Figure 4.8: Phase space plots solving Eq.(4.23) for a) $\phi_0 = 0°$ and b) $\phi_0 = 60°$ retaining only the first term of the Fourier expansion. In c) and d), we keep the first 5 terms of the expansion.

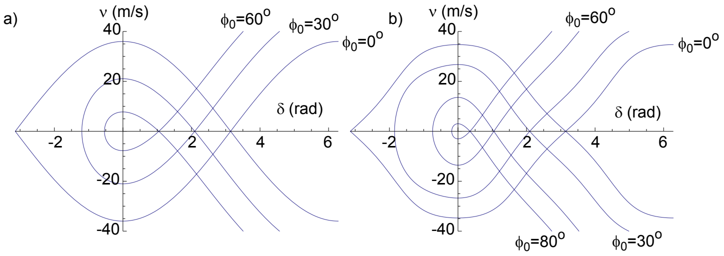

Figure 4.9: Separatrices for various phase angles calculated retaining only a) the first term b) the first five terms of the Fourier expansion. The acceptance is bigger at high phase angles in b).

into the transverse motion. We want to find the electric field due to two infinitely long cylindrical electrodes with radii 1.5mm, their axes parallel to the Y-axis and separated by 5mm. To solve this problem, first consider the related problem of two infinite parallel line-charges of charge per unit length λ lying parallel to the Y axis and placed a distance d apart. The electric field from an infinite line charge can be derived from Gauss's law and is given by $\mathbf{E} = \lambda/(2\pi\epsilon_0\rho)\hat{\rho}$ where ρ is the radial distance from the line. Integrating with respect to ρ gives the potential $V = (\lambda/2\pi\epsilon_0)\ln(\rho)$. Potentials being scalars, the contributions from each line charge can be added. V in the X-Z plane is then given by

$$V(X,Z) = \left(\frac{\lambda}{4\pi\epsilon_0}\right) \ln\left(\frac{(X-d/2)^2+Z^2}{(X+d/2)^2+Z^2}\right), \tag{4.24}$$

assuming both lines have the same charge per unit length. As before, X is the transverse axis, and Z is the molecular beam axis. Using Eq.(4.24), values of λ and d can be fixed such that the equipotential surface corresponding to a desired voltage matches the contour of the electrode surface in the X-Z plane, as illustrated in figure 4.10.

Since V and λ are constant for a given potential, the equipotentials are defined only by the argument of the logarithm. We set

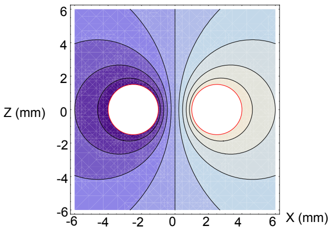

Figure 4.10: Cross-section of electric potential caused by 2 line charges along the Y axis (into page). Values of λ and d are fixed such that the equipotential surface matches the required electrode surface.

$$\chi = \frac{(X - d/2)^2 + Z^2}{(X + d/2)^2 + Z^2} = \exp\left(\frac{4\pi\epsilon_0 V}{\lambda}\right). \tag{4.25}$$

Expanding and rearranging Eq.(4.25) gives

$$Z^2 + (X - a)^2 = a^2 - \left(\frac{d}{2}\right)^2, \tag{4.26}$$

where $a = (d/2)(1-\chi)/(1+\chi)$. This is an equation for a circle with radius $\sqrt{a^2 - (d/2)^2}$ displaced by a from the origin in the X-direction. Setting this radius to that of our electrodes, R, we obtain the required value of d:

$$d = 2\sqrt{a^2 - R^2}. \tag{4.27}$$

For our decelerator, $R = 1.5$mm and $a = 2.5$mm, giving $d = 4$mm. This result confirms intuition in so far as the distance between the line-charges is smaller than the electrode centre-to-centre distance, and their positions are independent of the applied voltage.

Once the correct values of λ and d are found, the field from the line-charges represents the field produced by the electrode pair exactly (outside the electrode surface). Using those values and Eq.(4.24), a map of the electric field strength $|\mathbf{E}|$ is obtained by remembering that $\mathbf{E} = -\nabla V$. Knowing the Stark shift as a function of $|\mathbf{E}|$ (see figure 4.1), a map of W can be plotted, as shown in figure 4.11. The figure shows an approximately parabolic potential in the transverse direction for all values of Z. However, the depth of the potential varies greatly over a deceleration stage. Close to the electrodes ($Z \approx 3$mm), the potential is much deeper, leading to tighter focussing. Further away from the electrodes, the focussing is much weaker. Also, the model fits results obtained from the finite element model of the decelerator very well when close to the electrodes, though less well further away from the electrodes. This is because the line-charge model only accounts for one deceleration stage, unlike a real decelerator which is a sequence of closely-spaced stages. There appears to be no analytical solution for the electric field strength created by a sequence of rod-pairs. If the stages of the decelerator were well separated (which they are not), the potential for N pairs of line-charges would be a good approximation to the decelerator.

From Eq.(4.8), the transverse force seen by the molecules can be calculated and is shown in figure 4.12 a). This indeed shows a restoring force towards the molecular beam axis. The variation in the magnitude of the restoring force over a deceleration stage follows the variation in W seen

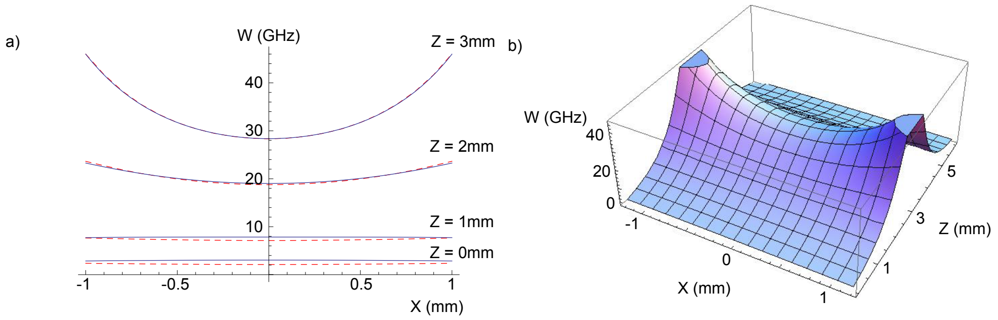

Figure 4.11: Map of W for a deceleration stage centred at $Z = 3$mm, calculated using the line-charge model. Blue lines in a) show $W(X)$ for Z =0, 1, 2 and 3mm. Red dashed lines are calculated using the electric field strength map from FEMLAB for comparison. b) shows a 2D map of W calculated using the line-charge model.

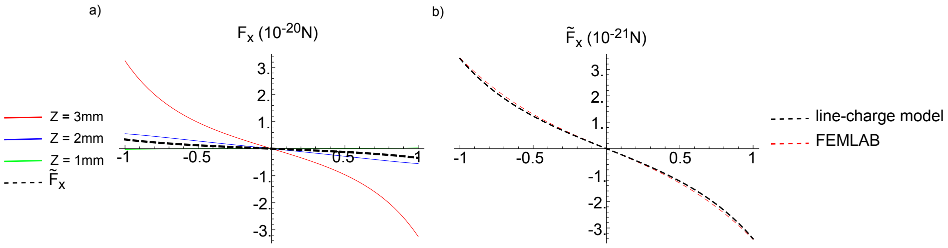

Figure 4.12: a) Transverse force F_X for Z=1mm (green), 2mm (blue) and 3mm (red), and average force $\tilde{F}_X$ (black dashed) as a function of transverse position X. b) comparison of line charge model $\tilde{F}_X$ to numerical $\tilde{F}_X$. The rods are centred at $Z = 3$mm.

in figure 4.11 a). In order to get a qualitative understanding of the transverse focussing in a decelerator, we integrate over the forces felt by the molecule along Z. This approximation is valid provided the spatial period (≈L) of the force fluctuations felt by the molecule is short compared to the wavelength of the transverse oscillations of the molecules, as will be shown later to be the case. The averaged transverse force $\tilde{F}_X$ is given by

$$\tilde{F}_X = \frac{1}{L}\int_0^L -\frac{\partial W}{\partial X}\, dZ, \tag{4.28}$$

where L is the distance between two stages. The transverse motion of molecules in a decelerator can thus be reduced to one dimension. As expected in the case of weak-field seeking molecules, the dashed black line in figure 4.12 a) shows that $\tilde{F}_X$ is indeed a force restoring the molecule towards the beam axis. As a result, molecules undergo transverse oscillations through the decelerator. Figure 4.12 b) shows this averaged force in comparison to the averaged force calculated using FEMLAB's numerical electric field strength map (red dashed line), where good agreement is found.

DC guiding

We first consider the case when all deceleration stages are left on throughout the experimental cycle. Oscillations in the transverse direction occur, which can be represented by contours of constant energy in phase-space. Separatrices denoting the region of phase space transported by

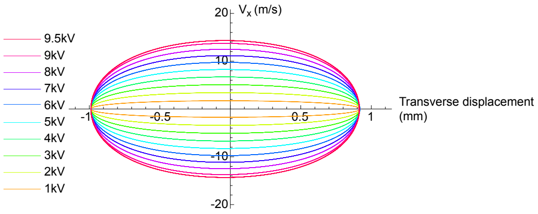

Figure 4.13: Separatrices in phase space for various voltages applied on the decelerator. The molecule will oscillate in the 1-D potential created by the average force $\tilde{F}_X$. The maximum possible oscillation amplitude is defined by the physical aperture of the decelerator.

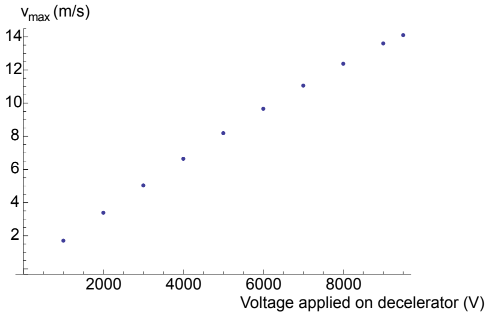

Figure 4.14: Maximum accepted velocity as a function of voltage applied onto the decelerator when the electric fields are left on during the entire experimental cycle (DC mode).

the decelerator can be plotted as shown in figure 4.13. The maximum amplitude is limited by the physical aperture of the decelerator, which is ±1mm. The separatrices plotted in figure 4.13 give the maximum accepted velocity $v_{\max}$ as a function of applied voltage, and this is plotted in figure 4.14. These predictions will be compared to data later in the chapter.

Guiding efficiency versus phase angle

To a first approximation, the force repelling the molecules from the electrodes can still be described as an average force $\tilde{F}_X$. However, by switching the fields, the longitudinally phase-stable molecules spend less time in the regions where the field is strong. Also, the electric field map W is different

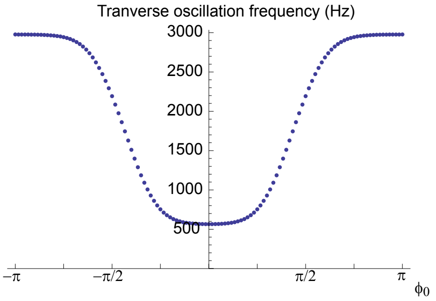

Figure 4.15: Transverse oscillation frequency as a function of ϕ_0 when decelerator is charged to ±10kV.

to the DC case, as every second stage is grounded. The result is that the average force is lower, resulting in less focussing. For instance, if $\phi_0 = \pi/2$ the fields are switched off for the entire time the molecule is exiting the stage. $\tilde{F}_X$ must then be roughly half of the DC case. $\tilde{F}_X$ is reduced further as less deceleration is applied. The transverse force $\tilde{F}$ in the switched case is given by

$$\tilde{F}_X = \frac{1}{2L}\left\{\int_{\phi_0-\pi}^{\phi_0} F_{\mathcal{X}}(\theta)\, d\theta + \int_{\phi_0}^{\phi_0+\pi} F_{\mathcal{Y}}(\theta)\, d\theta\right\}, \tag{4.29}$$

where $F_{\mathcal{X}}$ and $F_{\mathcal{Y}}$ are the force components along one of the transverse directions when the decelerator is in switch states $\mathcal{X}$ and $\mathcal{Y}$. However, because $F_{\mathcal{Y}}(\theta) = F_{\mathcal{X}}(\theta - \pi)$, Eq.(4.29) reduces to

$$\tilde{F}_X = \frac{1}{L}\int_{\phi_0-\pi}^{\phi_0} F_{\mathcal{X}}(\theta)\, d\theta. \tag{4.30}$$

Figure 4.15 shows the transverse oscillation frequency as a function of ϕ_0 when the decelerator is charged to ±10kV. In order to obtain this figure, $W(X)$ was extracted for different values of Z using the electric field strength map from FEMLAB (a few are shown as red dashed lines in figure 4.11). A harmonic potential, $(1/2)kX^2$, was fit to $W(X)$ at each value of Z, yielding force constants k as a function of Z. Following Eq.(4.30), an average force constant $\tilde{k}$ was found for each value of ϕ_0, from which the frequency was extracted by using the relation $\tilde{k} = m(2\pi f)^2$. A lower ϕ_0 reduces the oscillation frequency and the transverse acceptance of the decelerator. This reduced transverse acceptance will be observed in the data shown in section 4.4. Note that this only applies to molecules which are phase stable. The molecules which are not bound to the longitudinal potential well will see fields switched at uncorrelated times, which affects the transverse guiding differently.

The transverse oscillatory motion can also parametrically couple to the longitudinal motion [143]. The result is that the acceptance is reduced at low ϕ_0, while increased slightly at higher ϕ_0 when compared to the 'uncoupled' model.

4.3 The experimental setup

4.3.1 The decelerator

A schematic of the Stark decelerator is shown in figure 4.16. The decelerator comprises 100 pairs of 3mm diameter electrodes made of mechanically polished 316L stainless steel. An electrode pair, when aligned as shown in figure 4.16, creates a potential hill in the molecular beam axis Z when voltage is applied. The transverse distance between electrodes is 2mm. In order to achieve focussing in both transverse directions, these pairs alternate in orientation between the X and Y axes as shown in figure 4.16. We define L as the centre-to-centre distance between pairs along Z, which is 6mm. The 200 electrodes are mounted on four 16mm diameter support rods, according to their polarity and orientation. Each rod electrically connects all electrodes of the same orientation and polarity (Horizontal positive/negative and vertical positive/negative). By applying the voltage onto the four rods holding the electrodes, only 4 independent 20kV switches are needed to operate the decelerator. The high voltage is provided by HV feedthroughs attached

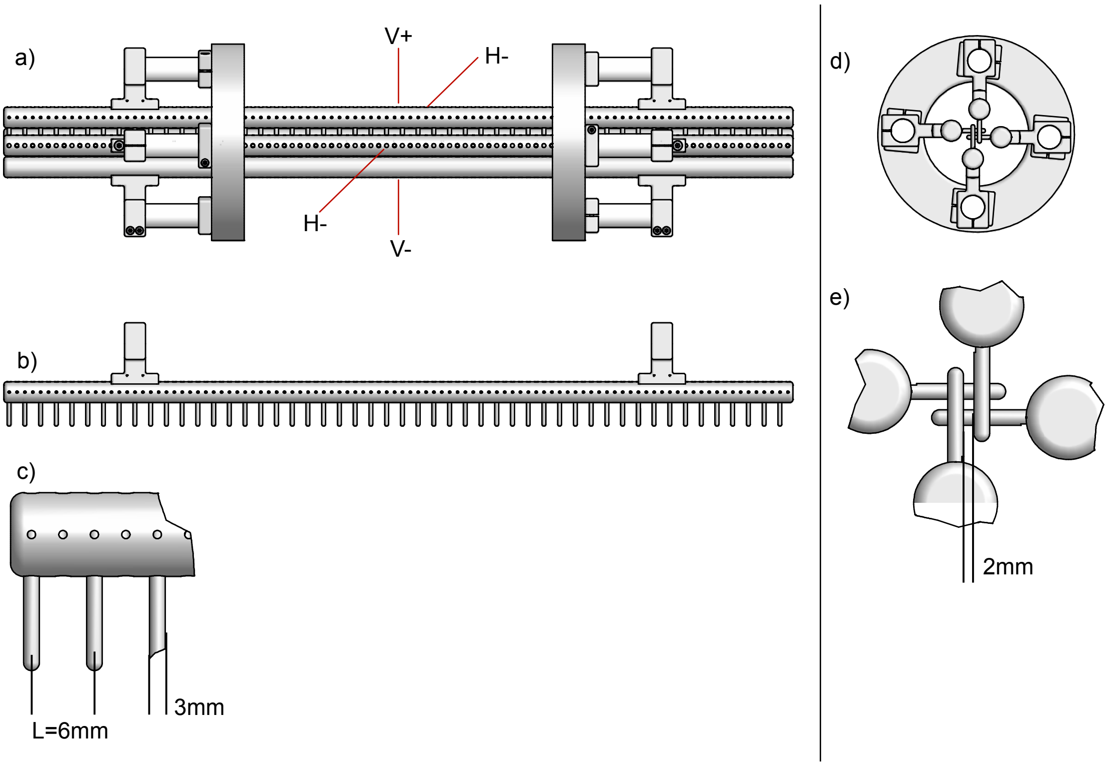

Figure 4.16: Side views of a) the entire decelerator b) one of the four rods that make up the decelerator c) magnified view of the end of a rod. Axial view of d) the entire decelerator and e) magnification of the central region.

to custom-made connectors. These connectors are designed to make electrical contact with the supporting rods by pushing into one of the outward-facing holes drilled in the surface of the rods.

As shown in figure 4.17, the 4 support rods holding the electrodes are in turn held by insulating alumina rods of diameter 18mm, which are attached to two large rings at either end of the decelerator. The large rings are designed to allow the entire structure to slide into a cradle, supported by translational feedthroughs. This allows the position of the decelerator to be adjusted. The cradle is designed such that the front of the decelerator (pointing towards the source) is positioned as close to the skimmer as possible to maximize the flux of molecules entering the decelerator.

4.3.2 Vacuum system

The vacuum chamber housing the decelerator is shown in figure 4.18. It is a 404mm long cylinder of radius 100mm with DN200CF flanges welded on both ends. When the full experiment is assembled, one end is connected to the source chamber while the other is connected to the detection chamber, as shown in figure 2.3. A total of 12 DN40CF flanges protrude from the cylinder. Translational feedthroughs are attached to 4 of them, as indicated in figure 4.18, which allow the position of the decelerator to be adjusted. Four more flanges are used for the high voltage feedthroughs. The top four are unused. The deceleration chamber is pumped out by the 1000l/s turbomolecular pump attached to the detection chamber.

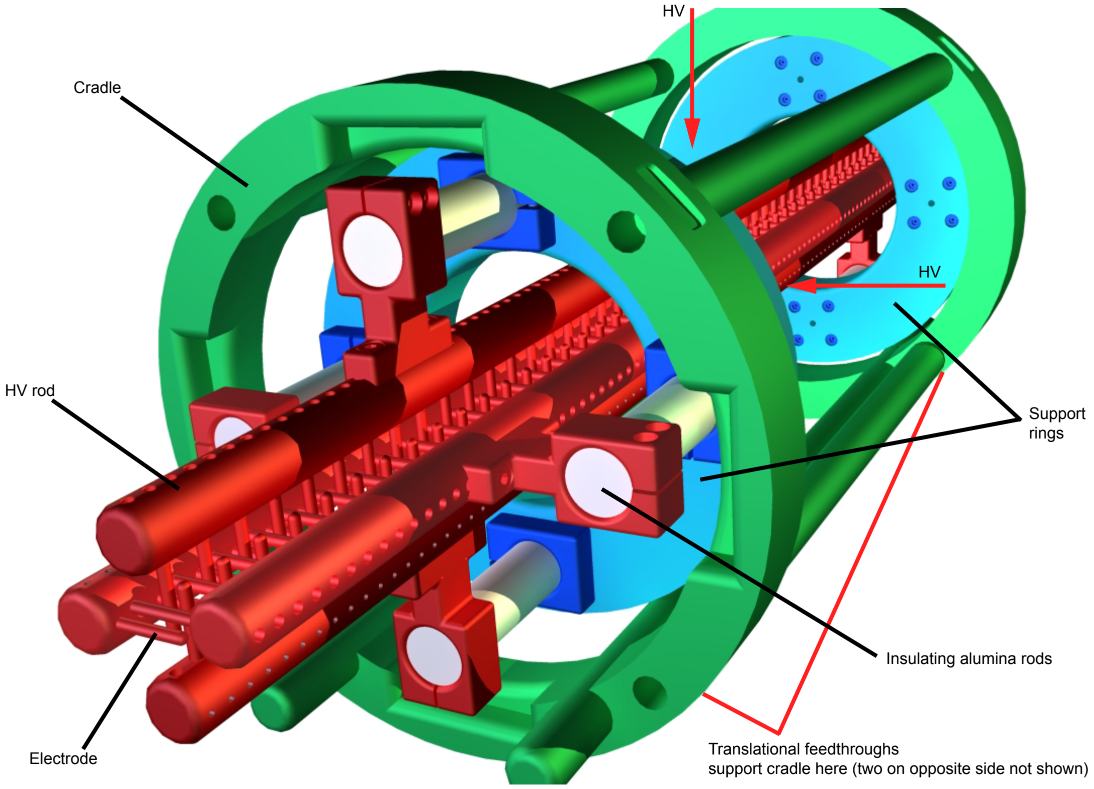

Figure 4.17: The decelerator sits inside a cradle which is supported by 4 translational feedthroughs allowing the position of the decelerator to be adjusted.

4.3.3 Providing the high voltage

An expanded block diagram of the experiment is shown in figure 4.19. In addition to controlling the source, detector and the microwave frequency, the computer also controls the switching sequence of the decelerator. Following the production of the LiH molecules, the decelerator is operated by applying a sequence of high voltage pulses onto its electrodes. Figure 4.19 also shows how this is achieved. DC high voltage is provided by the two power supplies. These are connected to switches which apply the voltage on the electrodes when the appropriate signal is received from the computer. The TTL from the computer is sent down an optical fibre, then sent to 50Ω drivers as required for the switches. The fibre significantly reduces pick-up noise, but also protects the computer from any possible voltage spikes in the event of a switch failure.

A circuit diagram showing the high voltage components of the decelerator is shown in figure 4.20. DC high voltage supplies, along with 20kV 0.5μF capacitors are connected to 20kV switches (BEHLKE HTS-201-03-GSM-HBF-CF). The two large capacitors are added to the circuit to ensure that enough charge is available for the duration of the deceleration sequence, so minimizing the voltage drop between the first and the last pulses of the deceleration sequence. The switches, triggered from the computer, connect the decelerator to either the HV supply or ground. Figure 4.20 shows the horizontal electrodes being grounded, while the vertical ones are connected to the high voltage supply. Following the notation used in section 4.2.2, this would correspond to state $\mathcal{X}$. The 100Ω, 1.1kΩ and 1.2kΩ are current limiting resistors, chosen to give the desired rise/fall times when the switch is thrown. Experimentally, these times were found to be around 3 times

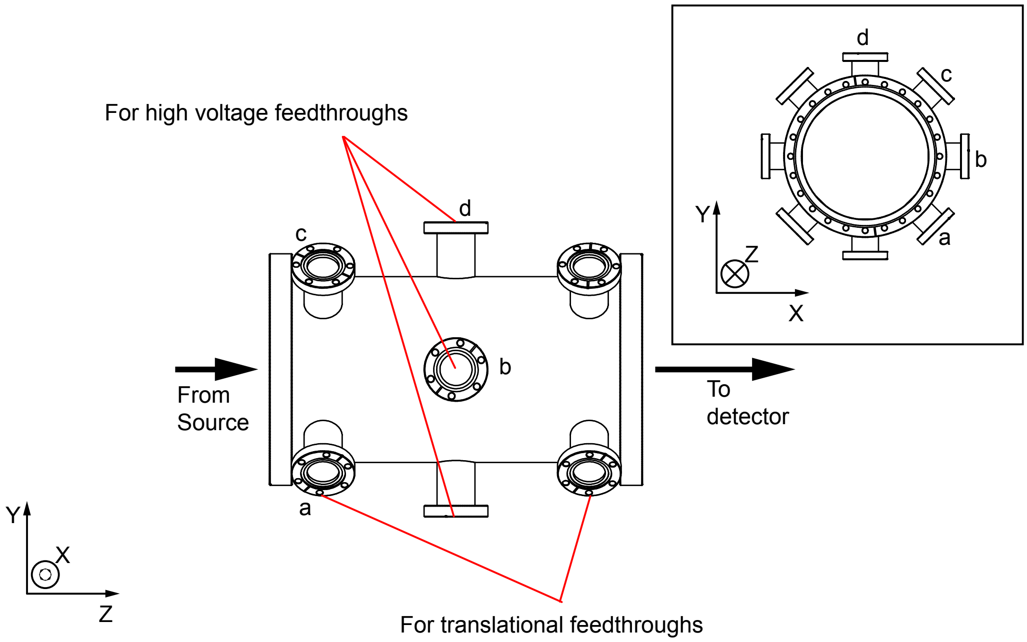

Figure 4.18: Layout of the deceleration chamber. Inset shows the chamber when looking down the molecular beamline.

longer than intended. We believe this is due to the capacitance caused by the extra shielding on the current-carrying wires (see following section). The 47kΩ resistors smooth out the charging of the capacitors between the HV bursts.

An expanded event-chain diagram showing the timing sequence is shown in figure 4.21. A few hundred μs after the Q-switch is fired, depending on the molecular pulse velocity, the deceleration sequence is started. This train of TTL pulses determine when the voltage is applied/removed from the decelerator. Following section 4.2.2, a timing sequence is calculated that decelerates the synchronous molecule at a chosen phase angle such that the fields are shut off when the molecules arrive at the same position on the potential hill.

4.3.4 High voltage conditioning and noise reduction

High voltage conditioning

A critical aspect of the experiment is to be able to switch the high voltage on and off very quickly. The high voltage circuit is therefore designed to have very low resistance and capacitance. As the circuit diagram in figure 4.20 shows, the current is limited only by a few kΩ. Were any electrical discharge to occur between the electrodes, the entire charge stored in the capacitors would rapidly be released onto the circuit. At ±10kV, peak currents reach several amps, causing severe damage to the electrodes. In order to ensure that such discharges do not occur, a procedure called 'high voltage conditioning' is performed. The electrical setup is then slightly different to the operational mode and is shown in figure 4.22.

The capacitors have been removed, and 1GΩ resistors are put in series in order to limit the currents to around 10μA. The switches are also removed. Instead, a pair of home-made floating ammeters are used to monitor current flow in the circuit. When a DC voltage is applied, there should be no

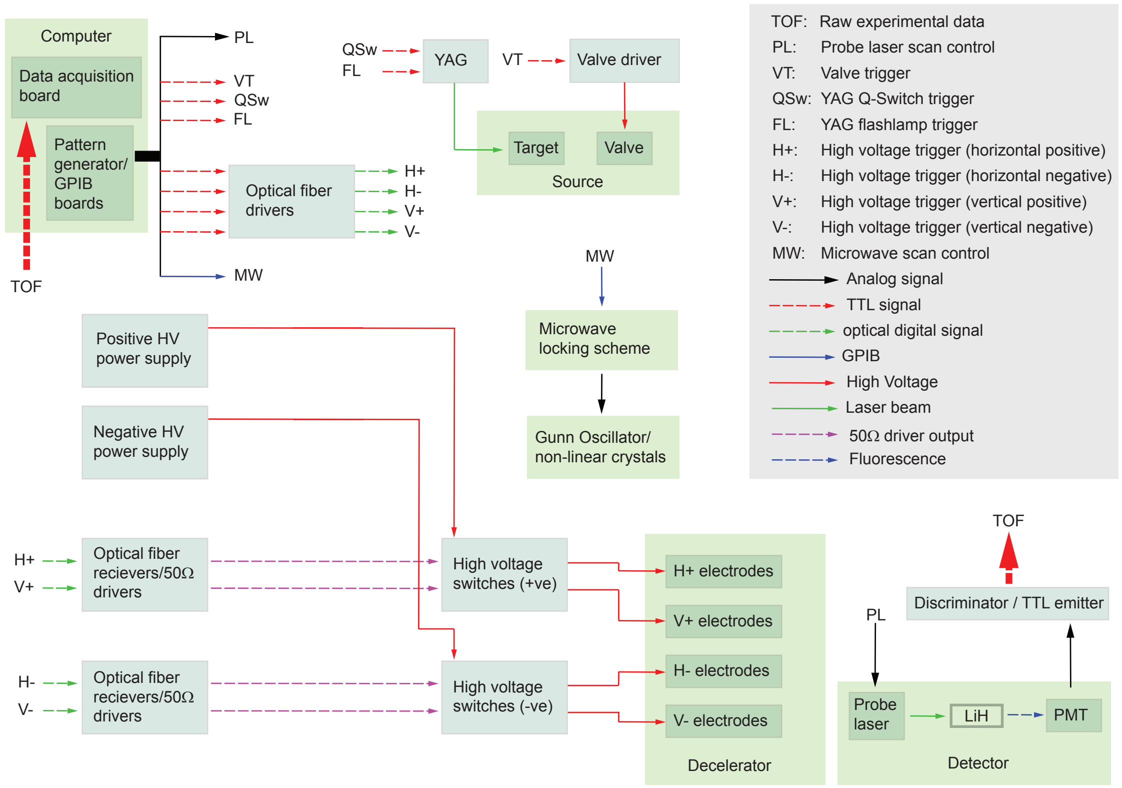

Figure 4.19: Block diagram showing the elements of the experiment, the control and acquisition systems.

current flow, apart from an initial transient corresponding to the charging of the electrodes. The decelerator is then kept at the constant voltage for several minutes, to ensure that no breakdowns occur. Once confident that the electrodes do not have any breakdowns, the voltage is slightly increased. This procedure is repeated until the desired voltage is reached. The accepted wisdom is to condition to a voltage which is 20% higher than the desired operational voltage. In order to operate at ±10kV, the decelerator was conditioned to ±12kV.

However, if electrical discharge does occur, the voltage must be reduced in order to stop the flow of current. High voltage conditioning is something of a black art. Small currents can be beneficial for the electrodes, as they tend to smooth out any irregularities on the surface. Letting ≈100nA of

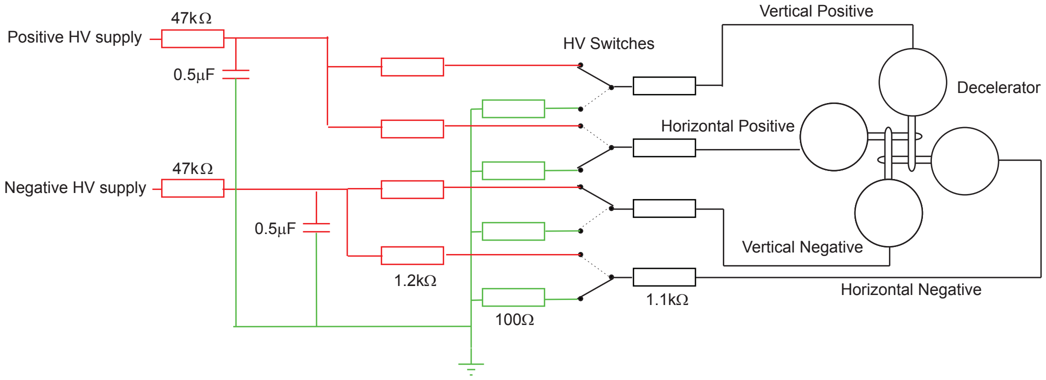

Figure 4.20: Circuit diagram of the high voltage components of the decelerator.

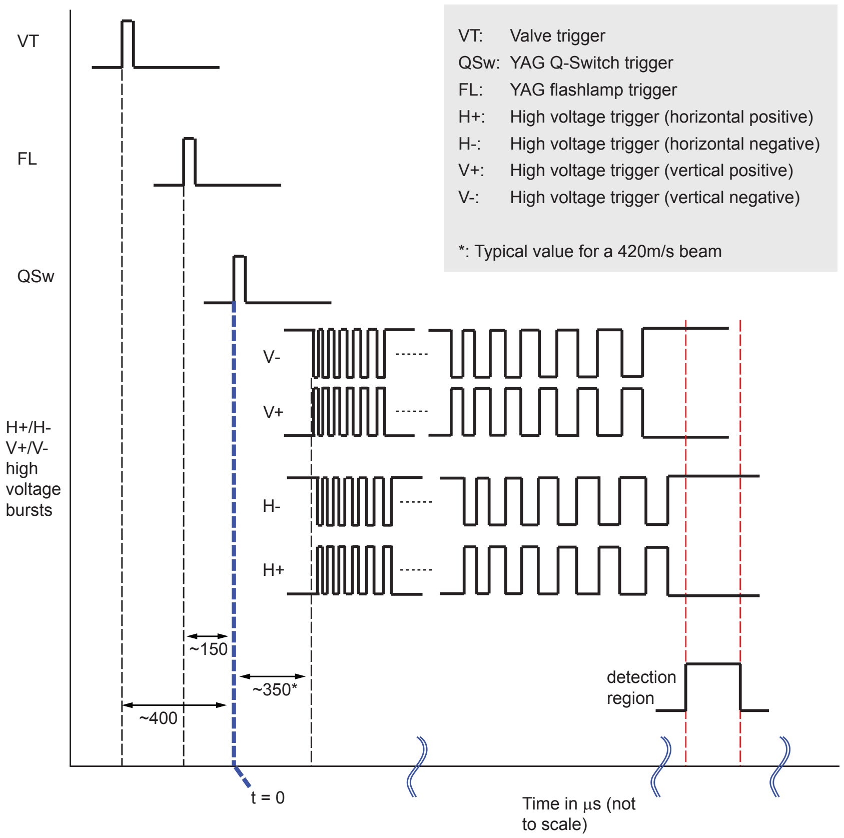

Figure 4.21: Event-chain diagram of one experimental cycle.

current flow for a few minutes sometimes quenches the discharge completely, allowing the voltage to be increased further. Other times, the current flow simply increases as the surface deteriorates, forcing the experimenter to reduce the voltage in order to prevent serious damage. If a large spike occurs while conditioning, a further step called ‘gas conditioning’ must be set up. This follows the same principle as normal vacuum conditioning, except 10^{-4}-10^{-5}mbar of argon is leaked into the vacuum chamber. Any discharge ionizes the gas, and these ions are then accelerated onto the electrodes where they tend to smooth away the surface irregularities. Just as with the electrons in vacuum conditioning, the ions quench the discharge.

In our experiment, we experienced a very large current spike at around 14kV on our first day of conditioning. Although there was no visible damage to any of the electrodes, only after several days of vacuum and gas conditioning were we able to bring the voltage back up to 7kV (enabling operation at 5kV). Over a period of 6 months, we intermittently returned to conditioning. The operating voltage was thus slowly increased to 10kV.

Note that whenever the vacuum chamber is opened, it is recommended to do some conditioning in case any dirt landed on the electrodes.

Noise reduction

Once the desired voltage is reached with the DC conditioning circuit (figure 4.22), the circuit in figure 4.20 is installed. While switching, the voltage is slowly increased. The peak currents flowing through the circuit are above 1A. At these currents, radio frequency broadcast from wires as well

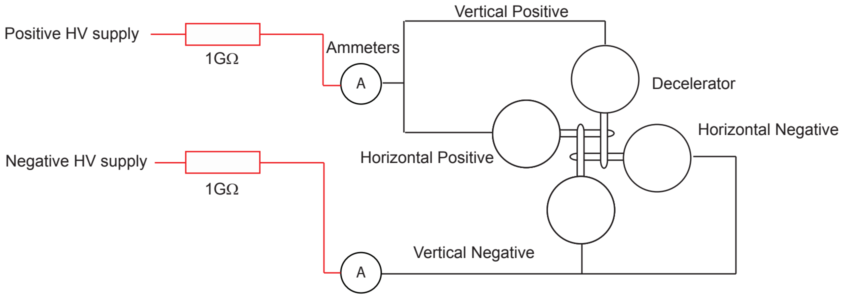

Figure 4.22: Circuit diagram for the high voltage circuit when conditioning

as ground noise become significant enough to unlock lasers. Care must be taken to ensure that this RF does not affect other electrical equipment, and that ground loops are minimized. This shielding step is also a black art. The main sources of broadcast, the wires connecting the electrodes and the switches, were isolated using EMI screening conduit (a commercial flexible steel conduit designed to shield its contents from external EM-interference). 7cm diameter steel cylinders were used to cover the high voltage feedthroughs (often the cause of RF broadcast). These cylinders were attached to the DN40CF flanges of the HV feedthroughs, protruding outward so as to cover the air-side of the feedthroughs completely. The HV wires were connected to the feedthroughs through a 16mm hole in the side of the cylinder onto which the EMI-screening conduits are attached. A lid placed on the end of the cylinders ensured that the feedthroughs are sealed, preventing any airborne RF broadcast. To prevent any electrical breakdown to the steel cylinders, another insulating cylinder was placed between the feedthrough and the steel cylinders.

To prevent pick-up, the trigger signals from the computer were sent via optical fibres. The worst case scenario is that the switches trigger off each other (e.g. the horizontal negative switch causes enough noise on the trigger line of the vertical positive to trigger it). This behaviour can be monitored by probing on the HV feedthrough pin using a fast HV probe (Tektronix P6015A) and an oscilloscope. False triggering appears on the scope as small glitches, usually immediately before or after a switch is thrown. This effect must be suppressed through trial and error, the use of steel braid shielding and lots of aluminium foil. It was found that ground noise was minimized when all the grounds are connected to a single point situated as close as possible to the high voltage supplies. Finally, the PMT's output cable was buried in braid and aluminium foil to prevent false counts being registered by the PMT.

According to its instruction manual, the Gunn oscillator is very sensitive to static. To protect the device, it was placed inside a Faraday cage made of stainless steel perforated sheets bent into the shape of a box. The output frequency of the Gunn oscillator fluctuated depending on where the cage was grounded to. We found through trial and error that the microwave frequency was most stable when the cage is grounded to the vacuum chamber.

We found that the HV pulses also resulted in a shift of the Ti:Sapphire laser frequency. By sending the Ti:Sapphire laser beam through a 250MHz low finesse cavity, the frequency over a laser scan was monitored. Figure 4.23 a) shows the laser intensity detected through the cavity. This signal is integrated over the normal gating period of our detector, 1 to 1.5ms after the Q-Switch.

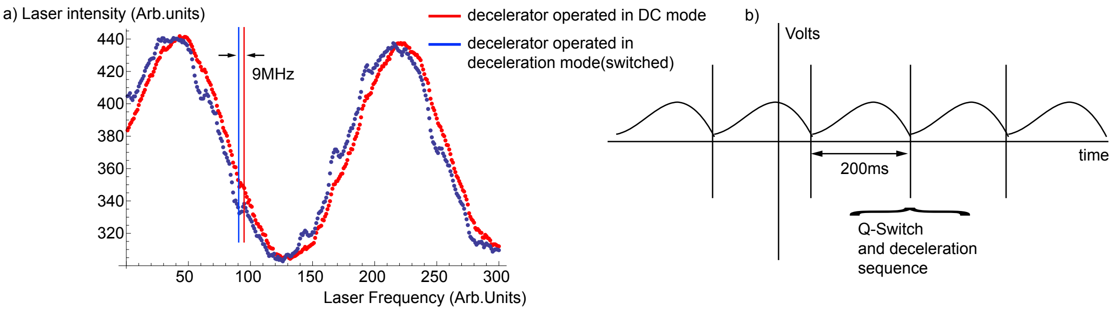

Figure 4.23: a) Output intensity from a low finesse 250MHz cavity, measured 1ms after the Q-switch for 500μs. By scanning the Ti:Sapphire laser through 500MHz, cavity fringes are observed. A frequency shift relative to DC mode of around 9MHz is observed whenever the decelerator is switched. b) Illustration of the temporal variation of cavity output observed on an oscilloscope, when the laser is nominally locked.

As the Ti:Sapphire laser is scanned, fringes are observed. The experiment alternates between DC guiding and deceleration, which is reproduced here. The blue points show the intensity for the DC mode, while the red points show the frequency when the decelerator is switched. A 9MHz shift is consistently observed whenever the decelerator is switched. By nominally locking the laser at a particular frequency and plotting the cavity output on an oscilloscope, we see that the laser frequency varies periodically with the repetition rate of the deceleration sequence (5Hz) as is illustrated in figure 4.23 b). The full oscillation amplitude is of the order of 100MHz, although this was not measured exactly. We believe this frequency shift to be due to noise on the ground line of the locking circuit. The ground noise caused by the switching of the decelerator causes the error signal to fluctuate, and the locking mechanism attempts to compensate for the fictional shift, sending the laser frequency off its initial position. A better electrical connection between the laser head and the controller, along with several additional grounding connections minimized this problem to within the natural linewidth of the molecules.

Once all triggers function without glitching and all other electrical equipment is sufficiently shielded to operate correctly, the molecules are ready to be decelerated.

The HV pulses

The high voltage pulses applied to the decelerator can be viewed on an oscilloscope by using a fast HV probe (Tektronix P6015A). Figure 4.24 a) illustrates the first two pulses observed on the vertical pair of electrodes. Characteristic rise and fall times are 1μs and 500ns respectively. Figure 4.24 b) illustrates the entire train of pulses, showing a small drop in the voltage over the HV pulse train. The capacitors (see figure 4.20) are gradually depleted of their charge over the deceleration sequence. By the end of the sequence, the capacitors are no longer able to supply the same voltage as they did at the start, resulting in the dip. Throughout the experiment, the switching sequence is calculated for a voltage which is slightly lower than the rated applied DC voltage. This way, although the calculated ΔW per stage is slightly too low at the start of the sequence and slightly too high at the end, the deceleration mechanism still works as will be shown in the following

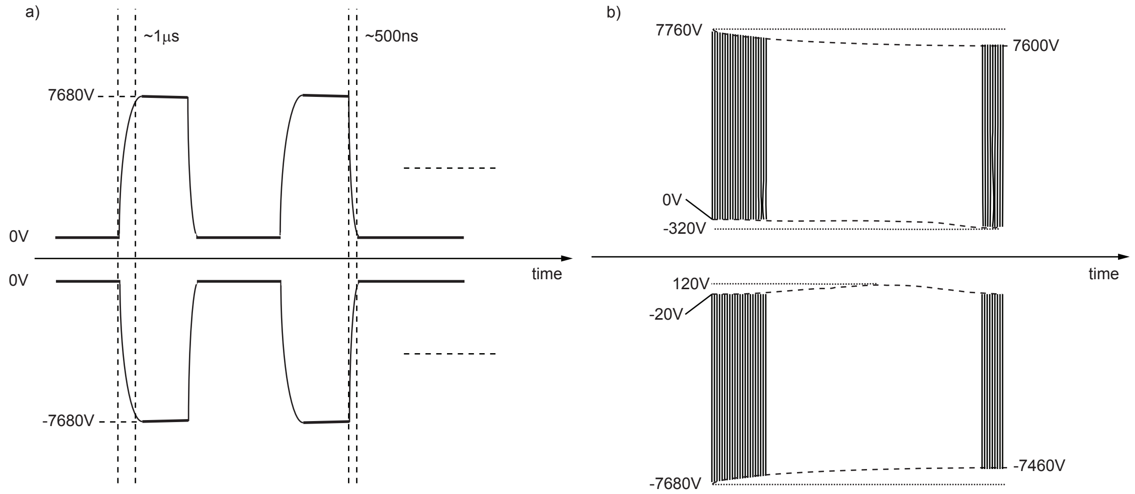

Figure 4.24: Illustrations of HV pulses applied to the two vertical electrodes as observed on an oscilloscope. a) the first two pulses and b) the entire pulse train.

sections.

4.4 The experimental data

4.4.1 Fluorescence signal versus applied voltage

By leaving the fields on during the entire transit time of the molecule, the effect of transverse guiding can be investigated. This will be referred to as the DC mode of operation, as the decelerator applies a constant voltage. When no field is present (the decelerator is switched off throughout the cycle), there is obviously no focussing. Only the molecules with very low initial transverse velocities exit the decelerator without crashing into the electrodes. There are so few molecules in this case that we do not observe any signal. As voltage is applied onto the electrodes, more of the molecules are successfully guided though, resulting in an increase in signal. Figure 4.25 shows the size of the transmitted signal as a function of applied voltage. Figure 4.25 a) is the data from an argon-carried beam (600m/s), while b) is the data for a krypton-carried one (430m/s). For a fixed probe laser frequency, molecules with larger transverse speeds are Doppler shifted out of resonance and so are not detected as efficiently as the on-axis molecules. To ensure that all molecules are detected, irrespective of velocity, the probe laser was scanned over the $X^1\Sigma^+$ ($v'' = 0, J'' = 1$)-$A^1\Sigma^+$ ($v' = 4, J' = 2$) resonance in taking this data. The signal size was then obtained by integrating over the frequency scan. The results are the black points in figure 4.25. In order to minimize errors due to source fluctuations, the data points were normalized against the average of the signals at a voltage of 8kV recorded immediately before and after a measurement. This can the be compared to the predictions obtained from numerical simulations of the experiment. The data is in very good agreement with the predicted behaviour.

The spectral width of the excitation transition is shown in figure 4.26. Points from an argon-carried beam are shown in a), while points from a krypton-carried beam are shown in b). The

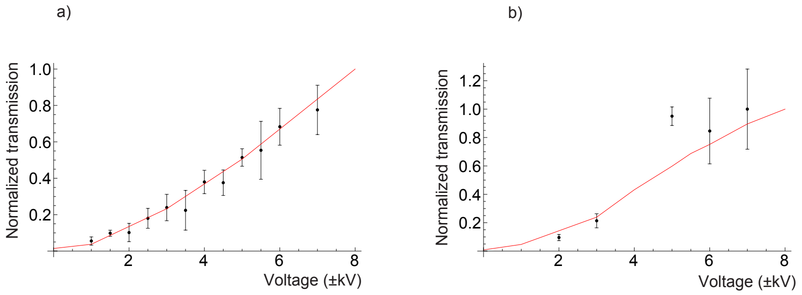

Figure 4.25: Total LiH ($J = 1$) transmission through the decelerator for a) 600m/s beam b) 430m/s beam as a function of voltage applied to the decelerator. The red curves are the predicted results of the simulation.

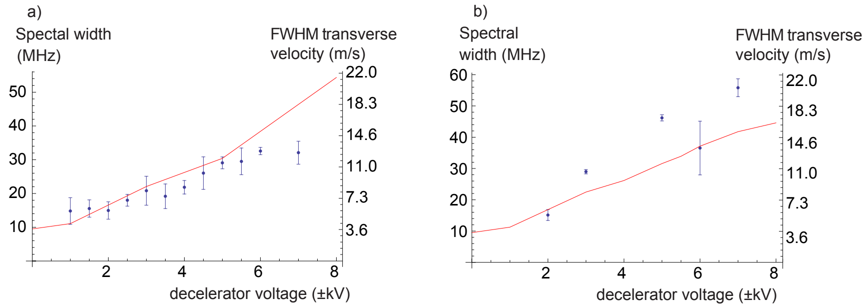

Figure 4.26: Spectral width of the excitation transition signal and corresponding transverse velocity from an a) 600m/s beam b) 430m/s beam as a function of voltage applied to the decelerator. The red curves show the predicted results of the simulation.

red lines represent the widths as predicted from numerical simulations of the experiment. The simulator numerically solves the equations of motion for an initial distribution of positions and velocities (see section 4.4.2). The data, which agrees reasonably well with the simulations, shows that the spectral width of the molecular pulse exiting the decelerator increases as the voltage is increased, as expected. This increased spectral width is a result of molecules with higher initial velocities being successfully guided through the decelerator. The spectral width can therefore be used to find the transverse velocity accepted by the decelerator. The velocity axis has been shown on the RHS of each plot in figure 4.26. In order to obtain the red curve from the simulations, the transverse velocity distributions predicted by the simulator were converted to a Doppler width, with which a convolution of the natural linewidth was taken. We find good agreement. We believe the fluctuations of the krypton data mainly come from source instability. Note also that the data is in good agreement with predictions from the 1-D model for an average F_x discussed in section 4.2.2.

From figures 4.25 and 4.26, we conclude that higher voltages yield more signal because transverse focussing improves, as expected. This is due to a higher transverse acceptance, as demonstrated by the increase in spectral width of the beam exiting the decelerator.

4.4.2 Decelerating a beam of lithium hydride molecules

We now arrive at the main dataset. In this section, the deceleration of lithium hydride molecules will be demonstrated.

A typical time-of-flight dataset

A typical time-of-flight dataset obtained from our detector is shown in figure 4.27 a). The blue curve shows the TOF when the decelerator is switching, while the red curve shows the TOF when the voltage is left on throughout the experimental cycle. The experiment was set up such that every second shot was taken in DC mode. Each curve is an average of 1000 shots. At a repetition rate of 10Hz, the data took approximately 3.5 minutes to collect. For this dataset, Ar was used as the carrier gas, giving an initial velocity of approximately 600m/s. The switch timings for this dataset were calculated for an initial velocity of 585m/s and a phase angle ϕ_0 of 45°. The applied voltage was 8kV. Without switching the decelerator (red curve in figure 4.27), we obtain a familiar $\approx$100μs long pulse, similar to those shown in chapter 2. When the decelerator is switched, the molecules travelling at approximately 585m/s will be caught in the potential well and decelerated. These molecules arrive later, as shown by the blue curve. The very sharp peak observed at around 1400μs is the decelerated pulse. Signals corresponding to molecules which travelled through the decelerator without being decelerated are also observed on the blue curve. These molecules did not have the correct initial position in phase space to be caught in the decelerating well. All other molecules either crashed into the electrodes, or followed trajectories which did not lead them to the detector.

By taking the integral over Gaussian fits of the red curve and the decelerated peak on the blue curve of figure 4.27 a), we find that approximately 1.6% of the molecules in the original pulse were decelerated when operating at 8kV at a phase angle of 45°. The expected arrival time can be calculated by summing the various transit times (source to decelerator, through the decelerator and decelerator to detector). For the parameters used to obtain figure 4.27 a), this expected arrival time is 1412μs. The peak of the decelerated pulse is found to be at 1412$\pm$1μs, which is in very good agreement with the prediction. Using Eq.(4.12), we therefore conclude that the velocity of the decelerated pulse is 521m/s, corresponding to a 11% reduction in the lab frame velocity of the molecules.

Comparison with numerical simulations

Our in-house simulator written by M. R. Tarbutt numerically calculates trajectories for molecules. Once a phase space distribution at the source and the various operational parameters of the decelerator are specified, the simulator can generate TOFs which can be compared to the experimental data. The arrival times of the molecules are binned to approximate the detector's resolution. The black curve in figure 4.27 b) shows the simulated TOF calculated by solving the equation of motion for 10^5 initial phase space positions mimicking a Gaussian 'pulse' of molecules travelling at 600m/s. The spatial spread at the source was set to 5mm width along Z and 3mm along X and Y. The velocity spread was set to 30m/s along Z and 15m/s along X and Y. The simulator then generates

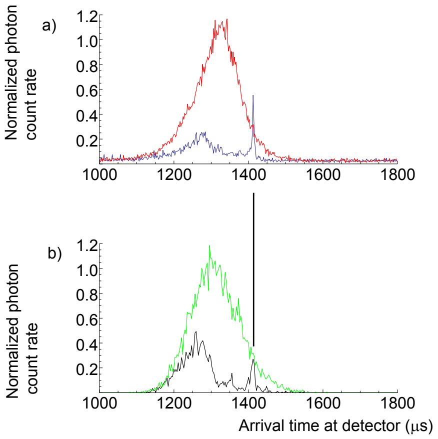

Figure 4.27: a) Typical time-of-flight (TOF) dataset obtained from the experiment. The blue curve shows the TOF when the decelerator is switching, while the red curve shows the TOF when the voltage is left on throughout the experimental cycle. b) Simulated TOF obtained by numerically solving for the trajectories of the molecules. The green curve shows the simulated arrival times when the decelerator is not switching, while the black curve shows the result of simulating the switching case.

a Gaussian distribution of initial positions and velocities for which the equations of motion can be solved. The decelerator's experimental parameters used to obtain figure 4.27 a) were replicated for this simulation. According to the simulator, the arrival time of the decelerated pulse is 1411.9μs, which agrees with other calculations and the data. Using the electric field map calculated using Femlab for the DC case, simulations of DC guiding can also be obtained, as shown by the green curve in 4.27 b). Here, the prediction for the fraction of decelerated molecules with respect to the original pulse is 1.7%, which is also in good agreement with the experiment.

However, there is a discrepancy between the number of undecelerated molecules observed in the experiment and the number predicted by the simulation. Comparing the total output of the switching case to the DC case, the data shows that only 18% make it to the detector, instead of the calculated 25%. Although this is not completely understood, we suspect the loss comes from a change of internal state from $m_J = 0$ to the high-field seeking $m_J = \pm 1$ states. The molecules which are not caught in the longitudinal potential well may be in a region of very low electric field when the field is switched, unlike the phase-stable ones which are always in a fairly large electric field when the field is switched. While they travel through regions where the field is absent, the m_J states are nearly degenerate. If the fields are switched on while the molecules are in these regions of low field, it may be possible to drive transitions to strong-field seeking states. The simulation does not account for this loss.

Delay to deceleration

The number of molecules caught in the phase stable region depends on the overlap between the phase space density of the original pulse and the decelerator's acceptance at the start of the deceleration sequence. Because the velocity is strongly correlated with the arrival time at the

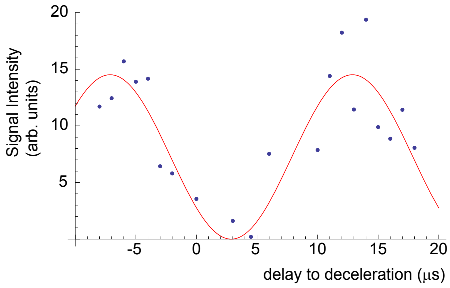

Figure 4.28: Signal intensity of the decelerated peak versus delay-to-deceleration when operating at 8kV with $\phi_0 = 45°$ for an initial velocity of 595m/s. The molecules suitable for deceleration have the best overlap with the phase-space acceptance of the decelerator when the delay-to-deceleration parameter is set to around -6μs.

decelerator, the timing for the start of the deceleration sequence is critical. By changing the start time of the deceleration sequence (a parameter I will refer to as the delay-to-deceleration), the overlap between the decelerator's acceptance and the molecular pulse can be varied. A delay to deceleration of zero implies that the sequence starts at time $\mathcal{L}/v_i$, where v_i is the initial velocity of the synchronous molecule and $\mathcal{L}$ is the distance from the source to the decelerator. Figure 4.28 shows the amplitude of the decelerated pulse as a function of the delay-to-deceleration. The decelerator was operating at ±8kV with a switching sequence calculated for an initial velocity of 595m/s and $\phi_0 = 45°$. In order to maximize the signal, the deceleration sequence must be started when the molecules with the correct velocity (595m/s) reach the front of the decelerator. If the sequence is started at the wrong time, the signal vanishes because there are no molecules with the correct velocity present at the entrance of the decelerator when the switching sequence started. Figure 4.28 also shows a periodic behaviour. This is because the decelerator, through its periodicity, produces a series of travelling potential wells. If the deceleration sequence is started an entire switch period late, molecules can be trapped upon arriving at the second stage of the same orientation, having flown past the first two undecelerated. Alternatively, starting the sequence early can allow molecules to be caught at the first stage, but on a subsequent decelerator switch. Although molecules decelerated using 98 stages will arrive at the detector at slightly different times, this difference is only a few μs. For these experimental parameters, this is below our detector's resolution. The period of the intensity oscillation in figure 4.28 is 20.0μs. This is in good agreement with the 20.1μs time interval between two switches (of electrodes with the same orientation). Alternatively, a molecule travelling at 595m/s covers 11.9mm during that time, which is consistent with the 12mm spacing between two stages of the same orientation. Either way, the intensity of the decelerated peak is maximized when a delay of either -6μs or +14μs is introduced. We believe the shift from zero mostly comes from spatial and temporal uncertainties in the source. Additionally, our uncertainty on the decelerator's position along the beam axis is about 1mm, which may also contribute to the shift.

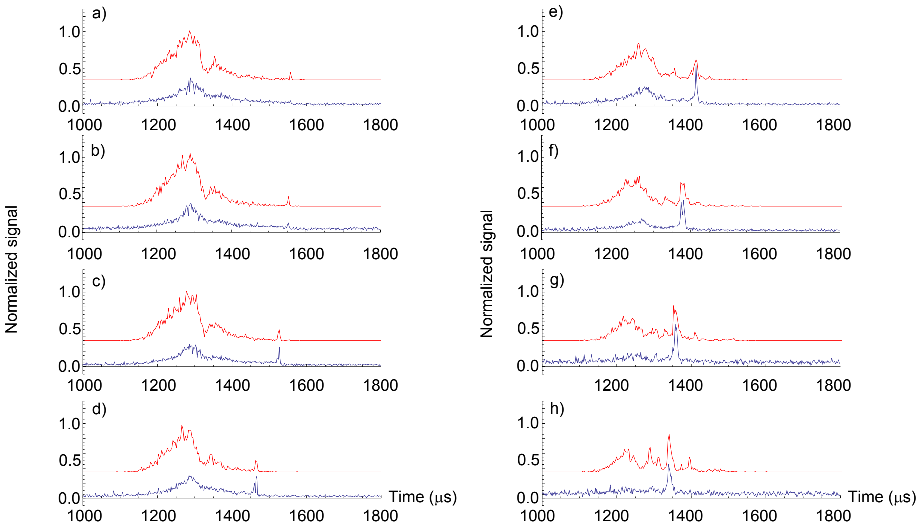

Figure 4.29: Experimental data (blue) and simulations (red) showing the Stark deceleration of lithium hydride molecules from 585m/s to a) 413m/s ($\phi_0 = 87°$), b) 416m/s ($\phi_0 = 84°$), c) 434m/s ($\phi_0 = 75°$), d) 480m/s ($\phi_0 = 60°$), e) 521m/s ($\phi_0 = 45°$), f) 550m/s ($\phi_0 = 30°$), g) 570m/s ($\phi_0 = 15°$), h) 585m/s ($\phi_0 = 0°$, guiding). The signal has been normalized to the amplitude of the DC TOF pulse.

The data

Injecting this beam into the Stark decelerator, operating at 7.6kV and switching according to times calculated using Eq.(4.13), we obtain time-of-flight profiles shown in figure 4.29. For most datasets in this section, the experiment alternated shot by shot between decelerating and DC modes of operation. The fast switching between the two modes allows the initial source parameters for a given deceleration TOF to be determined.

Figure 4.29 shows the Stark deceleration from an initial velocity of 585m/s using various values of ϕ_0. The blue curves show experimental TOFs while the red curves, offset along the vertical axis for clarity, show the simulations. The curves have been scaled to the DC mode amplitude (not shown) to cancel out any intensity fluctuations in the source. DC mode velocity and temperature were found on average to be 595m/s and 600mK[1]. As ϕ_0 is increased, a narrow bunch of molecules is selected out of the main group and shifted to later arrival times. The size of the decelerated group decreases as the degree of deceleration increases. This is because the longitudinal acceptance is smaller for larger values of ϕ_0 (see section 4.2.3). At the largest phase angle used (87°), the molecules are decelerated from 585m/s to 413m/s. The observed arrival times and the flux of decelerated molecules are in very good agreement with simulations. Signals from undecelerated molecules[2] do show some discrepancy in amplitude. The experimental signals for these undecelerated molecules are much smaller than expected. We believe these losses come from transitions being driven when molecules travel through regions of low electric field, as discussed above. However, the overall trend of increasing undecelerated flux with increasing phase angle

---

[1] Over the entire data run, these values varied between 0.51K and 0.66K, as well as 594.5m/s and 596.8m/s.

[2] molecules which reach the detector but are not phase-stable.

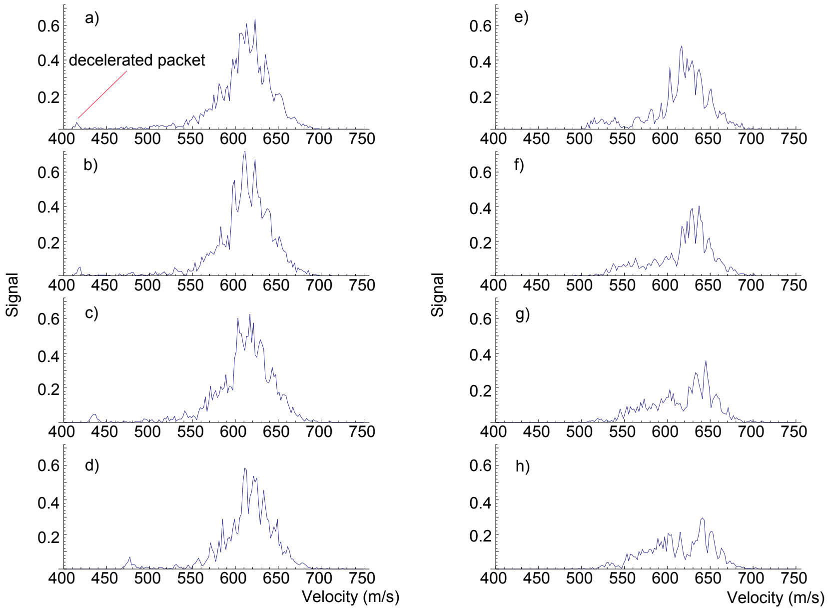

Figure 4.30: Velocity distributions obtained from simulation for an initial velocity of 585m/s to a final velocity of a) 413m/s ($\phi_0 = 87°$), b) 416m/s ($\phi_0 = 84°$), c) 434m/s ($\phi_0 = 75°$), d) 480m/s ($\phi_0 = 60°$), e) 521m/s ($\phi_0 = 45°$), f) 550m/s ($\phi_0 = 30°$), g) 570m/s ($\phi_0 = 15°$), h) 585m/s ($\phi_0 = 0°$, guiding).

is observed in both experiment and simulation. I believe this is caused by parametric coupling between transverse and longitudinal motions. This effect is observed in phase-stable molecules (see [143]) and is known to be more severe as ϕ_0 tends to zero. Establishing the precise effect of such couplings for undecelerated molecules would require further investigation.

The simulation can be used to extract information which would otherwise be difficult to measure. Figure 4.30 shows the velocity distributions of the molecules. As the phase angle ϕ_0 is increased, a small packet of lower velocity emerges. These are the decelerated molecules. Their final velocity is in excellent agreement with the predictions of Eq.(4.12).

By using Kr as the carrier gas, the initial velocity is reduced to 420m/s. Operating now at ±10kV DC (with a switch pattern calculated for 9.5kV, see section 4.3), and for various values of ϕ_0, we obtain another series of TOFs as shown in figure 4.31. The vertical axis was scaled to the amplitude of the DC TOFs, as before. The mean DC velocity and temperature over the entire dataset were 439m/s and 1.3K. These values did however fluctuate, ranging from 431m/s to 448m/s and 1.0K to 1.9K. As before, a small group of molecules is selected from the main bunch and is shifted to later arrival times. Again, increasing ϕ_0 increases the shift, corresponding to lower velocities. The size of the decelerated peak decreases with increasing ϕ_0, to the extent that at the lowest velocities obtained, the signal from decelerated molecules is only just above the noise. Here, the molecules have been decelerated from 420m/s to 53m/s, meaning 95% of the kinetic energy was removed. This demonstrates that it is possible to decelerate LiH molecules down to trappable velocities using a Stark decelerator.

In comparing experiment and simulation in figure 4.31, let us first focus on the decelerated molecules. The simulations predict the arrival times of these decelerated molecules very well, the

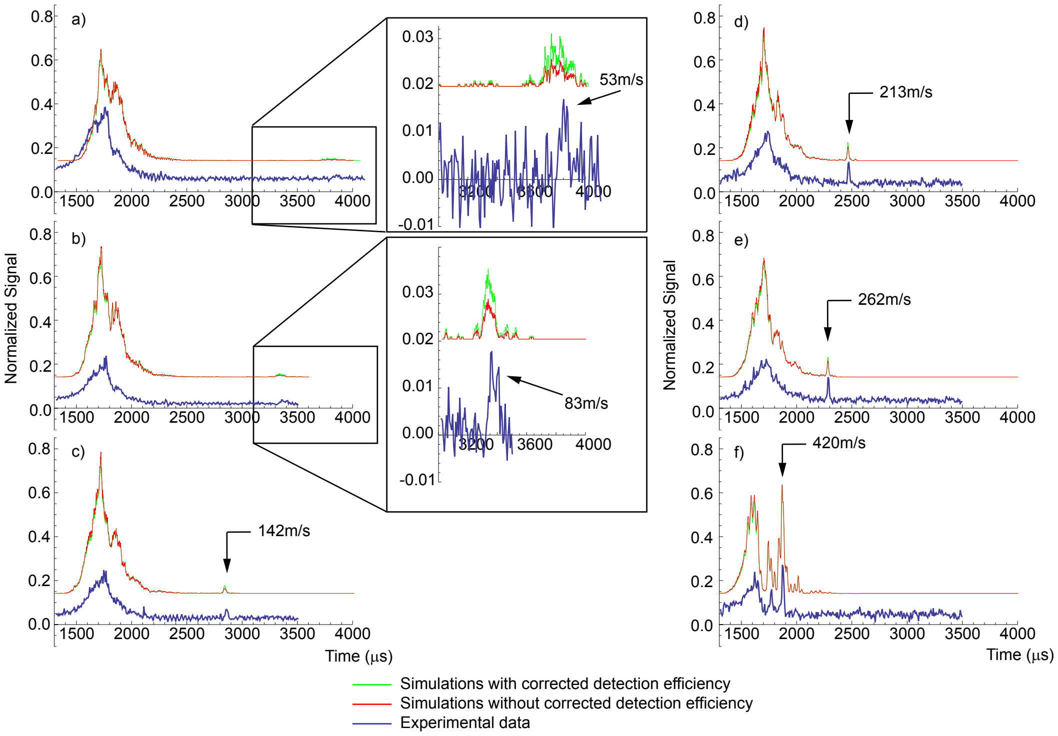

Figure 4.31: Stark deceleration of lithium hydride molecules, from 420m/s to a) 53m/s ($\phi_0 = 60.9°$), b) 83m/s ($\phi_0 = 60°$), c) 141.5m/s ($\phi_0 = 57°$), d) 213m/s ($\phi_0 = 51°$), e) 262m/s ($\phi_0 = 45°$), f) 420m/s ($\phi_0 = 0°$). The blue curve shows experimental data, while the red curve shows the simulation. The green curves are simulated TOFs after accounting for the velocity dependence of the detection efficiency. The signals have been normalized to the corresponding amplitudes in DC mode.

arrival times agreeing to within $\pm 50\mu$s in all cases. There is, however, a small systematic tendency for the molecules to arrive slightly later in the experiment than in the simulation, this being most noticeable at the lowest velocities obtained. This systematic shift is consistent with the detector being 2.5mm further downstream than the nominal value, and this is within the uncertainty of the detector placement. Another potential source of error is the 5% droop in the decelerator's voltage. The droop means that the molecules lose a slightly different amount of kinetic energy ΔW in comparison to the calculated value. The result is a longitudinal oscillation by the 'synchronous' molecule. The final velocity of the synchronous molecule can thus differ from the calculation by an amount set by the range of velocities which the synchronous molecule can take over the course of a longitudinal oscillation period. Therefore, the central arrival time may differ by an amount approximately equal to the spread in the arrival times. The amplitudes of the decelerated peaks tend to be a little larger in the experimental data than the simulations predict. This is mostly due to the velocity dependence of the detection efficiency. As discussed in section 2.7.2, not all molecules are excited during the interaction time with the detection laser given our laser power. Increasing the interaction time by reducing the velocity of the molecules therefore increases the signal by exciting a larger number of molecules. The green curves of figure 4.31 show the simulated

TOFs after accounting for this. Velocity dependant weights determined from the analysis given in section 2.7.2 were applied to the TOFs. At the lower velocities (figure 4.31 a) and b)) where this effect is greatest, the expected signal increases by a factor of 2, bringing the simulation far closer to the observed data.

The shape of the TOF profiles of the undecelerated molecules mostly agree, with the exception of 4.31 a), where the profile looks qualitatively different. The DC data (not shown) reveals that this is due to a non-Gaussian initial distribution of molecules from the source[3]. Also, just as in figure 4.29, some discrepancies in relative amplitudes are observed throughout the dataset. The most noticeable discrepancy is again for phase-unstable molecules. As mentioned in previous data, we believe this to be due to non-adiabatic transitions being driven when the decelerator switch occurs as the molecule is travelling through a region of low E-field.

Figure 4.32 shows the velocity distributions extracted from simulation. As before, a small packet of lower velocity emerges as ϕ_0 is increased. The final velocities of these decelerated packets are in good agreement with those predicted by Eq.(4.12). From these, the temperature of the decelerated peaks can be extracted, and are shown in figure 4.33. The temperature is obtained by equating a Gaussian fit of the velocity distribution of the decelerated peak to a Maxwell-Boltzmann distribution, giving:

$$N(v) \propto \mathrm{e}^{-\frac{m(v-v_0)^2}{2kT}} = \mathrm{e}^{-\frac{(v-v_0)^2}{w^2}}. \tag{4.31}$$

The fit's width w thus equals $\sqrt{2kT/M}$. The temperature is set by the phase-space acceptance of the decelerator. As such, the temperature decreases as the phase angle is increased. This is seen in figure 4.32 as a decrease in temperature with decreasing final velocity. For final velocities below 150m/s, the required change in ϕ_0 becomes small ($57^\circ \rightarrow 61^\circ$) and so no change in temperature of the decelerated peak is observed in these data points. At 53m/s, the temperature of the pulse is 15mK.

The flux of decelerated molecules as a function of ϕ_0 is shown in figure 4.34. The figure shows the decelerated flux obtained for initial velocities of a) 585m/s and b) 420m/s as determined from datasets shown in figures 4.29 and 4.31. The total signal from decelerated molecules, found by integrating over Gaussian fits of the phase-stable peaks were normalized to the total flux when operating in DC mode. Experimental data points are shown in red, while points extracted from simulations are shown in blue. Although already apparent from figures 4.29 and 4.31, we note that the decelerated flux is very low. At higher ϕ_0 in particular, the signal observed at the detector corresponds to less than a photon/shot. For a given phase angle, the v_i=585m/s data shows a higher flux. This is counter-intuitive as the voltage applied onto the decelerator was higher in b) v_i=420m/s, making the transverse acceptance higher. The principal cause lies in the difference in final velocities. In a), the molecules are still travelling at over 400m/s, whereas the molecules are as slow as 50m/s in b). After the deceleration process, the molecules travel through free-space for approximately 10cm. Since the transverse velocity of the pulse has not changed over the deceleration, fewer molecules reach the detector at the very lowest speeds. The divergence

---

[3] As a reminder: the simulator creates a Gaussian spatial and velocity distribution at the source.

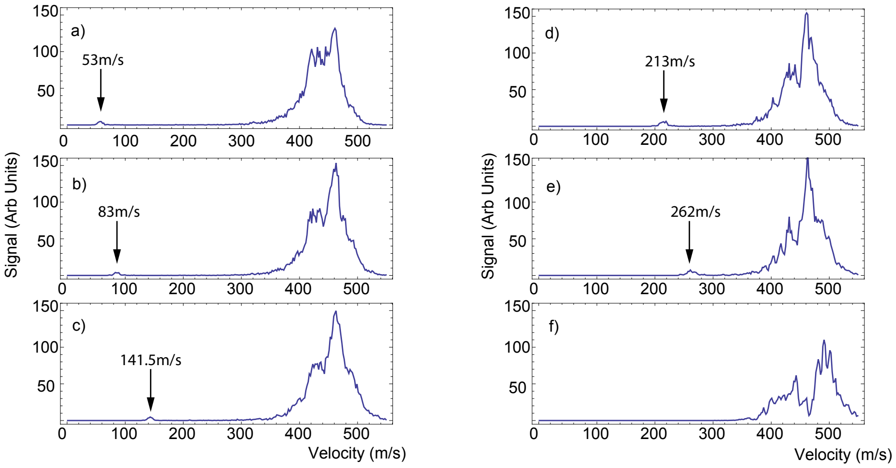

Figure 4.32: Velocity distribution of molecules at the detector, obtained from simulation, for decelerating a pulse with initial velocity of 420m/s down to a) 53m/s (ϕ_0 = 60.9°), b) 83m/s (ϕ_0 = 60°), c) 141.5m/s (ϕ_0 = 57°), d) 213m/s (ϕ_0 = 51°), e) 262m/s (ϕ_0 = 45°), f) 420m/s (ϕ_0 = 0°).

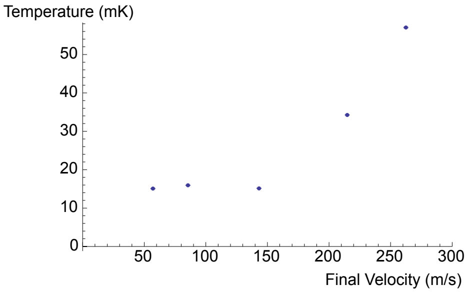

Figure 4.33: Temperature of decelerated molecules as a function of final velocity, extracted from the simulations.

of the beam exiting the decelerator is also a function of voltage. This being higher in b), the effect is compounded. These effects are also responsible for the significant losses which occur when attempting to trap molecules exiting a decelerator [140]. Another smaller effect is the deliberate selection of velocity classes which are less populated (585m/s and 420m/s). We know that the central velocity of the molecules are around 595m/s and 435m/s when using Ar and Kr respectively. Selecting molecules travelling at 585m/s and 420m/s helps to reduce the final velocity, but only at the expense of flux, since there are less molecules at these velocities to begin with.

4.4.3 Alternative deceleration strategies

The previous section outlined several mechanisms which limit the decelerated flux in a conventional Stark decelerator. The primary mechanisms are the ϕ_0 dependence of the longitudinal acceptance, the transverse focussing efficiency and the parametric coupling of the motion between the two directions [143]. The first is fundamental to the operation of a Stark decelerator. The other two, on the other hand, can be significantly improved by modifying the switch pattern. The ϕ_0 dependence

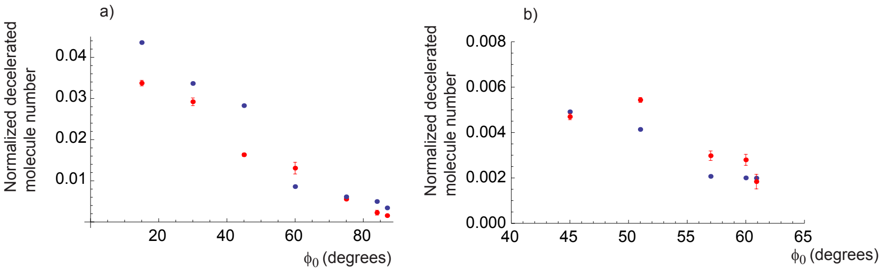

Figure 4.34: Flux vs ϕ_0 for initial velocities of a) 585m/s and b) 420m/s. Points extracted from simulated velocity distributions are shown in blue. Points from Gaussian fits to TOF data shown in red.

of the transverse guiding efficiency stems from relying on the same pair of electrodes for applying the deceleration and for guiding them transversely. In the particle-accelerator community, where phase-stability was first developed, this problem was solved by introducing additional 'guiding stages' throughout the accelerator [144]. In section 4.4.1, it has already been shown that our electrode stages can be used for guiding by leaving them on throughout the molecule's transit time. In order to create 'guiding stages', the decelerator can be left on during some of the stages. Rather than switching each time the synchronous molecule travels a distance L, we switch each time it travels the distance sL with s being any odd integer. Figure 4.35 shows the switching pattern for states $\mathcal{X}$ and $\mathcal{Y}$ for $s = 3$. In this mode, only every third stage is used for deceleration. Although this means the final velocity is far higher, the flux of decelerated molecules increases drastically, due to the additional guiding. Furthermore, $s = 3$ deceleration shifts the transverse oscillation frequency upwards and the longitudinal oscillation frequency downwards, thereby eliminating the parametric coupling. The effect is thus no longer observable, increasing the final decelerated flux. Note that $s = 3$ deceleration does lead to a slight decrease in longitudinal phase-space acceptance [139]. Because the distance between two deceleration stages is increased, the average force felt by the non-synchronous molecule is decreased. Although this would lead to a lower flux at a given phase angle, the effect is small. Over all, a considerable increase in flux is expected.

Figure 4.36 shows experimental data for $s = 3$ deceleration from an initial speed of 605m/s operating at 8kV with a switch pattern calculated for 7.6kV. Again, the signals have been normalized to the corresponding amplitudes in DC mode. The black vertical lines show the expected arrival times of the decelerated molecules. For most phase angles, the arrival times in the experimental data agree quite well with predictions. Apparent discrepancies only emerge at very high phase angles (a)-c)), where signals from decelerated molecules can no longer be clearly distinguished from the signals from undecelerated molecules. As the experiment only comprises 100 electrode pairs, we only have 32 stages available for deceleration when operating with $s = 3$. The amount of energy extracted for a given phase angle is reduced by a factor of 3. On the other hand, the TOFs show that the amplitude of the decelerated peaks is larger than the DC pulse for a wide range of ϕ_0 values. This is in contrast to conventional ($s = 1$) deceleration where the decelerated peaks were an order of magnitude smaller (see previous section). As explained above, this enhancement is due to an improved transverse guiding efficiency.

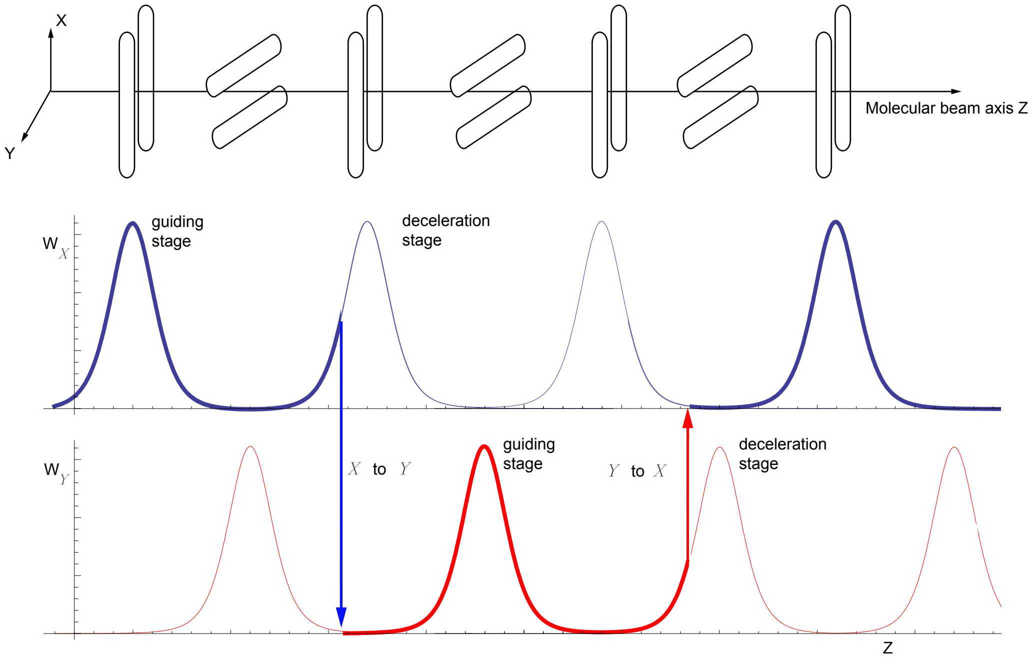

Figure 4.35: Stark potential along the molecular beam axis. The highlighted regions indicate the field seen by the synchronous molecule when operating in the $s = 3$ deceleration mode. Although the number of deceleration stages available in the experiment is reduced, we gain dedicated guiding stages, and hence flux.

Some additional features are observed in $s = 3$ deceleration. Several equally-spaced peaks arriving ahead of the synchronous pulse are observed. Although further investigation is required, we believe these emerge from the complicated dynamics of non-phase stable molecules. As a proof of principle, the molecules were also accelerated in figure 4.36 i) and j) from 605m/s to 614.9m/s (ϕ_0=-30°) and 633m/s (ϕ_0=-30°) by setting negative ϕ_0 values.

The same experiment was repeated for a krypton beam with an initial velocity set to 420m/s. The results are shown in figure 4.37. For this dataset, we did not alternate between DC and AC mode as was done in most of our data. Instead, a DC mode data set taken at the end of the entire run is shown on all the plots as a reference. This was done to preserve the Li target in the source, as it was approaching the end of its lifetime when the data was taken. There is therefore some uncertainty in the amount of initial flux during the data run, so the data has not been normalized to the DC pulse as has been done for other datasets.

The black lines show the expected arrival times of the decelerated molecules, with which the data shows excellent agreement. For the largest phase angle used in this dataset ($\phi_0 = 75°$), the molecules are decelerated from 420m/s to 320.5m/s. Figure 4.37 shows that the amplitude of the decelerated group actually increases with ϕ_0 until $\phi_0 = 45°$, beyond which a decrease is observed. The decrease when $\phi_0 > 45°$ is the usual decrease in longitudinal acceptance observed in all datasets. The initial increase in flux is similar to the increase observed in the $s = 1$, 585m/s data. Although this requires further investigation, several effects can be hypothesized. In spite of mostly decoupling the transverse focussing from longitudinal motion, there may be some

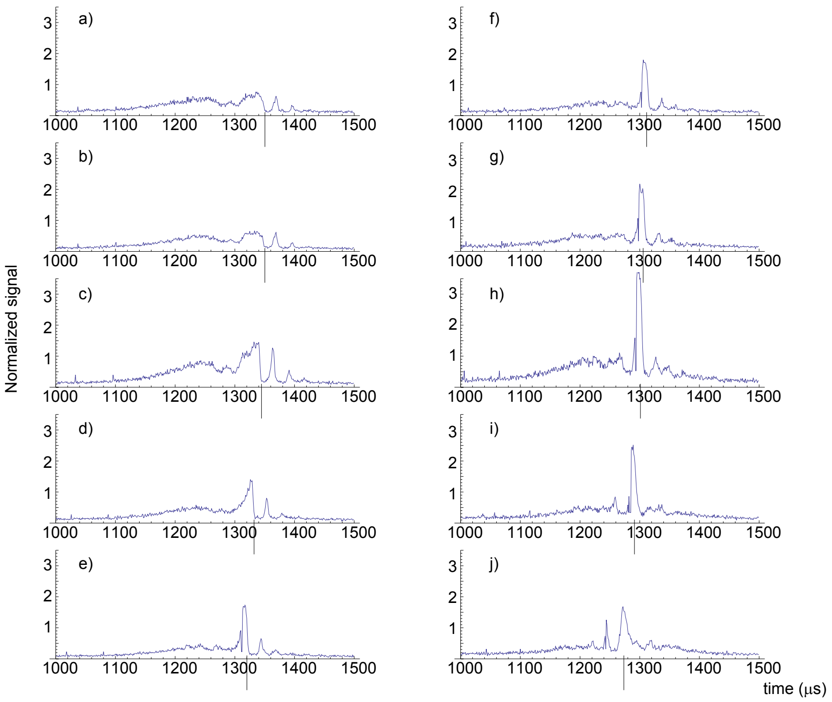

Figure 4.36: $s = 3$ deceleration at ±8kV from 605m/s to a) 557.7 m/s (ϕ_0=90°), b) 557.9 m/s (ϕ_0=87°) c) 563.0m/s (ϕ_0=75°) d) 571.7m/s (ϕ_0=60°) e) 586.2m/s (ϕ_0=45°) f) 594.6m/s (ϕ_0=30°) g) 600.4m/s (ϕ_0=15°) h) 605.0m/s (ϕ_0=0°). i) and j) show an acceleration from 605m/s to 614.9m/s (ϕ_0=-30°) and 633.0m/s (ϕ_0=-60°). The vertical axis is expressed in units of DC pulse amplitude. The black vertical lines show the expected arrival times.

residual ϕ_0 dependence on the transverse focussing. Alternatively, the suppression of flux through transitions to strong-field seeking states may also be occurring. The data is also consistent with source fluctuations. Whichever way, the amplitudes of the decelerated peaks are very much larger than the amplitude operating in DC mode for all except $\phi_0 = 75°$. This is because of the greatly improved guiding efficiency of this mode of operation, and the absence of parametric coupling between the transverse and longitudinal motions.

Figure 4.38 a) shows the flux obtained as a function of ϕ_0 for both $s = 1$ and $s = 3$ modes of operation. The dots show $s = 3$ deceleration with an initial speed of 605m/s and an applied voltage of ±8kV. The circled dots show $s = 3$ deceleration with an initial speed of 420m/s and an applied voltage of ±10kV. The squares and triangles, reproduced from figure 4.34, show the flux when applying $s = 1$ deceleration, starting at 585m/s (applying ±8kV) and 420m/s (applying ±10kV) respectively. As before, the signal was normalized to the total signal detected when operating in DC mode[4]. The error bars show the fit errors. For a given phase angle, $s = 3$ deceleration consistently shows a higher flux of molecules compared to when $s = 1$. Comparing only the $s = 3$ data, the flux for an initial speed of 420m/s shows a further increase over starting at 605m/s. This is simply due to the higher voltage which was applied when taking this data, rather than being an effect of starting at a lower initial velocity. This is in contrast to the $s = 1$ data, where the flux is lower for the ±10kV data (initial speed of 420m/s). This is due to additional losses which are

---

[4] The DC flux used to normalize the $s = 3$, 420m/s data was estimated from the flux at the end of the run.

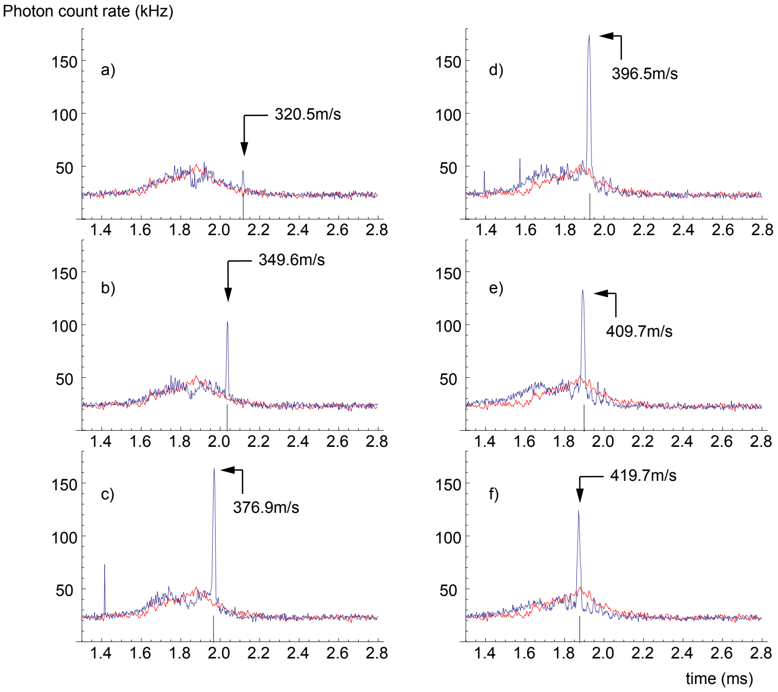

Figure 4.37: $s = 3$ deceleration at ±10kV from 420m/s to a) 320.5 m/s (ϕ_0=75°), b) 349.6 m/s (ϕ_0=60°) c) 376.9m/s (ϕ_0=45°) d) 396.5m/s (ϕ_0=30°) e) 409.7m/s (ϕ_0=15°) f) 419.7m/s (ϕ_0=0°). The blue TOF shows the result of switching the decelerator, while the red curve shows the signal from guiding the molecules by leaving the fields on (DC guiding mode). The black vertical lines show the expected arrival times.

incurred at very low final speeds (see discussion of figure 4.34, above). This reduces the flux of the 420m/s sets to below the 585m/s ones in spite of the increased voltage.

Figure 4.38 b) shows the identical data, plotted as a function of final velocity. The figure shows that although the flux in $s = 3$ is far higher, the velocity also remains high. At the current voltage, however, it is not possible to bring molecules to rest using only 33 stages. In order to do this, the voltage of the decelerator must be increased, requiring further high voltage conditioning.

Figure 4.38 indicates that it is clearly desirable to work with $s = 3$ deceleration in order to increase the flux. However, recent work on $s = 3$ deceleration carried out in Berlin [145] and Boulder [146] show that the advantages of $s = 3$ deceleration are lost at very low velocities. Over-focussing arises once the wavelength of the transverse oscillations of the molecules becomes comparable to the spatial period of the decelerator (see section 4.2.4). In this case, the transverse force $F(Z)$ is no longer well-described by an average force $\tilde{F}$. Molecules are lost in the regions between two stages of the same orientation, where the focussing forces are weak. For $s = 1$ deceleration, the spatial period of the transverse force is $2L$ in each direction. The spatial period of the focussing force increases to $6L$ in $s = 3$. Furthermore, the wavelength of the transverse oscillations of the molecules is shorter when $s = 3$, due to the increase in transverse focussing forces. The result is that, in contrast to $s = 1$ where over-focussing only occurs once the molecules are decelerated to very low speeds, the effect is observed at somewhat higher longitudinal velocities when $s = 3$. It was thus shown that for low speeds, the flux for $s = 3$ deceleration is actually lower than for $s = 1$

[145, 146].

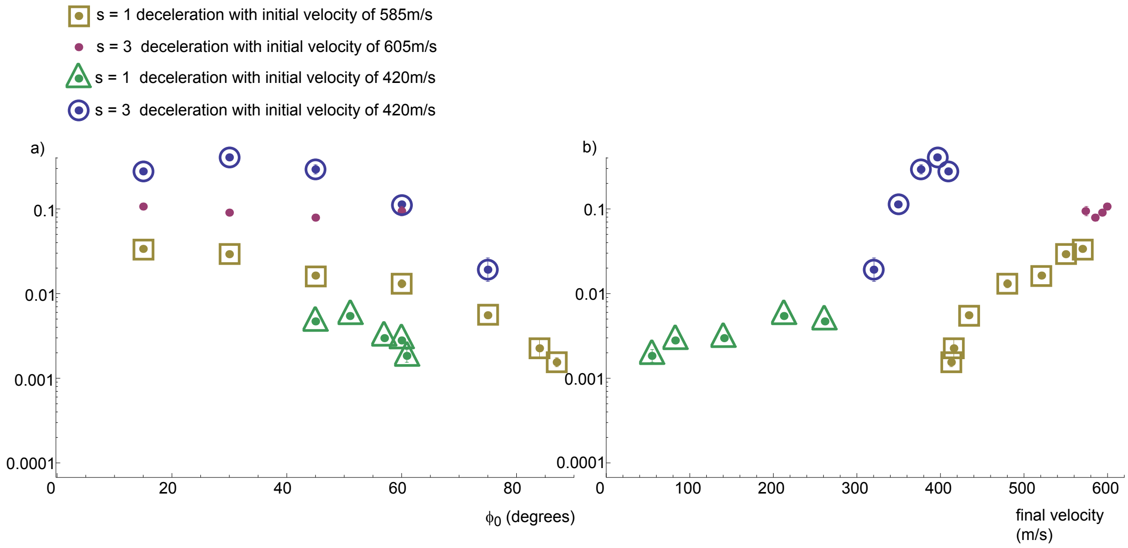

Figure 4.38: Flux of decelerated molecules (normalized to the DC signal) vs a) ϕ_0 and b) final velocity v_f. The points and circled points show $s = 3$ deceleration starting at 605/420m/s, while the squares and triangles show the $s = 1$ deceleration from 585/420m/s.

4.5 Conclusion

The Stark deceleration of LiH molecules with an initial velocity of 420m/s to a final velocity of 53m/s has been demonstrated. This corresponds to a 98.5% reduction in kinetic energy. At this speed, the molecules can be loaded into an electrostatic trap which would also act as the final stage of deceleration. This reduction in speed was achieved with a 100 stage Stark decelerator for weak-field seeking molecules, operating at ±10kV. Of all the $J = 1$, $m_j = 0$ molecules detected in DC mode, about 0.2% were successfully decelerated to this low velocity, corresponding to 17.5±7 molecules per shot. The temperature was found to be around 15mK. In order to increase this flux, $s = 3$ deceleration was also investigated. Although this did indeed increase the flux, the final velocity is much higher than the $s = 1$ case. The decelerator would need to be operated at a higher voltage in order to bring the molecules to rest using $s = 3$ deceleration.

Chapter 5

Concluding remarks

Following a short summary of the results presented in this thesis, future work for the project will be outlined.

5.1 Summary of results

By combining laser ablation and supersonic expansion techniques, a cold beam of LiH molecules with translational, rotational and vibrational temperatures of 0.9±0.1K, 5.9±0.5K and 468±17K was created. The beam velocity is 600m/s or 420m/s, depending on the carrier gas used. Approximately 90% of the molecules were observed to be in the $X^1\Sigma^+$ ($v = 0$, $J = 0$) ground state, with a flux of 4.5±1.8 $\times 10^7$ molecules per steradian per shot. The molecules were detected by laser-induced fluorescence on the $X^1\Sigma^+$ ($v = 0$)-$A^1\Sigma^+$ ($v = 3$) R(0) transition. These molecules were excited to the $J = 1$ state by driving the rotational transition at 444GHz. The microwaves were produced by quintupling the output of a Gunn oscillator phase locked to a microwave synthesizer. 68% of the ground state molecules were successfully transfered to the $J = 1$ state. The rotational frequency was measured to be 443952.91±0.09MHz, in agreement with two other measurements of similar precision. The molecules in the $J = 1$, $m_J = 0$ state were then decelerated using a 100-stage Stark decelerator for weak-field seeking molecules. Starting with an initial speed of 585m/s, a final velocity of 413.5m/s is obtained. Starting from an initial velocity of 420m/s, 0.2% of the molecules detected in the $J = 1$, $m_J = 0$ state when operating in DC mode were decelerated to 53m/s, with a temperature of 15mK. This corresponds to a flux of around 17.5±7 molecules per shot. At this final speed, corresponding to a removal of 98.5% of the translational kinetic energy, the molecules can be coupled into an electrostatic trap for further experiments. This is the first time a beam of cold LiH molecules has been made, and the first time LiH has been decelerated.

5.2 Future work

The obvious next step in the experiment would be to trap the molecules. Other species of dipolar molecules have been successfully trapped using electric fields [147, 76]. We hope to proceed along a similar path. The velocity distribution accepted by a trap can be estimated by equating $mv^2/2$

to ΔW. Knowing that ΔW is around 25GHz, the maximum velocity of LiH molecules accepted by a trap would be around 50m/s. If we say that the characteristic size of the trap is 1mm, then the acceptance is around 50(mm)m/s in a given direction. If we assume the trap can be made to have the same acceptance in all directions, the 3-D acceptance is simply $50^3\text{mm}^3(\text{m/s})^3$. This can be compared to the area in phase space occupied by molecules exiting the decelerator in the experiments reported in chapter 4. From simulations, we find this to be $13.4\text{mm}^3(\text{m/s})^3$. We see that the acceptance of the trap is very much larger than the area in phase-space occupied by the molecules. This means that in principle, all the decelerated molecules could be trapped. A practical experiment may have losses due to poor coupling to the trap, but it should be possible to minimize such losses through careful design. Furthermore, since the trap acceptance is so much larger than the area occupied by the molecules, it may be possible to accumulate decelerated molecules from several pulses, provided the trap lifetime is long compared to the repetition rate of the deceleration cycle. At present, the number of slow LiH molecules produced per shot is too small for most practical experiments. Nevertheless, there are many potential improvements that could increase this number greatly.

5.2.1 Improvements to the experiment

Several alternative methods of producing a cold supersonic beam of LiH have already been attempted (see chapter 2). Nevertheless, many options remain to be explored. A large number of other candidate seed-gases can be imagined, such as methane or ammonia. Other lithium containing solids, such as lithium amides or alloys could be used as ablation targets. A possible improvement may come from using a UV laser to dissociate the H_2 before the injection of lithium atoms. Alternatively, the target could be placed in the high pressure region behind the valve, creating the molecules before the expansion[1]. With lithium placed behind the valve, one could even imagine turning this region into an oven, thereby removing the need for an ablation laser. As mentioned before, creating an intense molecular beam is a black art. The search for a more efficient source is always an ongoing subject of investigation.

Some improvements to our current setup can also be envisaged. A higher voltage on the decelerator would help in bringing far more molecules to rest. The simulated curves in figure 5.1 a) show the phase angle required to decelerate molecules to 50m/s from 420m/s as a function of applied voltage. For a given ϕ_0, a higher voltage is required in $s = 3$ deceleration (red curve) than in $s = 1$ (blue curve) owing to the reduced number of deceleration stages. Also, excessive focussing which arises in $s = 3$ deceleration may result in lower flux when operating in this mode once low speeds are reached [145, 146]. In either mode, the required ϕ_0 decreases as the voltage is increased, which in turn increases the longitudinal acceptance. Figure 5.1 b) shows the projected flux of decelerated molecules for $s = 1$ deceleration as a function of the applied voltage, extracted from simulations. The vertical axis is normalized to the flux at 10kV. Operating at ±20kV would improve the flux by an order of magnitude. Although these voltages are experimentally challenging (corresponding to electric fields of 200kV/cm), they have been achieved in other experiments in

---

[1] I do not know whether any molecules created this way would actually make it though the valve.

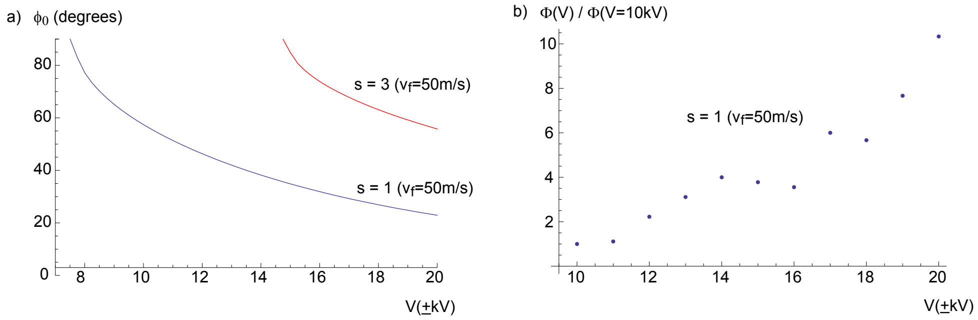

Figure 5.1: a) Phase angle ϕ_0 required to decelerate the molecules to 50m/s and b) expected flux of 50m/s pulse as a function of applied voltage (kV). b) is normalized to the flux at 10kV.

our laboratory. I am therefore hopeful about operating at these conditions in the future.

Another strategy for increasing the LiH flux is to use a modified solenoid valve called an Even-Lavie valve, which has been specifically tailored for molecular beam experiments [148]. These valves can create gas pulses as short as 20μs, thereby compressing our LiH pulse. This would allow more molecules to be matched to the decelerator's longitudinal acceptance, thus also increasing the final flux.

Higher detection efficiency would also provide a better signal-to-noise ratio. Since taking the data presented in chapter 4, we have successfully increased our probe laser power by a factor of 2. We expect that our signal will also benefit by the same factor. Also, Hamamatsu have recently developed a new series of photomultiplier tubes ('ultra-bialkali') which have a peak quantum efficiency of over 40% at 350nm, which is very close to our detection wavelengths. This would improve the detection efficiency by yet another factor of 2 over our current setup.

Since the writing of chapter 3, a new microwave source has been purchased, capable of delivering up to 250μW of power at 444GHz. The apparatus is currently being tested. This could improve the transfer efficiency to the $J = 1$ state. Another method of improving the population transfer would be to apply a small DC electric field on the molecules while driving the rotational transition. The Stark shift would lift the degeneracy of the upper states, allowing all the molecules to be excited exclusively to the $m_J = 0$ state. By preventing molecules from rotating to the strong-field seeking $m_J = \pm 1$ states (and thus being lost upon entering the decelerator), the flux would increase by a factor of 3. Charging parallel plates separated by 1cm to 530V would be sufficient to shift the $m_J = \pm 1$ states away from the $m_J = 0$ state by 1MHz. This would shift the $J = 0$ - ($J = 1$, $m_J = 0$) transition up by 1.7MHz, which remains within the range of our microwave source. There is a requirement on the field homogeneity across the interaction region, so that the microwaves remain on resonance with the molecules. For an interaction length of 5cm, the plates would only have to remain parallel to within 8°, a very feasible angle. The molecules would however need to be kept in an electric field until reaching the decelerator to prevent the states from becoming degenerate. The easiest way to achieve this is to drive the transition a few cm upstream of the decelerator entrance.

I hope that combining these efforts will lead to sufficient flux to allow for experiments with trapped LiH molecules.

5.2.2 The next step

Once trapped, the translational temperature of the molecules would be on the order of tens of mK [80]. To reach the ultra-cold regime, a further step is required. We are pursuing the possibility of sympathetically cooling the molecules using laser-cooled Li atoms. Although sympathetic cooling has been shown to be very successful for ions [101] as well as laser cooled ^{87}Rb atoms [102], no experiment to date has implemented the technique for neutral polar molecules. To this end, a Li MOT has been prepared. Very little is known about the elastic and inelastic collision cross-sections of molecules, as they are notoriously difficult to calculate. Recent theoretical work indicates that there is an inelastic loss channel in the J=1 state [149], which would make sympathetic cooling very difficult. This would mean that the molecules would need to be pumped back to the ground state before any sympathetic cooling can be attempted. To trap the molecules in the ground state, an AC electric trap [150] or an optical dipole trap can be used. By overlapping the cloud of molecules with the Li atoms from the MOT, we hope to be able to observe neutral polar molecules in the ultra-cold regime.

Bibliography

[1] H. L. Bethlem, G. Meijer. *Production and application of translationally cold molecules.* Int. Rev. Phys. Chem. **22**, 73 (2003).

[2] H. L. Bethlem, G. Berden, G. Meijer. *Decelerating neutral dipolar molecules.* Phys. Rev. Lett. **83**, 1558 (1999).

[3] S. K. Tokunaga, J. O. Stack, J. J. Hudson, *et al. A supersonic beam of cold lithium hydride molecules.* J. Chem. Phys. **126**, 124314 (2007).

[4] S. K. Tokunaga, J. M. Dyne, E. A. Hinds, *et al. Stark deceleration of lithium hydride molecules. arXiv:0812.4188.* N. J. P. focus issue: Cold and Ultracold Molecules (accepted) (2009).

[5] B. Odom, D. Hanneke, B. D'Urso, *et al. New Measurement of the Electron Magnetic Moment Using a One-Electron Quantum Cyclotron.* Phy. Rev. Lett. **97**, 030801 (2006).

[6] G. Gabrielse, D. Hanneke, T. Kinoshita, *et al. New Determination of the Fine Structure Constant from the Electron g Value and QED.* Phys. Rev. Lett. **97**, 30802 (2006).

[7] P. J. Mohr, B. N. Taylor. *CODATA recommended values of the fundamental physical constants: 2002.* Rev. Mod. Phys. **77**, 1 (2005).

[8] C. Schwob, L. Jozefowski, B. de Beauvoir, *et al. Optical Frequency Measurement of the* $2S - 12D$ *Transitions in Hydrogen and Deuterium: Rydberg Constant and Lamb Shift Determinations.* Phys. Rev. Lett. **82**, 4960 (1999).

[9] C. S. Wood, S. C. Bennett, D. Cho, *et al. Measurement of Parity Nonconservation and an Anapole Moment in Cesium.* Science **275**, 1759 (1997).

[10] B. C. Regan, E. D. Commins, C. J. Schmidt, *et al. New Limit on the Electron Electric Dipole Moment.* Phys. Rev. Lett. **88**, 071805 (2002).

[11] K. Szymaniec, W. Chalupczak, P. B. Whibberley, *et al. Evaluation of the primary frequency standard NPL-CsF1.* Metrologia **42**, 49 (2005).

[12] A. D. Ludlow, T. Zelevinsky, G. K. Campbell, *et al. Sr Lattice Clock at* 1×10^{16} *Fractional Uncertainty by Remote Optical Evaluation with a Ca Clock.* Science **319**, 1805 (2008).

[13] E. M. Purcell, N. F. Ramsey. *On the Possibility of Electric Dipole Moments for Elementary Particles and Nuclei.* Phys. Rev. **78**, 807 (1950).

[14] B. Aubert, D. Boutigny, J.-M. Gaillard, *et al.* *Observation of CP Violation in the B^0 Meson System.* Phys. Rev. Lett. **87**, 091801 (2001).

[15] K. Abe, K. Abe, R. Abe, *et al.* *Observation of Large CP Violation in the Neutral B Meson System.* Phys. Rev. Lett. **87**, 091802 (2001).

[16] J. J. Hudson, B. E. Sauer, M. R. Tarbutt, *et al.* *Measurement of the Electron Electric Dipole Moment Using YbF Molecules.* Phys. Rev. Lett. **89**, 023003 (2002).

[17] D. W. Rein. *Some remarks on parity violating effects of intramolecular interactions.* J. Mol. Evol. **4**, 15 (1974).

[18] V. S. Letokhov. *On difference of energy levels of left and right molecules due to weak interactions.* Physics Letters A **53**, 275 (1975).

[19] M. Ziskind, C. Daussy, T. Marrel, *et al.* *Improved sensitivity in the search for a parity-violating energy difference in the vibrational spectrum of the enantiomers of CHFClBr.* Euro. Phys. J. D **20**, 219 (2002).

[20] D. DeMille, S. B. Cahn, D. Murphree, *et al.* *Using Molecules to Measure Nuclear Spin-Dependent Parity Violation.* Phys. Rev. Lett. **100**, 023003 (2008).

[21] J. K. Webb, M. T. Murphy, V. V. Flambaum, *et al.* *Further Evidence for Cosmological Evolution of the Fine Structure Constant.* Phys. Rev. Lett. **87**, 091301 (2001).

[22] V. V. Flambaum, M. G. Kozlov. *Enhanced Sensitivity to the Time Variation of the Fine-Structure Constant and m_p/m_e in Diatomic Molecules.* Phys. Rev. Lett. **99**, 150801 (2007).

[23] E. Reinhold, R. Buning, U. Hollenstein, *et al.* *Indication of a Cosmological Variation of the Proton-Electron Mass Ratio Based on Laboratory Measurement and Reanalysis of H_2 Spectra.* Phys. Rev. Lett. **96**, 151101 (2006).

[24] E. R. Hudson, H. J. Lewandowski, B. C. Sawyer, *et al.* *Cold Molecule Spectroscopy for Constraining the Evolution of the Fine Structure Constant.* Phys. Rev. Lett. **96**, 143004 (2006).

[25] H. L. Bethlem, M. Kajita, B. Sartakov, *et al.* *Prospects for precision measurements on ammonia molecules in a fountain.* The European Physical Journal Special Topics **163**, 55 (2008).

[26] S. Y. T. van de Meerakker, N. Vanhaecke, M. P. J. van der Loo, *et al.* *Direct Measurement of the Radiative Lifetime of Vibrationally Excited OH Radicals.* Phys. Rev. Lett. **95**, 013003 (2005).

[27] J. J. Gilijamse, S. Hoekstra, S. A. Meek, *et al.* *The radiative lifetime of metastable CO (a Π, v= 0).* J. Chem. Phys. **127**, 221102 (2007).

[28] J. J. Gilijamse, S. Hoekstra, S. Y. T. van de Meerakker, *et al.* *Near-Threshold Inelastic Collisions Using Molecular Beams with a Tunable Velocity.* Science **313**, 1617 (2006).

[29] B. C. Sawyer, B. K. Stuhl, D. Wang, *et al.* *Molecular Beam Collisions with a Magnetically Trapped Target.* Phys. Rev. Lett. **101**, 203203 (2008).

[30] S. Y. T. van de Meerakker. *Private communication.*

[31] R. V. Krems. *Molecules near absolute zero and external field control of atomic and molecular dynamics.* Int. Rev. Phys. Chem. **24**, 99 (2005).

[32] A. V. Avdeenkov, J. L. Bohn. *Linking Ultracold Polar Molecules.* Phys. Rev. Lett. **90**, 043006 (2003).

[33] E. R. Hudson, C. Ticknor, B. C. Sawyer, *et al.* *Production of cold formaldehyde molecules for study and control of chemical reaction dynamics with hydroxyl radicals.* Phys. Rev. A **73**, 063404 (2006).

[34] J. R. Bochinski, E. R. Hudson, H. J. Lewandowski, *et al.* *Cold free-radical molecules in the laboratory frame.* Phys. Rev. A **70**, 043410 (2004).

[35] M. H. Anderson, J. R. Ensher, M. R. Matthews, *et al.* *Observation of Bose-Einstein Condensation in a Dilute Atomic Vapor.* Science **269**, 198 (1995).

[36] A. G. Truscott, K. E. Strecker, W. I. McAlexander, *et al.* *Observation of Fermi Pressure in a Gas of Trapped Atoms.* Science **291**, 2570 (2001).

[37] M. Greiner, O. Mandel, T. Esslinger, *et al.* *Quantum phase transition from a superfluid to a Mott insulator in a gas of ultracold atoms.* Nature **415**, 39 (2002).

[38] K. Góral, L. Santos, M. Lewenstein. *Quantum Phases of Dipolar Bosons in Optical Lattices.* Phys. Rev. Lett. **88**, 170406 (2002).

[39] L. Santos, G. V. Shlyapnikov, M. Lewenstein. *Roton-Maxon Spectrum and Stability of Trapped Dipolar Bose-Einstein Condensates.* Phys. Rev. Lett. **90**, 250403 (2003).

[40] M. A. Baranov, M. S. Mar'enko, V. S. Rychkov, *et al.* *Superfluid pairing in a polarized dipolar Fermi gas.* Phys. Rev. A **66**, 013606 (2002).

[41] M. A. Baranov, K. Osterloh, M. Lewenstein. *Fractional Quantum Hall States in Ultracold Rapidly Rotating Dipolar Fermi Gases.* Phys. Rev. Lett. **94**, 070404 (2005).

[42] N. R. Cooper, E. H. Rezayi, S. H. Simon. *Vortex Lattices in Rotating Atomic Bose Gases with Dipolar Interactions.* Phys. Rev. Lett. **95**, 200402 (2005).

[43] D. DeMille. *Quantum Computation with Trapped Polar Molecules.* Phys. Rev. Lett. **88**, 067901 (2002).

[44] A. Andre, D. DeMille, J. M. Doyle, *et al.* *A coherent all-electrical interface between polar molecules and mesoscopic superconducting resonators.* Nature Physics **2**, 636 (2006).

[45] P. Rabl, D. DeMille, J. M. Doyle, *et al.* *Hybrid Quantum Processors: Molecular Ensembles as Quantum Memory for Solid State Circuits.* Phys. Rev. Lett. **97**, 033003 (2006).

[46] J. T. Bahns, W. C. Stwalley, P. L. Gould. *Laser cooling of molecules: A sequential scheme for rotation, translation, and vibration.* J. Chem. Phys. **104**, 9689 (1996).

[47] J. M. Doyle, B. Friedrich, J. Kim, *et al. Buffer-gas loading of atoms and molecules into a magnetic trap.* Phys. Rev. A **52**, R2515 (1995).

[48] J. Kim, B. Friedrich, D. P. Katz, *et al. Buffer-gas loading and magnetic trapping of atomic europium.* Phys. Rev. Lett. **78**, 3665 (1997).

[49] J. D. Weinstein, R. deCarvalho, J. Kim, *et al. Magnetic trapping of atomic chromium.* Phys. Rev. A **57**, R3173 (1998).

[50] J. D. Weinstein, R. Decarvalho, T. Guillet, *et al. Magnetic trapping of calcium monohydride molecules at millikelvin temperatures.* Nature **395**, 148 (1998).

[51] W. C. Campbell, E. Tsikata, H.-I. Lu, *et al. Magnetic Trapping and Zeeman Relaxation of NH* ($X\,^3\Sigma^-$). Phys. Rev. Lett. **98**, 213001 (2007).

[52] J. Doyle, B. Friedrich, R. V. Krems, *et al. Editorial: Quo vadis, cold molecules?* The European Physical Journal D **31**, 149 (2004).

[53] H. R. Thorsheim, J. Weiner, P. S. Julienne. *Laser-induced photoassociation of ultracold sodium atoms.* Phys. Rev. Lett. **58**, 2420 (1987).

[54] P. D. Lett, K. Helmerson, W. D. Phillips, *et al. Spectroscopy of* Na_2 *by photoassociation of laser-cooled Na.* Phys. Rev. Lett. **71**, 2200 (1993).

[55] A. P. Mosk, M. W. Reynolds, T. W. Hijmans, *et al. Photoassociation of Spin-Polarized Hydrogen.* Phys. Rev. Lett. **82**, 307 (1999).

[56] N. Herschbach, P. J. J. Tol, W. Vassen, *et al. Photoassociation Spectroscopy of Cold* $He(2^3S)$ *Atoms.* Phys. Rev. Lett. **84**, 1874 (2000).

[57] G. Zinner, T. Binnewies, F. Riehle, *et al. Photoassociation of Cold Ca Atoms.* Phys. Rev. Lett. **85**, 2292 (2000).

[58] E. R. I. Abraham, W. I. McAlexander, C. A. Sackett, *et al. Spectroscopic Determination of the s-Wave Scattering Length of Lithium.* Phys. Rev. Lett. **74**, 1315 (1995).

[59] A. N. Nikolov, E. E. Eyler, X. T. Wang, *et al. Observation of Ultracold Ground-State Potassium Molecules.* Phys. Rev. Lett. **82**, 703 (1999).

[60] J. D. Miller, R. A. Cline, D. J. Heinzen. *Photoassociation spectrum of ultracold Rb atoms.* Phys. Rev. Lett. **71**, 2204 (1993).

[61] C. Gabbanini, A. Fioretti, A. Lucchesini, *et al. Cold Rubidium Molecules Formed in a Magneto-Optical Trap.* Phys. Rev. Lett. **84**, 2814 (2000).

[62] A. Fioretti, D. Comparat, A. Crubellier, *et al. Formation of Cold* Cs_2 *Molecules through Photoassociation.* Phys. Rev. Lett. **80**, 4402 (1998).

[63] M. Viteau, A. Chotia, M. Allegrini, *et al.* *Optical Pumping and Vibrational Cooling of Molecules.* Science **321**, 232 (2008).

[64] J. P. Shaffer, W. Chalupczak, N. P. Bigelow. *Photoassociative ionization of heteronuclear molecules in a novel two-species magneto-optical trap.* Phys. Rev. Lett. **82**, 1124 (1999).

[65] C. Haimberger, J. Kleinert, M. Bhattacharya, *et al.* *Formation and detection of ultracold ground-state polar molecules.* Phys. Rev. A **70**, 021402 (2004).

[66] D. Wang, J. Qi, M. F. Stone, *et al.* *Photoassociative Production and Trapping of Ultracold KRb Molecules.* Phys. Rev. Lett. **93**, 243005 (2004).

[67] A. J. Kerman, J. M. Sage, S. Sainis, *et al.* *Production and State-Selective Detection of Ultracold RbCs Molecules.* Phys. Rev. Lett. **92**, 153001 (2004).

[68] J. Deiglmayr, A. Grochola, M. Repp, *et al.* *Formation of Ultracold Polar Molecules in the Rovibrational Ground State.* Phys. Rev. Lett. **101**, 133004 (2008).

[69] F. Ferlaino, S. Knoop, R. Grimm. *Ultracold feshbach molecules. arxiv:0809.3920v1* (2008).

[70] C. Ospelkaus, S. Ospelkaus, L. Humbert, *et al.* *Ultracold Heteronuclear Molecules in a 3D Optical Lattice.* Phys. Rev. Lett. **97**, 120402 (2006).

[71] K.-K. Ni, S. Ospelkaus, M. H. G. de Miranda, *et al.* *A High Phase-Space-Density Gas of Polar Molecules.* Science **322**, 231 (2008).

[72] C. Weber, G. Barontini, J. Catani, *et al.* *Association of ultracold double-species bosonic molecules. arxiv:0808.4077* (2008).

[73] S. A. Rangwala, T. Junglen, T. Rieger, *et al.* *Continuous source of translationally cold dipolar molecules.* Phys. Rev. A **67**, 043406 (2003).

[74] S. Willitsch, M. T. Bell, A. D. Gingell, *et al.* *Cold Reactive Collisions between Laser-Cooled Ions and Velocity-Selected Neutral Molecules.* Phys. Rev. Lett. **100**, 043203 (2008).

[75] J. R. Bochinski, E. R. Hudson, H. J. Lewandowski, *et al.* *Phase Space Manipulation of Cold Free Radical OH Molecules.* Phys. Rev. Lett. **91**, 243001 (2003).

[76] S. Y. T. van de Meerakker, N. Vanhaecke, G. Meijer. *Stark Deceleration and Trapping of OH Radicals.* Annu. Rev. Phys. Chem **57**, 159 (2006).

[77] H. L. Bethlem, F. M. H. Crompvoets, R. T. Jongma, *et al.* *Deceleration and trapping of ammonia using time-varying electric fields.* Phys. Rev. A **65**, 053416 (2002).

[78] S. Y. T. van de Meerakker, I. Labazan, S. Hoekstra, *et al.* *Production and deceleration of a pulsed beam of metastable NH ($a^1\Delta$) radicals.* Journal of Physics B: Atomic, Molecular and Optical Physics **39**, S1077 (2006).

[79] O. Bucicov, M. Nowak, S. Jung, *et al.* *Cold SO_2 molecules by Stark deceleration.* European Physical Journal D **46**, 463 (2008).

[80] H. L. Bethlem, G. Berden, F. M. H. Crompvoets, *et al. Electrostatic trapping of ammonia molecules.* Nature **406**, 491 (2000).

[81] F. M. H. Crompvoets, H. L. Bethlem, R. T. Jongma, *et al. A prototype storage ring for neutral molecules.* Nature **411**, 174 (2001).

[82] C. E. Heiner, D. Carty, G. Meijer, *et al. A molecular synchrotron.* Nature Physics **3**, 115 (2007).

[83] S. Earnshaw. *On the nature of the molecular forces which regulate the constitution of the luminferous ether.* Trans. Cambridge Phil. Soc. **7**, 97 (1842).

[84] E. D. Courant, M. S. Livingston, H. S. Snyder. *The Strong-Focusing Synchroton-A New High Energy Accelerator.* Phys. Rev. **88**, 1190 (1952).

[85] D. Auerbach, E. E. A. Bromberg, L. Wharton. *Alternate-Gradient Focusing of Molecular Beams.* J. Chem. Phys. **45**, 2160 (1966).

[86] A. Lübbert, G. Rotzoll, F. Günther. *Molecular beam focusing of ICl in rotational states with positive induced electric dipole moments.* J. Chem. Phys. **69**, 5174 (1978).

[87] D. Kakati, D. C. Laine. *Alternating Gradient Focusing of a Molecular Beam.* J. Phys. E **4**, 269 (1971).

[88] J. A. Maddi, T. P. Dinneen, H. Gould. *Slowing and cooling molecules and neutral atoms by time-varying electric-field gradients.* Phys. Rev. A **60**, 3882 (1999).

[89] H. L. Bethlem, A. J. A. van Roij, R. T. Jongma, *et al. Alternate Gradient Focusing and Deceleration of a Molecular Beam.* Phys. Rev. Lett. **88**, 133003 (2002).

[90] M. R. Tarbutt, H. L. Bethlem, J. J. Hudson, *et al. Slowing heavy, ground-state molecules using an alternating gradient decelerator.* Phys. Rev. Lett. **92**, 173002 (2004).

[91] E. Vliegen, F. Merkt. *On the electrostatic deceleration of argon atoms in high Rydberg states by time-dependent inhomogeneous electric fields.* J. Phys. B **38**, 1623 (2005).

[92] E. Vliegen, F. Merkt. *Stark deceleration of hydrogen atoms.* J. Phys. B **39**, L241 (2006).

[93] E. Vliegen, S. D. Hogan, H. Schmutz, *et al. Stark deceleration and trapping of hydrogen Rydberg atoms.* Phys. Rev. A **76**, 023405 (2007).

[94] S. R. Procter, Y. Yamakita, F. Merkt, *et al. Controlling the motion of hydrogen molecules.* Chem. Phys. Lett. **374**, 667 (2003).

[95] Y. Yamakita, S. R. Procter, A. L. Goodgame, *et al. Deflection and deceleration of hydrogen Rydberg molecules in inhomogeneous electric fields.* J. Chem. Phys. **121**, 1419 (2004).

[96] R. Fulton, A. I. Bishop, M. N. Shneider, *et al. Controlling the motion of cold molecules with deep periodic optical potentials.* Nature Physics **2**, 465 (2006).

[97] R. Fulton, A. I. Bishop, M. N. Shneider, *et al. Optical Stark deceleration of nitric oxide and benzene molecules using optical lattices.* J. Phys. B **39**, S1097 (2006).

[98] E. Narevicius, A. Libson, C. G. Parthey, *et al. Stopping Supersonic Beams with a Series of Pulsed Electromagnetic Coils: An Atomic Coilgun.* Phys. Rev. Lett. **100**, 093003 (2008).

[99] N. Vanhaecke, U. Meier, M. Andrist, *et al. Multistage Zeeman deceleration of hydrogen atoms.* Phys. Rev. A **75**, 031402 (2007).

[100] E. Narevicius, A. Libson, C. G. Parthey, *et al. Stopping supersonic oxygen with a series of pulsed electromagnetic coils: A molecular coilgun.* Phys. Rev. A **77**, 051401 (2008).

[101] D. J. Larson, J. C. Bergquist, J. J. Bollinger, *et al. Sympathetic cooling of trapped ions: A laser-cooled two-species nonneutral ion plasma.* Phys. Rev. Lett. **57**, 70 (1986).

[102] C. J. Myatt, E. A. Burt, R. W. Ghrist, *et al. Production of two overlapping bose-einstein condensates by sympathetic cooling.* Phys. Rev. Lett. **78**, 586 (1997).

[103] M. Lara, J. L. Bohn, D. Potter, *et al. Ultracold Rb-OH Collisions and Prospects for Sympathetic Cooling.* Phys. Rev. Lett. **97**, 183201 (2006).

[104] S. Schlunk, A. Marian, W. Schöllkopf, *et al. AC electric trapping of neutral atoms.* Phys. Rev. A **77**, 043408 (2008).

[105] K.-C. Lin, R. Vetter. *Alkali-hydrogen reactions.* Int. Rev. Phys. Chem. **21**, 357 (2002).

[106] P. J. Dagdigian. *Detection of LiH and NaH molecular beams by laser fluorescence and measurement of radiative lifetimes of the* $A^1\sum^+$*state.* J. Chem. Phys. **64**, 2609 (1976).

[107] G. Scoles, ed. *Atomic and Molecular Beam Methods*, volume 1 (Oxford University Press, 1988), 1st edition. Pages 3-13 written by G. Scoles.

[108] G. Scoles, ed. *Atomic and Molecular Beam Methods*, volume 1 (Oxford University Press, 1988), 1st edition. Pages 14-53 written by D. R. Miller.

[109] W. R. Gentry, C. F. Giese. *Ten-microsecond pulsed molecular beam source and a fast ionization detector.* Rev. Sci. Instrum. **49**, 595 (1978).

[110] G. Scoles, ed. *Atomic and Molecular Beam Methods*, volume 1 (Oxford University Press, 1988), 1st edition. Pages 54-82 written by W.R.Gentry.

[111] E. R. Hudson, J. R. Bochinski, H. J. Lewandowski, *et al. Efficient Stark deceleration of cold polar molecules.* Euro. Phys. J. D **31**, 351 (2004).

[112] M. R. Tarbutt, J. J. Hudson, B. E. Sauer, *et al. A jet beam source of cold YbF radicals.* J. Phys. B **35**, 5013 (2002).

[113] T. W. Hänsch, B. Couillaud. *Laser Frequency Stabilization by Polarization Spectroscopy of a Reflecting Reference Cavity.* Optics Communications **35**, 441 (1980).

[114] M. R. Tarbutt, J. J. Hudson, B. E. Sauer, *et al.* *Preparation and manipulation of molecules for fundamental physics tests. arXiv:0803.0967* (2008).

[115] J. B. Anderson, J. B. Fenn. *Velocity Distributions in Molecular Beams from Nozzle Sources.* Physics of Fluids **8**, 780 (1965).

[116] G. Herzberg. *Spectra of Diatomic Molecules* (D. Van Nostrand Company, Inc., Princeton, 1950).

[117] J. Brown, A. Carrington. *Rotational Spectra of diatomic molecules* (Cambridge University Press, 2003).

[118] B. H. Bransden, C. J. Joachain. *Physics of Atoms and Molecules* (Prentice Hall, 3003).

[119] R. N. Zare. *Angular momentum* (John Wiley & Sons, NY, USA, 1987).

[120] M. Dulick, K.-Q. Zhang, B. Guo, *et al.* *Far- and Mid-Infrared Emission Spectroscopy of LiH and LiD.* J. Mol. Spec. **188**, 14 (1998).

[121] N. Bouloufa, P. Cacciani, R. Vetter, *et al.* *Sub-Doppler Spectroscopy of the LiH Molecule: The A-X System.* J. Molecular Spectroscopy **202**, 37 (2000).

[122] W. Stwalley, W. Zemke. *Spectroscopy and Structure of the Lithium Hydride Diatomic Molecules and Ions.* J. Phys. Chem. Ref. Data **22**, 87 (1993).

[123] W. T. Zemke, W. Stwalley. *Radiative transition probabilities of the* $A^1\Sigma^+$-$X^1\Sigma^+$ *bands of* ^{7}*LiH.* J. Chem. Phys **68**, 4619 (1978).

[124] W. T. Zemke, J. B. Crooks, W. C. Stwalley. *Radiative and non radiative lifetimes for vibrational levels of the* $A^1\Sigma^+$ *state of* ^{7}*LiH.* J. Chem. Phys **68**, 4628 (1978).

[125] P. T. Callaghan, M. Le Gros. *Nuclear spins in the Earth's magnetic field.* Am. J. Phys **50**, 709 (1982).

[126] S. Skowronek, R. Pereira, A. Gonzalez-Urena. *Spectroscopy and Dynamics of Excited Harpooning Reactions: The Photodepletion Action Spectrum of the BaFCH3 Complex.* Journal of Physical Chemistry A **101**, 7468 (1997).

[127] E. G. Myers, D. E. Murnick, W. R. Softky. *Isotope selective laser enhancement of the* $Li+H_2$ *reaction.* App. Phys. B **43**, 247 (1987).

[128] V. Hohreiter, D. W. Hahn. *Dual-pulse laser induced breakdown spectroscopy: Time-resolved transmission and spectral measurements.* Spectrochim Acta **60**, 968 (2005).

[129] E. Rothstein. *Molecular constants of lithium hydrides by the molecular-beam electric resonance method.* J. Chem. Phys **50**, 1899 (1969).

[130] J. J. Sakurai. *Modern Quantum Mechanics* (Addison Wesley Longman, 1994).

[131] A. Edmonds. *Angular momentum in quantum mechanics* (Princeton University press, Princeton, NJ, USA, 1960).

[132] N. F. Ramsey. *Electron Coupled Interactions between Nuclear Spins in Molecules.* Phys. Rev. **91**, 303 (1953).

[133] R. R. Freeman, A. R. Jacobson, D. W. Johnson, *et al.* *The molecular Zeeman and hyperfine spectra of LiH and LiD by molecular beam high resolution electric resonance.* J. Chem. Phys **63**, 2597 (1975).

[134] C. Winnewisser, F. Lewen, H. Helm. *Transmission characteristics of dichroic filters measured by THz time-domain spectroscopy.* Applied Physics A: Materials Science & Processing **66**, 593 (1998).

[135] G. M. Plummer, E. Herbst, F. C. de Lucia. *Submillimeter spectra and molecular constants of* ^{6}*LiH,* ^{7}*LiH,* ^{6}*LiD, and* ^{7}*LiD.* J. Chem. Phys. **81**, 4893 (1984).

[136] M. Bellini, P. De Natale, M. Inguscio, *et al.* *Precise experimental test of models for the breakdown of the Born-Oppenheimer separation: The rotational spectra of isotopic variants of lithium hydride.* Phys. Rev. A **52**, 1954 (1995).

[137] R. T. Jongma, G. von Helden, G. Berden, *et al.* *Confining CO molecules in stable orbits.* Chem. Phys. Lett. **270**, 304 (1997).

[138] E. D. Courant, H. S. Snyder. *Theory of the Alternating-Gradient Synchrotron.* Annals of Physics **281**, 360 (2000). Re-print of the original paper, Annals of Physics 3, 1 (1958).

[139] S. Y. T. van de Meerakker, N. Vanhaecke, H. L. Bethlem, *et al.* *Higher-order resonances in a Stark decelerator.* Phys. Rev. A **71**, 053409 (2005).

[140] H. L. Bethlem. *Deceleration and Trapping of Polar Molecules using Time-varying Electric Fields.* Ph.D. thesis, Katholieke Universiteit Nijmengen (2002).

[141] H. L. Bethlem, G. Berden, A. J. A. van Roij, *et al.* *Trapping Neutral Molecules in a Traveling Potential Well.* Phys. Rev. Lett. **84**, 5744 (2000).

[142] S. Y. T. van de Meerakker. *Deceleration and electrostatic trapping of OH radicals.* Ph.D. thesis, Radboud Universiteit Nijmengen (2006).

[143] S. Y. T. van de Meerakker, N. Vanhaecke, H. L. Bethlem, *et al.* *Transverse stability in a Stark decelerator.* Phys. Rev. A **73**, 023401 (2006).

[144] H. Wiedemann. *Particle Accelerator Physics* (Springer, 2003).

[145] L. Scharfenberg, H. Haak, G. Meijer, *et al.* *Operation of a Stark decelerator with optimum acceptance. arXiv:0807.4056* (2008).

[146] B. C. Sawyer, B. K. Stuhl, B. L. Lev, *et al.* *Mitigation of loss within a molecular Stark decelerator.* Euro. Phys. J. D **48**, 197 (2008).

[147] H. L. Bethlem, G. Berden, F. M. H. Crompvoets, *et al.* *Electrostatic trapping of ammonia molecules.* Nature **406**, 491 (2000).

[148] U. Even, J. Jortner, D. Noy, *et al.* *Cooling of large molecules below 1 K and He clusters formation.* J. Chem. Phys. **112**, 8068 (2000).

[149] P. Zuchowski. *Private communication.*

[150] E. Peik. *Electrodynamic trap for neutral atoms.* Eur. Phys. J. D **6**, 179 (1999).